Design, Simulation, and Characterization Toolset for Nano-Scale Photonic Crystal Devices

A Dissertation
Presented to
The Academic Faculty

by

Charles M. Reinke

In Partial Fulfillment
of the Requirements for the Degree
Doctor of Philosophy in the
School of Electrical and Computer Engineering

Georgia Institute of Technology
May 2010

Design, Simulation, and Characterization Toolset for Nano-Scale Photonic Crystal Devices

Approved by:

Dr. Ali Adibi
School of ECE
Georgia Institute of Technology

Dr. Thomas Gaylord
School of ECE
Georgia Institute of Technology

Dr. John Buck
School of ECE
Georgia Institute of Technology

Dr. Kevin Kornegay
School of ECE
Georgia Institute of Technology

Dr. Hao Min Zhou
School of Mathematics
Georgia Institute of Technology

Date approved: November 19, 2009

To my wife,

My mother and step-father,

My dad,

And my grandmother

ACKNOWLEDGEMENTS

Above all, I would like to give honor and thanks to God Almighty, His Holy Spirit who guides me, and His Son Yeshua who is LORD of my life.

I would like to thank my advisor, Dr. Ali Adibi, for all the years of providing direction and support. I appreciate your vote of confidence in selecting me to be one of your first graduate students and your patience with me throughout my time in your research group. I especially thank Dr. Sina Khorasani, who provided key advice early in my graduate career and continued to offer assistance even after returning to his home in Iran.

I would like to thank my stepfather and mom, William and Miriam Dockery, for their nurture and training during my formative years, as well as the wisdom they imparted to me and prayers interceded on my behalf as I grew into adulthood. I also thank my dad, Dr. Charles L. Reinke, for his encouragement and support, and my grandmother, Doris Raiford, who has always been there for me with a kind, loving touch. To my wife, Lakeisha, I say I love you, and thank you for all the devotion, assistance, and motivation; I look forward to us living the rest of our lives together.

I would like to thank my committee members, Dr. Thomas Gaylord, Dr. John Buck, Dr. Kevin Kornegay, and Dr. Hao Min Zhou. I would also like to thank a few collaborators I have had the opportunity to work with, including Dr. Yong Xu at Virginia Tech, Dr. Robert Norwood and Dr. Savas Tay at the University of Arizona, and Dr. Xiaoguang Zhang at Oak Ridge National Laboratory. In particular, I want to thank Clyde

Bethea, who gave me valuable training in what it means to be a researcher during my summer internship at Lucent Technologies—Bell Laboratories.

I am grateful to my fellow group members for many stimulating discussions and their technical expertise; I have been blessed to work a brilliant group of associates in Dr. Adibi's group. I especially thank Omid Momtahan, Arash Karbaschi, Jiandong (JD) Huang, Aliakbar Jafarpour, Mohammad Soltani, Babak Momeni, Siva Yegnanarayanan, Majid Badieirostami, Ali Asghar Eftekhar, Murtaza Askari, Saeed Mohammadi, Ehsan Shah Hosseini, and Amir Atabaki. Lastly, I would like to thank the secretaries who provided invaluable assistance during my time at Georgia Tech, including Nancy Baines, Elaine Bennett, Angela Yvonne, and Sharon Lawrence.

TABLE OF CONTENTS

LIST OF FIGURES

SUMMARY

The objective of this research is to present a set of powerful simulation, design, and characterization tools suitable for studying novel nanophotonic devices. The simulation tools include a three-dimensional finite-difference time-domain code adapted for parallel computing that allows for a wide range of simulation conditions and material properties to be studied, as well as a semi-analytical Green's function-based complex mode technique for studying loss in photonic crystal waveguides. The design tools consist of multifunctional photonic crystal-based template that has been simulated with nonlinear effects and measured experimentally, and planar slab waveguide structure that provides highly efficient second harmonic generation is a chip-scale device suitable for photonic integrated circuit applications. The characterization tool is composed of a phase-sensitive measurement system using a lock-in amplifier and high-precision optical stages, suitable for probing the optical characteristics of nanoscale devices. The high signal-to-noise ratio and phase shift data provided by the lock-in amplifier allow for accurate transmission measurements as well as a phase spectrum that contains information about the propagation behavior of the device beyond what is provided by the amplitude spectrum alone.

CHAPTER 1

INTRODUCTION TO NANOPHOTONICS

1.1 What is nanophotonics?

Nanophotonics is a term that was coined to describe the study of light manipulation on the sub-micrometer scale. Nanoscale optical devices have compelling potential in the area of optical signal processing, including spectroscopy, telecommunications, and all-optical logic. Much emphasis has been concentrated recently on the area of photonic integrated circuits (PICs), which are the counterparts of microelectronic circuits, using light instead of photonics to manipulate information. Extensive research has been directed toward shrinking the size of PIC devices in an effort to reduce the power consumption and wafer footprint, but with the tradeoff of reduced interaction lengths and increased difficulty in handling and measuring the devices. However, benefits such as compact form factors and possible integration with microelectronics make nanophotonic systems very attractive for many applications.

The work presented here provides a set of advanced tools focused on the processes critical to cutting-edge nanophotonic research, namely simulation, design, and characterization. The simulation tools presented here include a three-dimensional finite-difference time-domain (3D FDTD) code that allows for a wide range of simulation conditions and material properties to be studied, as well as a semi-analytical Green's function-based technique for studying loss in photonic crystal (PC) waveguides. The design tools consist of multifunctional PC-based template that can also be used to enhance the effects of nonlinear material within a relatively small footprint, and planar

slab waveguide structure that provides highly efficient second harmonic generation is a chip-scale device suitable for photonic integrated circuit applications. Finally, the characterization tool is composed of a phase-sensitive measurement system using a lock-in amplifier and precise optical stages, suitable for probing the optical characteristics of nanoscale devices. The high signal-to-noise ratio and phase shift data provided by the lock-in amplifier allow for accurate transmission measurements as well as a phase spectrum that contains information about the propagation behavior of the device beyond what is provided by the amplitude spectrum alone.

1.2 Nonlinear optics

Nonlinear optics deals with materials that have a polarization vector that varies nonlinearly with the electric field of an optical beam, typically at high light intensities. Nonlinear optical materials can be used to enable functionalities that include wavelength conversion, optical amplification, and logic operations. Such phenomena have applications in many areas such as high-speed telecommunications and optical computing [1]. Of particular interest, all-optical control of electromagnetic waves can be achieved, which enables all-optical signal processing. Nonlinear optics also has a number of inherent benefits, such as the ability to compensate for linear dispersion and diffraction effects, as evidenced by temporal and spatial solitons [2]. Utilizing the nonlinear properties of various materials, optical switches and modulators have also been realized and found wide applications in the state-of-the-art telecommunication industry [3],[4]. A very common technique for analyzing nonlinear optical wave propagation is the nonlinear Schrödinger equation. The solutions of the nonlinear Schrödinger equation can

be found analytically, which provide the basic framework for the investigation of important subjects such as solitons [5] and can lend important insights for the study of other nonlinear optical phenomena [6],[7]. However, the nonlinear Schrödinger equation makes certain assumptions that make it best suited to geometrically simple systems such as free-space optics and fiber optics. For other systems, including many nanophotonic devices, other techniques must be used.

1.3 Modeling nanophotonic structures

The simulation tools presented here include a three-dimensional (3D) FDTD code, as well as a semi-analytical Green's function-based technique for studying loss in photonic crystal (PC) waveguides. Unfortunately, it is generally difficult to apply the nonlinear Schrödinger equation to describe nonlinear wave propagation in structures that have very large index contrast or exhibit significant modal dispersion, since these properties invalidate some of the basic approximations in the derivation of the nonlinear Schrödinger equation [8]. However, the finite-difference time-domain (FDTD) technique allows for a wide range of simulation conditions and material properties to be studied. The 3D FDTD code presented in this work is based on a modification of Yee's original FDTD algorithm, which is suitable only for linear, lossless materials. The version that has been developed here is suitable for simulating arbitrary structure geometries, including anisotropy and second- and third-order nonlinear effects. The code has also been adapted to parallel processing, making it suitable for cluster and supercomputer architectures that take advantage of the ability to run a simulation on multiple processors

at the same time. The FDTD simulation tool is discussed in Chapter 2, which explains its capabilities and performance.

Propagation loss in PC structures is a major concern, and much work has been done to try to minimize such losses via design and fabrication in silicon [9]-[11], various III-IV semiconductors [12],[13], and low-index glass waveguides [14]. However, since nanofabrication is an expensive and time-consuming process, several techniques have been developed to model such losses theoretically to better understand the underlying mechanisms for the loss. Many such approaches focus on the application of perturbation theory to various mode propagation analysis techniques [15]-[18], but almost all of the techniques for loss analysis require complex and computationally demanding calculations. Thus a semi-analytical Green's function-based technique has been developed for the analysis of propagation loss in PC waveguides that only requires calculation of the complex band behavior of the waveguide. The theory governing this complex band technique and its limitations are presented in Chapter 3.

1.4 Designing nanophotonic structures

An infinite number of possibilities exist for designing arbitrary nanophotonic components. However, there are a few recurring design templates that are commonly seen in literature. One such structure is the photonic crystal, which has inspired much interest with its unique ability to control light propagation and emission through the photonic band gap [19],[20]. PCs can be useful for many applications due to their nonlinear dispersion characteristics and design flexibility [21]. By combining them with resonators or highly dispersive structures, the physical lengths of nonlinear devices may

be decreased by taking advantage of slow-light effects and resonant enhancement [22]. The design tool presented in Chapter 4 is a four-port structure based on the PC waveguide that can be used as a building block to produce devices with multiple photonic functionalities.

It is well understood that resonant structures can be used to enhance various nonlinear optical effects [23],[24]. An interesting case occurs when the magnitude of the coupling coefficient from the waveguide to the resonator is equal to the loss in the resonator at the resonant frequency. Under these conditions, called critical coupling [25], the transmission through the waveguide approaches zero and all of the power is dissipated inside the resonator. An example system that can be used for efficient on-chip second harmonic generation (SHG) is a racetrack resonator side-coupled to a slab waveguide [26]. The advantage of using the racetrack resonator is that its resonant properties allow for enhancement of nonlinear effects, while the Q and position in frequency of the resonance can be tuned by simply changing the physical properties of the resonator. If the loss mechanism is assumed to be SHG, this implies that 100% conversion efficiency can be achieved. Although other loss mechanisms besides the second harmonic effect and also the absence of complete phase matching may reduce the SHG efficiency, using critical coupling can strongly enhancement the 2nd harmonic process. Moreover, by engineering the resonator cavity length to match the coherence length for the nonlinear process of SHG, phase matching can be achieved and the double-resonant condition satisfied simultaneously [27]-[32]. The design of the two-port critically-coupled cavity structure for highly-efficient enhancement of nonlinear optical effects is detailed in Chapter 5.

1.5 Measuring nanophotonic devices

Due largely to the small feature size of nanophotonic structures, the calibration and experimental studies of these structures can be hindered by the inherent low signal-to-noise ratio (SNR) of the measurements. Design efforts have been made to improve the SNR of such measurements by increasing the light coupling efficiency in and out of the PC waveguides (PCWGs), for example, by using adiabatic tapers [33]. These designs decrease the overall insertion loss of the PCWG circuits, but are limited by the available processing technologies and often change the transmission properties of the modes of the PCWGs. Additionally, it is still a challenge to measure the dispersion of PCWGs at optical frequencies [34], which is a critical parameter for designing high-speed optical circuits. However, by incorporating a lock-in amplifier into the measurement setup, the SNR of the power transmission measurements can be improved by at least one order of magnitude, while at simultaneously providing a phase shift measurement in addition to the magnitude (transmission). The phase-sensitive lock-in characterization test-bench is described in Chapter 6, and its applicability and the value of the measured phase spectra are discussed.

CHAPTER 2

FINITE-DIFFERENCE TIME-DOMAIN SIMULATION TOOL

2.1 Finite-Difference Time-Domain Technique

A very common technique for the analysis of nonlinear optical wave propagation is the nonlinear Schrödinger equation, which for many applications can be solved analytically. Unfortunately, it is generally difficult to apply the nonlinear Schrödinger equation to describe nonlinear wave propagation in photonis crystals (PCs), since such structures typically have very large index contrast and exhibit significant modal dispersion (especially near the band edge), which invalidates the basic approximations used to derive the nonlinear Schrödinger equation [35]. The FDTD method of analysis [36], however, is a brute-force technique applicable for a wide range of complex dielectric structures, generally constrained only by the size of the computational space required for the simulation. Several FDTD-based algorithms have been developed to address nonlinear phenomena; however, most of these methods either use relatively complex formulations solved using iterative techniques [37],[38] or simplify the problem by neglecting certain field components [39], at the expense of generality of the technique. Although a practical FDTD code that can solve all nonlinear problems is elusive at best, a robust analytical solution for Kerr media may be found [40],[41], and $\chi^{(2)}$ materials can be handled using a simple iterative approach.

The three-dimensional finite-difference time-domain (3D FDTD) code presented here, designed to simulate simple anisotropic, $\chi^{(2)}$, and $\chi^{(3)}$ nonlinear materials [42], has

been developed based on a modification of Yee's original FDTD algorithm [36]. The general FDTD method solves the differential form of Maxwell's equations:

$$\frac{\partial}{\partial t}\mathbf{H} = -\frac{1}{\mu_0}\nabla \times \mathbf{E}, \tag{2.1}$$

$$\frac{\partial}{\partial t}\mathbf{E} = +\frac{1}{\varepsilon}\nabla \times \mathbf{H}, \tag{2.2}$$

which relate the electric (**E**) and magnetic (**H**) fields both in space and time. In these equations, the permittivity (ε) and magnetic permeability (μ_0) are considered scalars for all materials. In Yee's original method, the discretized magnetic and electric fields are computed at interlacing time intervals and the differentials are approximated by differences, as shown here for the *x* components

$$H_x^{\,n+\frac{1}{2}}(i, j+\tfrac{1}{2}, k+\tfrac{1}{2}) = H_x^{\,n-\frac{1}{2}}(i, j+\tfrac{1}{2}, k+\tfrac{1}{2}) + \frac{\Delta t}{\mu}\left(\frac{E_y^n(i, j+\tfrac{1}{2}, k+1) - E_y^n(i, j+\tfrac{1}{2}, k)}{\Delta z} - \frac{E_z^n(i, j+1, k+\tfrac{1}{2}) - E_z^n(i, j, k+\tfrac{1}{2})}{\Delta y}\right), \tag{2.3}$$

$$E_x^{\,n+1}(i+\tfrac{1}{2}, j, k) = E_x^{\,n}(i+\tfrac{1}{2}, j, k) - \frac{\Delta t}{\varepsilon}\left(\begin{array}{l}\dfrac{H_y^n(i+\tfrac{1}{2}, j, k+\tfrac{1}{2}) - H_y^n(i+\tfrac{1}{2}, j, k-\tfrac{1}{2})}{\Delta z} \\ -\dfrac{H_z^n(i+\tfrac{1}{2}, j+\tfrac{1}{2}, k) - H_z^n(i+\tfrac{1}{2}, j-\tfrac{1}{2}, k)}{\Delta y}\end{array}\right), \tag{2.4}$$

where *n* represents the time index, Δt is the timestep, Δy and Δz are the grid spacings in the *y* and *z* directions, respectively, and *i*, *j*, and *k* are the grid coordinates in the respective *x*, *y*, and *z* directions. The *y* and *z* field components of the electric and magnetic fields are calculated from corresponding equations, with the field components arranged spatially as shown in Figure 2.1, commonly referred to as Yee's cell.

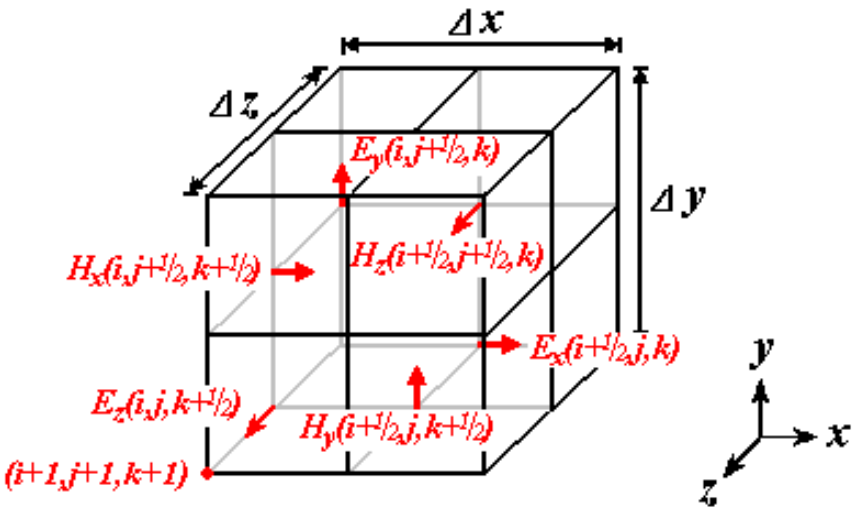

Figure 2.1. Traditional Yee's cell for a 3D FDTD domain, showing the magnetic (*H*) and electric (*E*) field components offset from each other by a half grid cell.

In this nonlinear extension, the electric displacement vector, D^n, is used to introduce the nonlinear response. Now, Eq. (2.4) is rewritten as

$$D_x^{\,n+1}(i+\tfrac{1}{2},j,k) = D_x^{\,n}(i+\tfrac{1}{2},j,k) - \Delta t\left(\begin{array}{l}\dfrac{H_y^n(i+\frac{1}{2},j,k+\frac{1}{2}) - H_y^n(i+\frac{1}{2},j,k-\frac{1}{2})}{\Delta z} \\ -\dfrac{H_z^n(i+\frac{1}{2},j+\frac{1}{2},k) - H_z^n(i+\frac{1}{2},j-\frac{1}{2},k)}{\Delta y}\end{array}\right), \tag{2.5}$$

with corresponding equations for the *y* and *z* components. This displacement vector is calculated from the previous time step through the nonlinear constitutive relation $\mathbf{D}^n = f\left(\mathbf{E}^n\right)\cdot\mathbf{E}^n$ (*f* here represents an arbitrary function). Clearly this model is for an instantaneous effect that neglects any dispersion effects, which is suitable for the materials of interest (e.g., semiconductors) since they have a nonlinear response that is effectively instantaneous on the time scale of a typical application. After finding $\mathbf{D}^{n+1}$, the electric field is advanced from the inverse constitutive relation, i.e.

$\mathbf{E}^{n+1} = f^{-1}\left(\mathbf{D}^{n+1}\right) \cdot \mathbf{D}^{n+1}$. This inversion process is possible either through exact analytical methods or an iterative approach starting with $\mathbf{E}^{n}$ as the initial value (i.e. Newton's method).

2.2 Nonlinear extension to FDTD

Although the $\chi^{(2)}$ and $\chi^{(3)}$ susceptibilities are generally a second- and third-rank tensor, respectively, for a wide variety of materials (such as many of the semiconductors used in modern optoelectronics) most of the tensor elements are negligible or equal to each other due to material symmetries and other considerations. Therefore, the total number of independent tensor elements is significantly reduced. As an example, the general second-order nonlinear susceptibility tensor is commonly written in contracted form as

$$d = \begin{bmatrix} d_{11} & d_{12} & d_{13} & d_{14} & d_{15} & d_{16} \\ d_{21} & d_{22} & d_{23} & d_{24} & d_{25} & d_{26} \\ d_{31} & d_{32} & d_{33} & d_{34} & d_{35} & d_{36} \end{bmatrix}, \tag{2.6}$$

where $d_{ij} = ½\ \chi_{ij}^{(2)}$, and the indices i and j are in Voigt notation. However, for $\chi^{(2)}$ materials of interest addressed in this paper, the tensor can be simplified as

$$d = \begin{bmatrix} 0 & 0 & 0 & d_{14} & 0 & 0 \\ 0 & 0 & 0 & 0 & d_{25} & 0 \\ 0 & 0 & 0 & 0 & 0 & d_{36} \end{bmatrix}, \tag{2.7}$$

and $d_{14} = d_{25} = d_{36}$ (i.e. 43m symmetry); hence, only one independent parameter needs to be considered. In the case of $\chi^{(3)}$ materials, the tensor has many more elements and cannot be conveniently written, however the model for many of the materials used in

photonic integrated circuits is much simpler. For example, Si and GaAs, have point groups m3m and $\bar{4}3m$, respectively [1], corresponding to the Cubic II system [43]. Thus, there are only 21 nonzero $\chi^{(3)}$ tensor components, of which only 4 are independent, as given by

$$\begin{aligned}
&\chi_{xxxx} = \chi_{yyyy} = \chi_{zzzz} \\
&\chi_{yyzz} = \chi_{zzyy} = \chi_{zzxx} = \chi_{xxzz} = \chi_{xxyy} = \chi_{yyxx} \\
&\chi_{yzyz} = \chi_{zyzy} = \chi_{zxzx} = \chi_{xzxz} = \chi_{xyxy} = \chi_{yxyx} \\
&\chi_{yzzy} = \chi_{zyyz} = \chi_{zxxz} = \chi_{xzzx} = \chi_{xyyx} = \chi_{yxxy}
\end{aligned} . \tag{2.8}$$

It turns out that there is no experimental data showing distinct numerical values for the parameters; in measurements of third order nonlinear materials only one effective figure comes out for all of them. Thus, it is convenient to treat the nonlinear susceptibilities as a scalar quantity and summarize the relationship in matrix form as

$$\mathbf{D} = \varepsilon_0 \varepsilon_r \mathbf{E} + \varepsilon_0 \chi_{eff}^{(3)} \left|\mathbf{E}\right|^2 \mathbf{E} . \tag{2.9}$$

Note that this form does not include any degeneracy factors, and thus is suitable for studying the effects involved a single polarized beam; if polarization mixing or multiple beams (i.e. having different frequencies) are to be included, degeneracy factors may have to be added to the nonlinear polarization expressions for the cross-polarized field products. Some examples of $\chi^{(2)}$ and $\chi^{(3)}$ materials of interest that can be treated using these simplifications include most semiconductors, such as gallium arsenide, KD*P, and liquid crystals. It should be mentioned that there are nonlinear algorithms which are capable of treating tensors [44], however these more complex methods, which have been developed for systems that require the full tensor forms, do not provide significant

benefits for materials such as those used for practical PC applications and in general demand an increased computational load versus this approach.

In the case of simple anisotropy, the inverse relation involves the direct inversion of the permittivity matrix. The equations for the inversion of this 3x3 matrix were found explicitly using linear algebra and then implemented directly into Yee's algorithm. For simple, non-dispersive $\chi^{(2)}$ and $\chi^{(3)}$ nonlinear materials, the required time-dependent tensors can be found from the equivalent constitutive relations given by

$$\mathbf{D} = \varepsilon_0 \begin{bmatrix} \varepsilon_r & 0 & \chi^{(2)}\mathbf{E}\cdot\hat{y} \\ \chi^{(2)}\mathbf{E}\cdot\hat{z} & \varepsilon_r & 0 \\ 0 & \chi^{(2)}\mathbf{E}\cdot\hat{x} & \varepsilon_r \end{bmatrix} \mathbf{E}, \tag{2.10}$$

$$\mathbf{D} = \varepsilon_0 \begin{bmatrix} \varepsilon_r + \chi^{(3)}|\mathbf{E}|^2 & 0 & 0 \\ 0 & \varepsilon_r + \chi^{(3)}|\mathbf{E}|^2 & 0 \\ 0 & 0 & \varepsilon_r + \chi^{(3)}|\mathbf{E}|^2 \end{bmatrix} \mathbf{E}, \tag{2.11}$$

respectively, where $\hat{x}$, $\hat{y}$, and $\hat{z}$ represent unit vectors in the respective *x*, *y*, and *z* directions. Although these relations take more elaborate tensor forms in the most general case, this compact notation is both mathematically consistent for the materials of interest and also convenient for the rest of this discussion. For $\chi^{(2)}$ nonlinear media, the inverse relation is complicated to the extent that an iterative approach becomes most efficient. This iterative method calculates the value of the **E** field at a given time step from an implicit expression that uses the values from the previous time step as an initial guess for the calculation [45]. This new value is then used as the next guess and so on until **E** is found to the desired precision. However, for self-focusing $\chi^{(3)}$ nonlinear media where the nonlinear term is essentially a scalar (such as Kerr materials), the inverse function $g = f^{-1}$

may be found in closed form as the solution to a third-order polynomial, which after simplification results in

$$g\left(\varepsilon_r, \chi^{(3)}, D\right) = \frac{-\sqrt[3]{12}\varepsilon_r + \left(9\sqrt{\chi^{(3)}}D + \sqrt{12{\varepsilon_r}^3 + 81\chi^{(3)}D^2}\right)^{\frac{2}{3}}}{\sqrt[3]{18\left(9\sqrt{\chi^{(3)}}D + \sqrt{12{\varepsilon_r}^3 + 81\chi^{(3)}D^2}\right)}D\sqrt{\chi^{(3)}}}, \tag{2.12}$$

where $D = |\mathbf{D}|$ (i.e. the magnitude of vector **D**) and ε_r is the local relative permittivity of the medium. Using Eq. (2.12), exact evaluation of the inverse constitutive relation becomes possible, and the efficiency of the algorithm is improved by 30% (in MATLAB) compared with the iterative approach. The actual performance will vary depending on the programming language, computer architecture, and other factors, but will never be worse than the iterative method since at least one iteration that involves roughly the same number of calculations as Eq. (2.12) must be performed for each grid point during each time step.

The frequency dependence of the second- or third-order nonlinear coefficients is ignored in this algorithm; this is significant because although this is a time-domain technique, any real excitation will have a non-infinite time duration and thus non-infinitesimal bandwidth in frequency. However, this assumption is well justified if the optical frequency is far from the absorption resonance of the nonlinear materials [46]. Furthermore, the frequency bandwidth of common optical signals is typically much smaller than the dispersion of the nonlinear coefficients, which allows for the $\chi^{(2)}$ or $\chi^{(3)}$ coefficients to be treated as frequency independent constants.

Since this algorithm simulates the behavior of a nonlinear system, the absolute amplitude of the electromagnetic wave in the simulation carries physical meaning and

cannot be normalized arbitrarily. Thus, a normalization factor $A_{I,N}$ is introduced which relates the physical electric field E and the normalized electric field E_N as $E_N = E/\sqrt{A_{I,N}}$. Correspondingly, the material $\chi^{(2)}$ and $\chi^{(3)}$ nonlinear coefficients are normalized as:

$$\chi_N^{(2)} = \chi^{(2)}\sqrt{A_{I,N}}\,, \tag{2.13}$$

$$\chi_N^{(3)} = \chi^{(3)} A_{I,N} = n_2 \frac{cn_0^2}{\pi} A_{I,N}\,, \tag{2.14}$$

respectively, where n_0 is the linear refractive index, n_2 is the second-order nonlinear refractive index, and $\chi_N^{(2)}$ and $\chi_N^{(3)}$ represent the respective normalized $\chi^{(2)}$ and $\chi^{(3)}$ nonlinear coefficients. The renormalization of these quantities is necessary in order to prevent the numerical values from approaching the upper or lower precision limits for a given computer architecture. Note that the numerical results given by the FDTD correspond to the normalized values, which can be converted into physical values by using the appropriate normalization factor $A_{I,N}$. Also, according to Eq. (2.13) and Eq. (2.14) the normalized nonlinear coefficients are directly related to the both the physical nonlinearity strength and the normalization factor. Thus, materials of various nonlinear strengths or different input intensity levels may be simulated by choosing appropriate values of the normalized nonlinearity strength. As an example of how physical nonlinear values compare with the corresponding normalized quantities, a value of 9.2×10^{-9} esu for $\chi^{(2)}$ (beta barium borate) with $A_{I,N} = 1$ corresponds to a normalized $\chi^{(2)}$ of 3.9×10^{-10}, and a value of 4×10^{-14} cm^2/W for n_2 (maximum for GaAs) with $A_{I,N} = 1$ corresponds to a normalized $\chi^{(3)}$ of 5.5×10^{-15}.

2.3 Nonlinear FDTD stability

It can be shown that Yee's FDTD algorithm is stable under the Courant's stability condition [47], which asserts that the numerical propagation velocity must be greater than the maximum phase velocity of the light in the structure [48]:

$$\frac{1}{\Delta t\sqrt{(\Delta x)^{-2}+(\Delta z)^{-2}}} \geq \sup\left\{\frac{1}{\sqrt{\mu_0\varepsilon_0\varepsilon_r}}\right\} = c_{\max}\,. \tag{2.15}$$

Notice that this derivation is performed for the two-dimensional case, but can be extended to three dimensions in a very straightforward manner. This condition is both necessary and sufficient for numerical stability in an FDTD code that only considers linear effects. The extension to anisotropic materials has an almost identical stability condition:

$$\frac{1}{\Delta t\sqrt{(\Delta x)^{-2}+(\Delta z)^{-2}}} \geq \sup\left\{\frac{1}{\sqrt{\mu_0\varepsilon_0\left|\mathrm{eig}\{\overline{\overline{\varepsilon}}_r\}\right|}}\right\} = c_{\max}\,, \tag{2.16}$$

except that now the eigenvalues of the permittivity tensor $\overline{\overline{\varepsilon}}_r$ are considered in the expression. In order to examine the stability of the nonlinear FDTD implementation, suppose that the simulation is run for a given time-step and spatial grid size, and the output field is observed over the entire structure. Assuming that the input field is kept unchanged, the simulation must produce the same results as if the time-dependent linear system were solved with the permittivity being a suitably defined anisotropic time-dependent tensor, rather than the original nonlinear case. This is because in Maxwell equations for anisotropic media (and therefore the FDTD method as well), field components can be decomposed into a superposition of plane waves along various directions. Each direction is normally associated with two eigenvalues and two

eigenvectors, which characterize the corresponding eigenmodes. Generally, these two modes propagate at different phase velocities, and if for each direction the fast mode is stabilized in the numerical scheme, so would be the slower mode. It can be easily demonstrated that the fastest propagating wave corresponds to the smallest refractive index, which must be one of the eigenvalues of the refractive index matrix of the anisotropic medium [49]. Therefore it is sufficient to consider only the eigen-indices.

For both $\chi^{(2)}$ and $\chi^{(3)}$ nonlinearity, the constitutive relationships, i.e. Eq. (2.10) and Eq. (2.11), respectively, depend on the strength of the electric field at each grid point in the computation space, which makes the stability analysis more complicated than the linear or simple anisotropic cases. In particular, for $\chi^{(2)}$ media the eigenvalues are

$$\mathrm{eig}\left\{\overline{\overline{\varepsilon}}\right\} = \begin{bmatrix} \varepsilon_r + \chi^{(2)}\widetilde{E} \\ \varepsilon_r - \frac{1}{2}\left(1 + j\sqrt{3}\right)\chi^{(2)}\widetilde{E} \\ \varepsilon_r - \frac{1}{2}\left(1 - j\sqrt{3}\right)\chi^{(2)}\widetilde{E} \end{bmatrix}, \tag{2.17}$$

where $\widetilde{E} = \sqrt[3]{(\mathbf{E}\cdot\hat{x})(\mathbf{E}\cdot\hat{y})(\mathbf{E}\cdot\hat{z})}$ and satisfies

$$\left|\widetilde{E}\right| = \left|\sqrt[3]{(\mathbf{E}\cdot\hat{x})(\mathbf{E}\cdot\hat{y})(\mathbf{E}\cdot\hat{z})}\right| \le \frac{|\mathbf{E}|}{\sqrt{3}}. \tag{2.18}$$

From this expression it can be deduced that for positive values of $\chi^{(2)}$ and assuming that the strength of the nonlinearity is not greater than a defined limit, the Courant's stability condition will suffice, where the limit requires that $\left|\chi^{(2)}\widetilde{E}\right| < \varepsilon_r$ as shown

$$\begin{aligned} &\widetilde{E} > 0: \quad \min\left\{\left|\mathrm{eig}\left\{\overline{\overline{\varepsilon}}\right\}\right|\right\} = \sqrt{{\varepsilon_r}^2 + \left(\chi^{(2)}\widetilde{E}\right)^2 - \varepsilon_r\chi^{(2)}\widetilde{E}} \ge \varepsilon_r - \chi^{(2)}\left|\widetilde{E}\right| \ge \varepsilon_r - \chi^{(2)}\frac{|\mathbf{E}|}{\sqrt{3}} \\ &\widetilde{E} < 0: \quad \min\left\{\left|\mathrm{eig}\left\{\overline{\overline{\varepsilon}}\right\}\right|\right\} = \varepsilon_r - \chi^{(2)}\left|\widetilde{E}\right| \ge \varepsilon_r - \chi^{(2)}\frac{|\mathbf{E}|}{\sqrt{3}} \end{aligned} \tag{2.19}$$

Therefore, for sufficiently large nonlinearity, as a result of either large field amplitudes or large normalized $\chi^{(2)}$ values, the smallest eigenvalue tends to zero and the Courant's condition no longer guarantees stability. In other words, for nonlinear strengths and field values that are not too large (i.e. $\left|\chi^{(2)}\tilde{\tilde{E}}\right| < \varepsilon_r$), the linear stability constraints on the time step size are sufficient. However, for large nonlinear strength or field values, a smaller time step should be used to guarantee that stability is maintained, as seen from Eq. (2.19). In fact, while stable operation has been demonstrated using normalized $\chi^{(2)}$ values as large as 10, instability has also been encountered for certain simulations using normalized $\chi^{(2)}$ of only 5. The difference between the two cases is the maximum field intensity encountered in the structure, which for the case of cavities or similar resonant structures can have localized spikes that increase risk of instability over that of a slab of bulk material, for example. Also, Joseph and Taflove [46] reported encountering similar stability problems with their $\chi^{(2)}$ nonlinear implementations of the FDTD method.

The stability argument for $\chi^{(3)}$ materials of interest is considerably simpler that for the $\chi^{(2)}$ case, primarily since self-focusing media are commonly studied and the corresponding tensor is isotropic. In this case, an analysis of the minimum value taken by the eigenvalues of the constitutive matrix shows that for any positive values of $\chi^{(3)}$ (i.e. for any positive Kerr materials), Courant's stability condition is still sufficient for code stability

$$\min\left\{\text{eig}\left\{\tilde{\tilde{\varepsilon}}\right\}\right\} = \varepsilon_r + \chi^{(3)}\left|\mathbf{E}\right|^2 \geq \varepsilon_r, \quad \chi^{(3)} \geq 0. \tag{2.20}$$

Therefore, the linear stability condition is applicable, since the self-focusing effect results in a local decrease of the phase velocity. As verification of this statement, a more

detailed calculation for the scalar TE modes in self-focusing media may be performed, [50] which results in

$$\frac{\sqrt{\frac{\partial\left[\varepsilon_r E + \chi^{(3)} E^3\right]}{\varepsilon_r \partial E}}}{\Delta t\sqrt{(\Delta x)^{-2} + (\Delta z)^{-2}}} \geq \frac{1}{\Delta t\sqrt{(\Delta x)^{-2} + (\Delta z)^{-2}}} \geq c_{\max}. \tag{2.21}$$

Clearly, the same result is reached, confirming that Courant's stability condition is sufficient for $\chi^{(3)}$ nonlinearity in the materials of interest in which only one independent $\chi^{(3)}$ component exists.

2.4 FDTD code validation

In order to validate the nonlinear FDTD code developed in Section 2.2, two types of well-understood nonlinear optical phenomena were simulated: second-harmonic generation in $\chi^{(2)}$ materials and self-focusing of optical beams in $\chi^{(3)}$ nonlinear media. In the simulations for the $\chi^{(2)}$ nonlinear code, a Huygens source [51] was used to excite a wave that propagates in a dielectric slab waveguide composed of the nonlinear material. The TM field profile (H_z component) at the fundamental frequency for the case of a material with normalized $\chi^{(2)}$ = 10 is shown in Figure 2.2a. The resulting SHG field, which appears as a TE field (E_z component) as predicted by the matrix constitutive relationship assumed for the $\chi^{(2)}$ case (Eq. (2.10)), is shown in the field profile in Figure 2.2b. Here, TM denotes the field that only has a magnetic field component in the direction normal to the plane of the computational domain; TE denotes a field that only has an electric field component in this direction. Also note that in this simulation a relatively large value for $\chi^{(2)}$ was used to exaggerate the SHG effect and reduce the required size of the computation domain. The spatial period (i.e. the wavelength) for the

SHG signal is observed to be roughly half that for the fundamental beam. A periodic transfer of the power between the fundamental and SHG fields can also be seen, which agrees with theory for the case of non-phase-matched co-propagating beams in a dispersive waveguide. The null on the axis seen in the second-harmonic field is due to the fact that the transverse magnetic field of the fundamental guided mode in the slab has even symmetry and therefore its electric field must vanish on the axis (i.e. the corresponding electric field has odd symmetry).

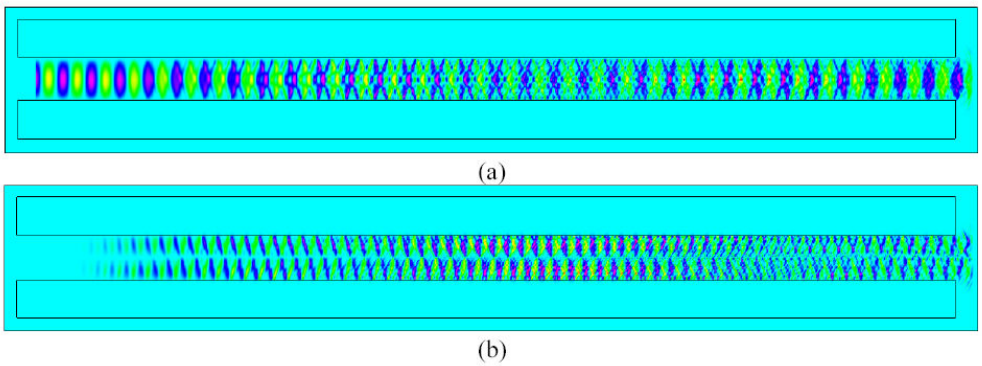

Figure 2.2. Field profiles of the **a.** fundamental (TM) and **b.** second harmonic beams in a nonlinear $\chi^{(2)}$ slab waveguide. The fundamental guided mode of the slab waveguide is excited using a Huygens' source, and the structure is surrounded by PML boundaries. The spatial pattern of the electric field in b. calculated using the nonlinear 2D FDTD code demonstrates the SHG effect.

The procedure to quantitatively examine the accuracy of the $\chi^{(2)}$ code uses the theoretical equations for a second harmonic beam generated in a slab waveguide of fixed length and composed of a $\chi^{(2)}$ nonlinear material. The calculated SHG field is then compared with analytical theory to determine the accuracy of the simulation data. According to coupled-mode theory, the definitions $D = \omega\sqrt{\frac{\mu}{\varepsilon_0}}\frac{1}{n}\varepsilon_0\chi^{(2)}$ and $\Delta k = k_{2\omega} - k_{\omega}$ are assumed. If the pump depletion is very small, then the second harmonic field produced by a slab of nonlinear material of length L is $E_{2\omega}^{out} = DE_{\omega}^{2}\frac{1-e^{i\Delta kL}}{\Delta k}$, where E_{ω} is

the pump field at the fundamental frequency and $E_{2\omega}^{out}$ is the resulting SHG field observed at the end of the waveguide. A comparison of the SHG signal calculated from FDTD with the value from these equations results in an estimated error of 4.7%. Since it is commonly understood that the FDTD in practical usage has a typical error of approximately 5%, these results verify within reasonable agreement the accuracy of the third-order nonlinear code. Also, if the coherence length of the SHG process is compared with the theoretical value of $\Lambda = \frac{\pi}{\Delta k}$, the calculated error is only 2.4%.

In the simulations for the $\chi^{(3)}$ nonlinear code, a Huygens source was again used to excite a propagating wave that originates from a slab waveguide and continues through the nonlinear dielectric medium. In Figure 2.3, the electric field profile of such a propagating wave is shown for the case of a bulk $\chi^{(3)}$ material with normalized $\chi^{(3)} = 1$. As shown in the figure, the wave is excited by the source in the slab waveguide to the right of the computational domain and propagates from left to right in the nonlinear medium. A qualitative observation of the diagram indicates that the lensing effect of the material focuses an initially divergent beam and causes the light to converge near the middle of the computational domain.

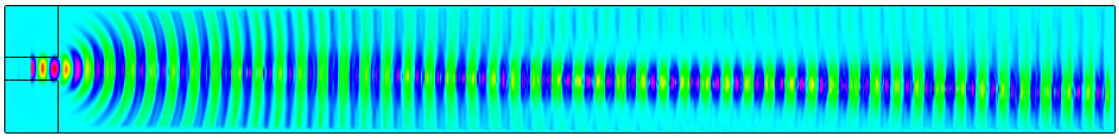

Figure 2.3. Self-focusing of a beam radiating out of a dielectric slab waveguide by using a bulk $\chi^{(3)}$ nonlinear medium. The fundamental guided mode of the slab waveguide is excited using a Huygens' source, and the structure is surrounded by PML boundaries. The spatial pattern of the electric field throughout the structure calculated by the nonlinear 2D FDTD code demonstrates the self-focusing effect.

The numerical verification of the $\chi^{(3)}$ nonlinear code was somewhat more complicated than the $\chi^{(3)}$ case, and was performed using the formula for the well-known phenomenon of self-phase modulation. The index of refraction n is the square root of the permittivity, which in this case may be written as

$$n = n_0 + \delta n = \sqrt{\varepsilon_r + \chi^{(3)}|\mathbf{E}|^2} \approx n_0 + \frac{\chi^{(3)}}{2\sqrt{\varepsilon_r}}|\mathbf{E}|^2, \tag{2.22}$$

where ε_r is the relative permittivity and n_0 is the linear refractive index. Self-phase modulation arises from the δn term, which changes the local effective index of the material in proportion to the square of the electric field strength**.**

If a plane wave incident upon a material exhibiting third-order nonlinearity is considered, the z-component of the electric field for a TE-polarized wave (i.e. electric field normal to the 2D computation plane, which is the x-y plane) has the form

$$E_z = A\cos(kx + \phi) = A\cos(\omega n x + \phi), \tag{2.23}$$

where A is the amplitude, k is the wavenumber, ω is the angular frequency, x is the position along the propagation direction, and φ is a phase constant. Here, the speed of light in vacuum is normalized to $c = 1$. In these simulations, a plane wave can be well approximated by the unidirectional traveling wave excited by the Huygens source far from the end of a waveguide, as seen from Figure 2.4. If the phase term φ is neglected,

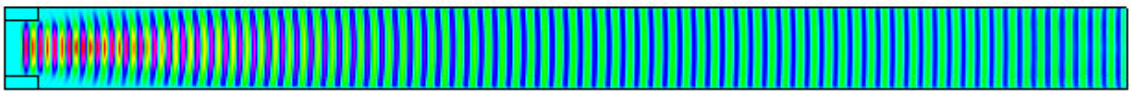

Figure 2.4. Structure used to produce plane-wave excitation of bulk nonlinear $\chi^{(3)}$ material for numerical self-phase modulation verification. The spatial pattern of the electric field throughout the structure calculated by the linear 2D FDTD method is shown, with a plane-wave-like pattern produced at the rightmost end of the domain.

which is valid as long as the nonlinear field component is relatively weak, the second derivative of E_z can be approximated as

$$\begin{aligned} \frac{dE_z}{dx} &= -\omega n A \sin(\omega n x) \\ \frac{d^2 E_z}{dx^2} &= -\omega^2 n^2 A \cos(\omega n x) \end{aligned} . \tag{2.24}$$

If the second derivative is then divided by the original field and the square root taken the refractive index can be written as

$$n = \sqrt{\frac{-\frac{d^2 E_z}{dx^2}}{\omega^2 E_z}} . \tag{2.25}$$

Shifting of the calculated values due to the phase constant and discrete differentiation may be accounted for by considering the peaks of the numerator and denominator terms under the square root, as shown:

$$n = \sqrt{\frac{\max\left(-\frac{d^2 E_z}{dx^2}\right)}{\max\left(\omega^2 E_z\right)}} . \tag{2.26}$$

An additional issue that must be accounted for is the extra harmonic components present in E_z for the nonlinear case [52], which likely result from the fact that the spatial variation of the phase term ϕ can no longer be ignored when large values are chosen for $\chi^{(3)}$. The electric field in this case is not perfectly sinusoidal, resulting in distortion of the calculated second derivative. This extra harmonic effect is shown in Figure 2.5a, which depicts the variation of E_z and $-d^2E_z/dx^2$ with the FDTD grid position (or x) at a fixed time within a $\chi^{(3)}$ material with normalized $\chi^{(3)} = 4$ (the field values were normalized to 1). This can be overcome by filtering the field values using a low-pass filter such that

only the fundamental harmonic component remains, as shown in Figure 2.5b, which displays the same data as in Figure 2.5a after the filtering process has been applied.

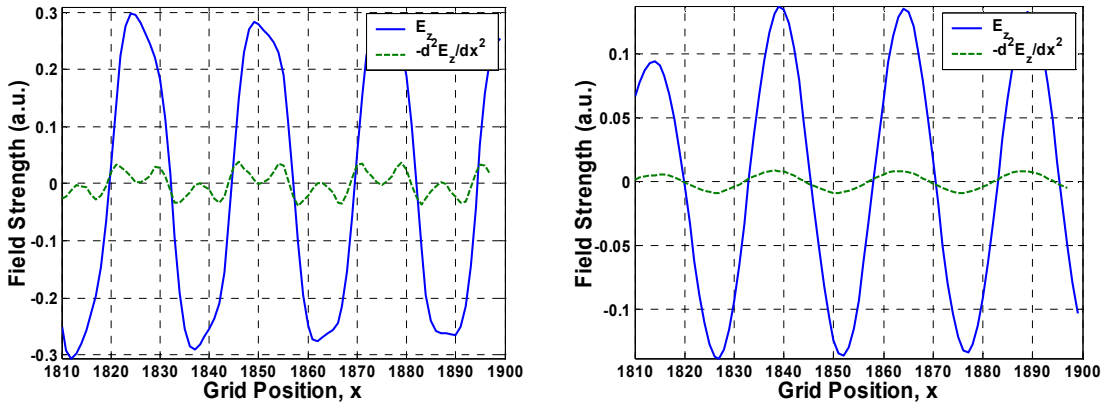

Figure 2.5. a. Variation of the out-of-plane (or z) component of the electric field (E_z) calculated using the nonlinear FDTD method and its second derivative with position (x) along the guiding direction within a $\chi^{(3)}$ nonlinear bulk material with normalized $\chi^{(3)} = 4$. The structure is excited by a plane wave with normalized frequency $a/\lambda = 0.265$ and TE polarization. **b.** Variation of the filtered out-of-plane electric field component (E_z) and its second derivative with position (x) along the guiding direction within a $\chi^{(3)}$ nonlinear bulk material with normalized $\chi^{(3)} = 4$. The structure is excited by a plane wave with normalized frequency $a/\lambda = 0.265$ and TE polarization.

Using Eq. (2.21), δn may now be calculated by subtracting the value of the linear refractive index from the refractive index obtained numerically from Eq. (2.26). Notice that the maximum of the squared E_z values from the FDTD simulation results was used in the calculation, although the average value is assumed in the theoretical analysis; the average field intensity can be related to the maximum field intensity through:

$$\left\langle |\mathbf{E}|^2 \right\rangle = |\mathbf{E}|^2_{\max} / 2 . \tag{2.27}$$

Comparing the simulation results (Eq. (2.26)) with the analytical expression for n (Eq. (2.22)), the values agree to within 12% error. The permittivity values may also be compared directly, eliminating the approximation used to separate the square-root terms in Eq. (2.22). The values using this approach agree to within only 2.6% error, much

smaller due to the fact that the error in truncation of the binomial expansion of Eq. (2.22) is no longer introduced.

2.5 Mode source in 3D FDTD

A critical component of the FDTD simulation tool is the mode source [49], which is a radiating electromagnetic source used to excite the guided modes of a slab waveguide. Although the simplest active source that can be implemented in FDTD is a dipole source, such a source has limited applications since it radiates in all directions and does not match the spatial profile of the guided modes of a slab waveguide. A mode source is more appropriate for studying the propagation properties of finite-length waveguides, including photonic crystal waveguides, and in the case of a 2D slab has an explicit form for the transverse-electric (TE) and -magnetic (TM) modes. Unfortunately, in the full 3D form, no explicit form can be found even for a simple slab waveguide.

One way to implement a 3D mode source is to approximate the field profile in the proximity of the waveguide, and then allow the field to propagate in the waveguide long enough that only the desired mode remains; i.e. until the unguided components of the initial field have radiated away from the waveguide region. Such a source is defined in a place perpendicular to the waveguide and slicing through it. As seen in Figure 2.6, five regions are defined, namely the waveguide core and the rectangular regions above, below, to the right, and to the left of the core. Four possible distinct refractive indices are allowed for the core, upper cladding, lower cladding, and the claddings to the right and left of the core, which are assumed to have the same index. Analogous to the 2D case, the modes of this type of waveguide are assumed to be one of two polarizations: E_x,

where H_x is zero and E_y is assumed to be negligible; or E_y polarized, where H_y is zero and E_x is negligible. The field profiles for the electric and magnetic field components in the core of the waveguide are sinusoids that have arguments that are functions of the refractive index and the geometric dimensions of the waveguide (i.e. *a* and *b*) [53]. The profiles for the other four regions are exponentially decaying sinusoids with similar arguments including phase terms to smoothly match with the field values for the core.

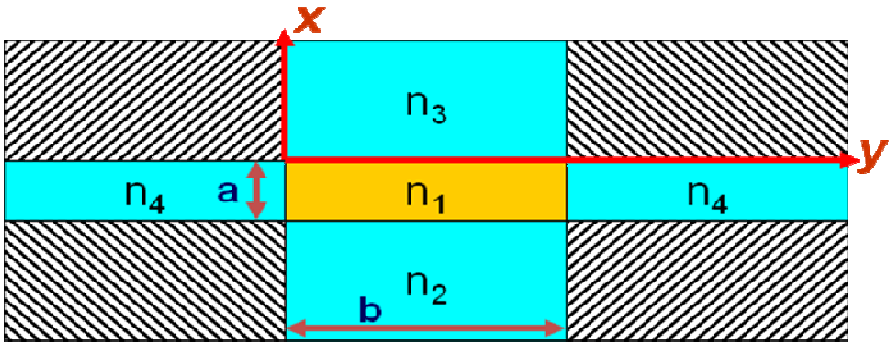

Figure 2.6. Computational domain in the region surrounding the waveguide core (center) showing the regions where the mode source is defined and their respective refractive indices, denoted as n_1, n_2, n_3, and n_4.

The E_x field profile of such a mode is shown in Figure 2.7, where PML terminating conditions were used on all six boundaries, and an index of 2.9 was used for the waveguide core (n_1) and 1.0 for the remaining regions (n_2 through n_4). The simulation has been run in this case for only a few time steps so that the development of the propagating waveguide mode can be observed. As seen in the figure, the mode is propagating bi-directionally from the initial surface plane within the waveguide, and converges to profile of the guided mode of the waveguide within only a few grid cells.

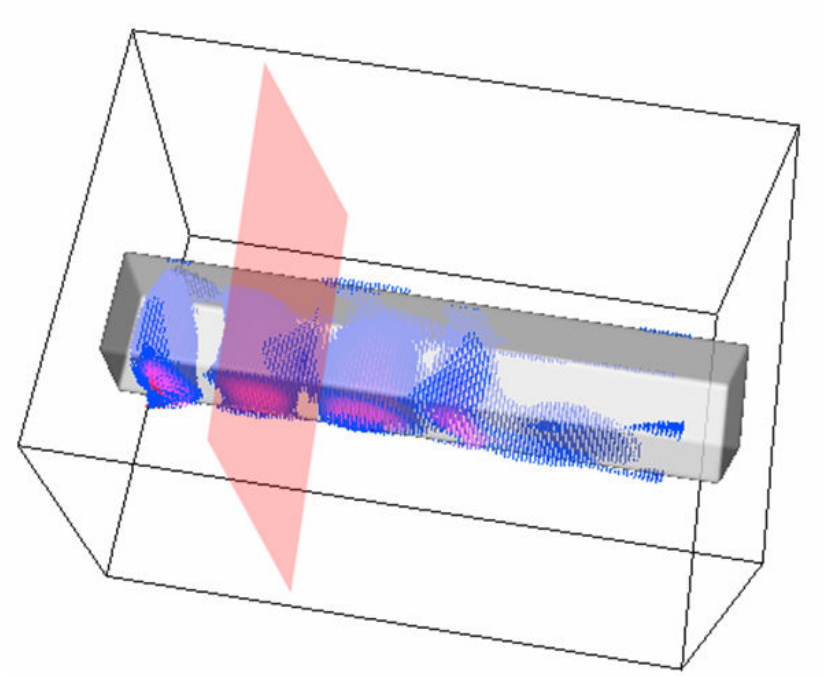

Figure 2.7. 3D field profile of a mode source propagating bi-directionally in a slab waveguide; the plane where the source was defined is highlighted.

2.6 FDTD optimization

The FDTD technique is a powerful tool for studying light propagation in the time domain, but is also notorious for its large computational and storage requirements. This becomes a critical factor for extended structures such as waveguides, and can make full 3D problems all but intractable even on the fastest workstation. Fortunately, the FDTD technique is quite compatible with parallel computing due to its inherent "data parallel" nature. This means that the computational domain can be divided in a straightforward manner between several processors, which can then perform their calculations individually on their portion of the domain. Thus, not only can the computational loaded be divided among numerous processors working simultaneously, but the storage burden can be divided as well, theoretically increasing the maximum size of the domain that can be simulated by almost a factor of n, where n is the number of available processors. The

first step in parallelizing the code was to optimize the serial version for maximum performance. After careful analysis of the timing profiles and the data structure of the serial code, it was determined that the largest computation load was incurred while performing the update calculations for all of the field values at each time-step. Since the original code used 3D matrices to store these field values, the memory access time could be significantly shortened by vectorizing the matrices and streamlining the memory access. The reason for this is that accessing the values in order enables the processor to preload values from memory into the quickly-accessible cache. A two- to three-fold improvement in computation time was achieved by this method for the serial code, as seen in Figure 2.8; this enhancement carries over directly to the parallel version.

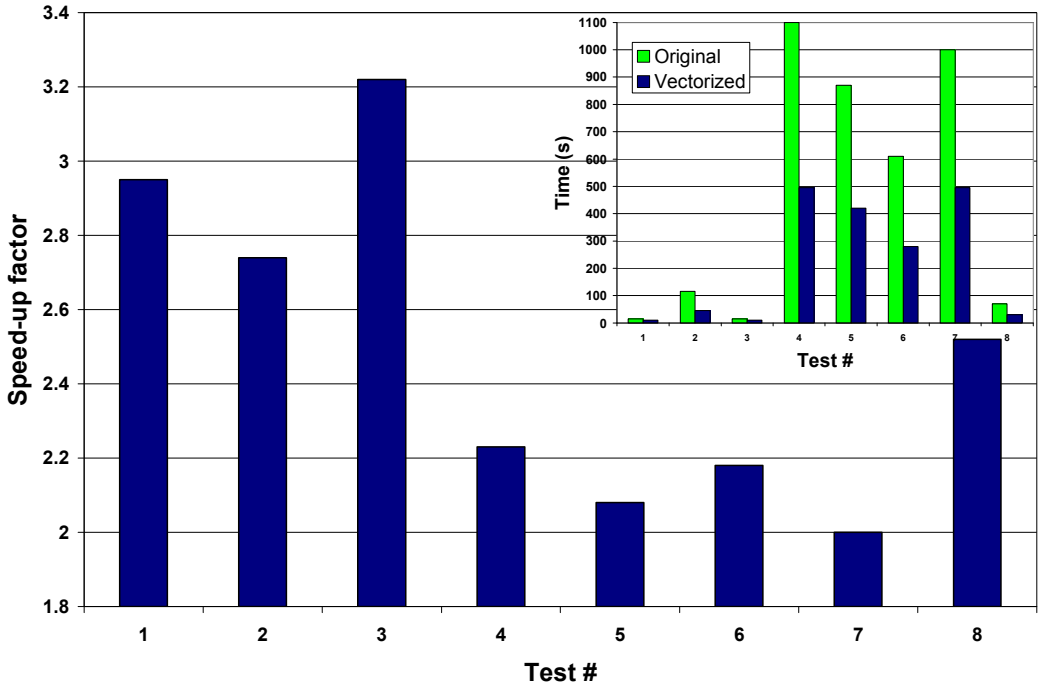

Figure 2.8. Improvement factor of the serial FDTD code for 8 different representative test cases. Inset: Simulation run time for the same 8 different test cases for the matrix (original) and vectorized optimization of the code.

The parallelized version of the 3D FDTD has been developed, which includes all of the features of the serial FDTD and has been implemented using the Message Passing Interface (MPI) library. MPI allows for a large degree of flexibility in programming style and is available for a wide variety of computer architectures and operating systems. The code was parallelized by dividing the computational domain into slices perpendicular to one of the axes, and then using one processor per slice to calculate all of the necessary field components. The memory usage was optimized such that each processor only stores the portion of computational domain that it needs for its own calculations, not the entire domain. The parallel code has been tested using a cluster of 16 dual-processor machines at Georgia Tech, as well as the state-of-the-art Oak Ridge National Laboratory Institutional Cluster (OIC), which has 320 dual-processor nodes for a total of 640 processors. The speed-up factor is plotted in Figure 2.9 versus the number of processors

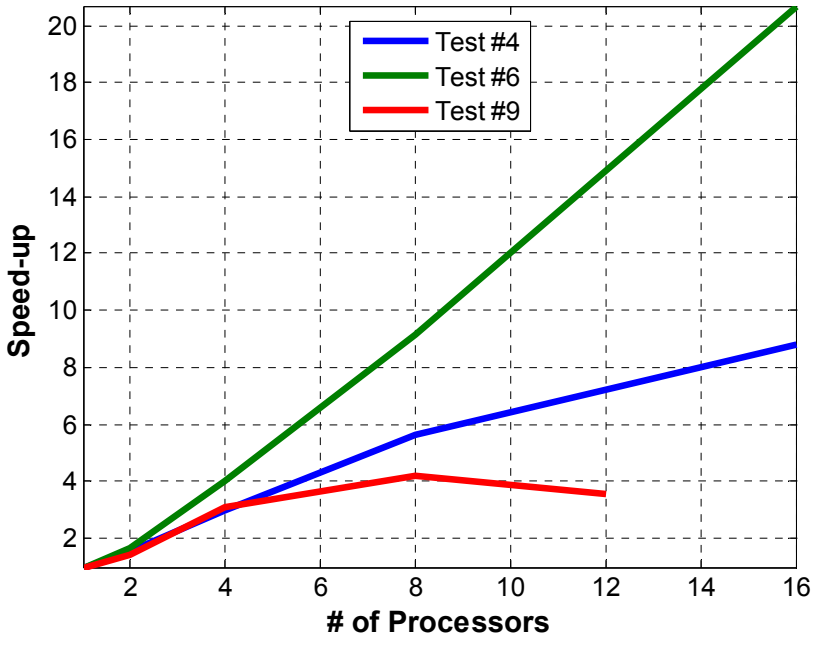

Figure 2.9. Speed-up factor (serial run time divided by parallel run time) for the initial version of the parallel FDTD code versus the number of processors for 3 of the test cases.

for 3 representative test cases. The overall speed-up scaled very well with the number of processors for the smallest computational domain (Test #6), but very poorly for the largest (3D) test case, Test #9. In fact, the speed-up factor actually decreased for Test #9 when using 12 processors, as compared to when only 8 processors were used. This indicated that the computational load was poorly balanced among the processors, as evidenced by the difference between the longest time taken by any processor and the average processor run time. A straightforward method improve the load balancing was to use only one processor to open, write, and close the files used for the calculated output field values. This eliminated the time-consuming opening and closing of files by the processors that store the desired field values, while the other processors are forced to wait before performing any further operations. The communications overhead added by these processors now having to send their data to a "master" processor is offset by the gain in having only one processor handle all disk I/O operations. The results of this optimization are shown in Figure 2.10 below, where the speed-up factor is shown to now increase monotonically for all of the test cases. Again, test cases #6 and #8 use 2D domains (#6 is the smallest) and the largest test case, #9, uses a 3D domain. Overall the change was small; however, even though the smallest test case ran slightly slower for larger numbers of processors, it is significant that the largest test case no longer performs worse for 12 processors than for 8 (Figure 2.9), as it did with the previous version. This indicates that the load balancing was improved, and the speed-up factor for the largest domains no longer saturates prematurely.

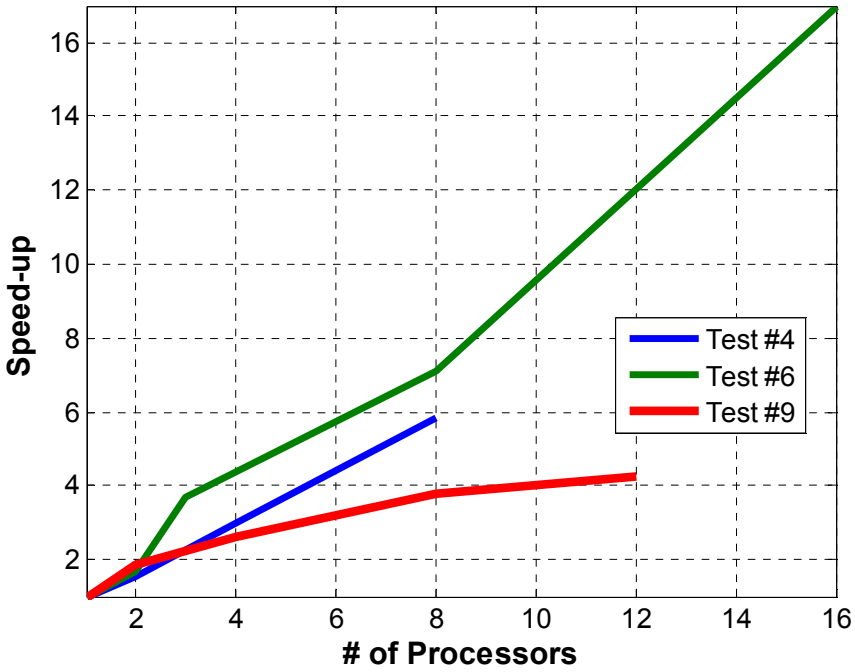

Figure 2.10. Speed-up factor (serial run time divided by parallel run time) for the optimized version of the parallel FDTD code versus the number of processors for the same 3 test cases.

Another performance benchmark performed was the characterization of the floating-point operations per second (FLOPS) performance of the 3D FDTD code. The FLOPS gives an indication of how much processor time is spent performing numerical calculations, as opposed to branches (logical operations), integer operations, etc. Thus, the efficiency of the code in terms of optimal use of the processor's power can be determined. The results of the characterization are shown in Figure 2.11, where the MFLOPS performance and processor time is plotted for each of the nine simulations used previously to test the serial code. Two different versions of the code were tested: the "old" version was the code without the parallelized output file writing, and the "new" version was the code with the parallelized output. As seen in the figure, the code performance did not change much when the output was parallelized, and even improved

slightly for some test cases. This is significant because the parallel performance was greatly improved with only a slight overhead added in the single-processor case. Also note that the MFLOPS performance for the smaller test cases (Tests #1-3 and 8) is much better than for the larger test cases, even passing the average benchmark performance reported [54] for this architecture (~1250 MFLOPS) for Test #1. Although the peak performance at about 1300 MFLOPS is still short of the maximum benchmark of almost 1600 MFLOPS, the code appears to be very well optimized.

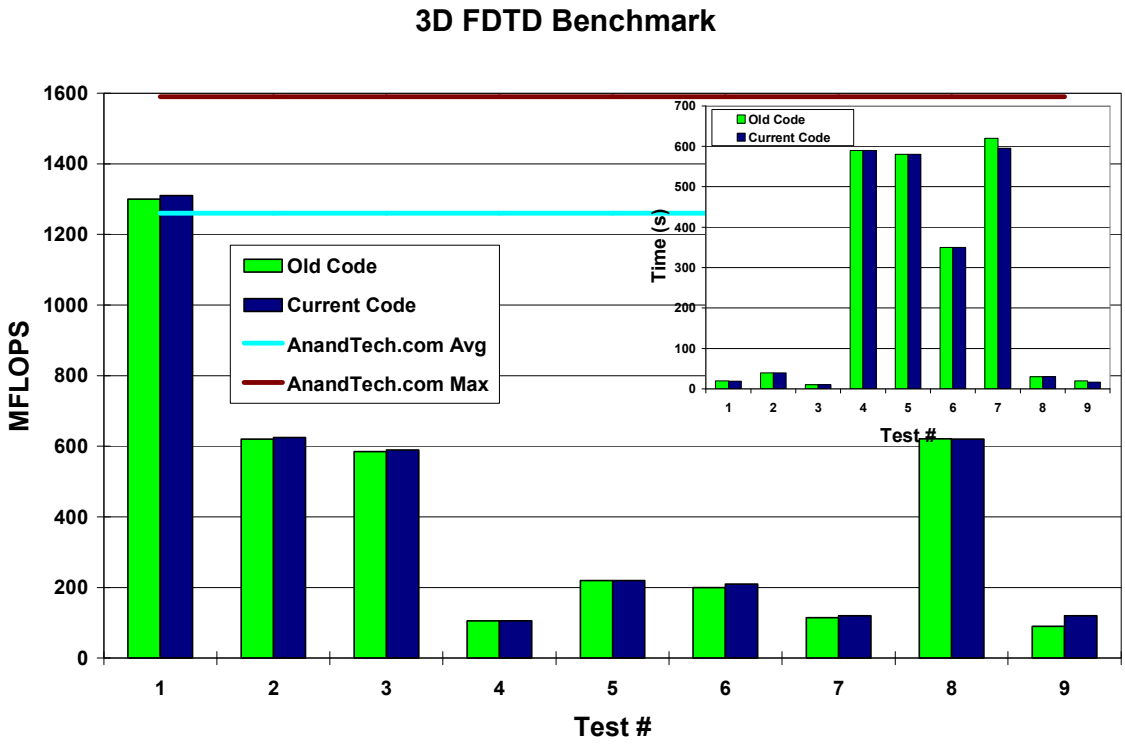

Figure 2.11. MFLOPS performance and processor time (inset) of the serial 3D FDTD code for nine different test simulations.

CHAPTER 3

GREEN'S FUNCTION-BASED COMPLEX BAND ANALYSIS

3.1 Green's Function Based Propagation Loss Analysis

A brute force technique such as FDTD can be used to study propagation loss in photonic crystal (PC) structures; however, but it has certain disadvantages, such as requiring extensive computation resources, especially when simulating extended structures like waveguides, and providing output data that include relatively little intuition. Thus, a semi-analytical tool is desirable, since the computational demands can often be reduced and additional intuition into the nature of the problem is provided. An analytic Green's function-based approach has been published [55] to this end, but it requires several lengthy calculations in addition to using a brute-force technique for calculating the band structure.

The general algorithm of the layer Korringa-Kohn-Rostoker (KKR) method [56],[57] is a powerful and flexible platform for studying the properties of electronic and photonic systems. Layer-KKR has been applied to numerous electronic problems to calculate the transmission of the system [58]-[61]. It has also been used to calculate the reflection and diffraction properties of photonic systems [62]-[64], but not for loss analysis. This technique has been previously adapted to use a layer-plane-wave basis, which is the same plane-wave basis of the layer-KKR code [65]. That derivation used the Green's function and Lippmann-Schwinger equation, but used only a one-dimensional Green's function, which cannot adequately describe the electromagnetic behavior of PCs. In fact, there has been no previously published work on the application of layer-KKR

theory to study loss in PC structures. The power of this approach is that is only requires calculation of the complex band structure of a given PC structure, from which the transmission (and loss) can be directly deduced. In this chapter, a Green's function-based technique in full 3D vector form is presented for the analysis of propagation loss in PC structures.

The semi-analytical approach for studying scattering loss in PC structures using the layer-KKR method with the Green's function starts with the unit cell of the PC. A slab of dielectric material is considered with a periodic spatial distribution of the dielectric constant $\varepsilon(\vec{r})$ with periodicity a in the x direction. The periodicity of the PC allows the infinite structure to be mapped to a system of periodic unit cells. This is completed by repeating the unit cell of the PC structure, which includes some defect, and inserting computation "absorbing layers" between adjacent cells, creating a supercell [66], as shown schematically in Figure 3.1. The defect is a model of the loss mechanism that is being studied and can be any arbitrary arrangement of $\varepsilon(\vec{r})$. The absorbing layers are needed to eliminate the multiple internal reflections within each cell that would

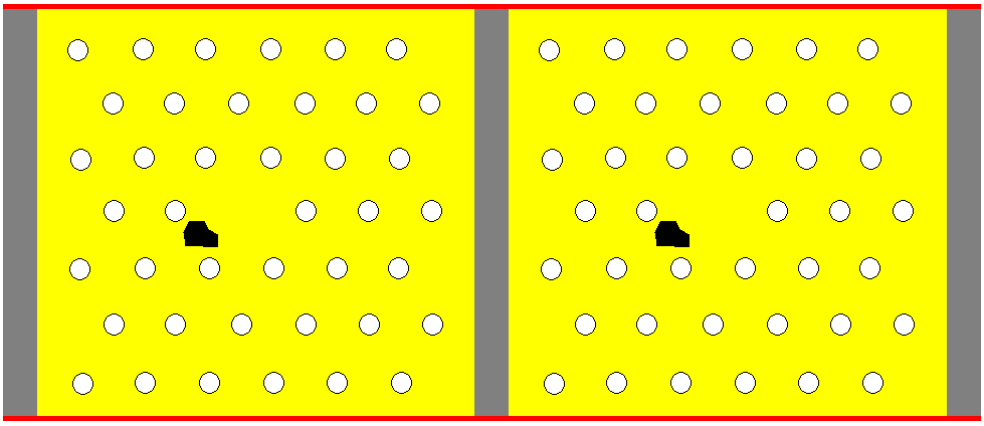

Figure 3.1. Schematic of the supercell structure used for the layer-KKR framework; the absorbing layers are shown in gray, the PC structure in yellow (high-permittivity material) and white (low-permittivity material), and the defect in black.

inappropriately change the physics of the problem by creating a system of infinitely repeating defects, instead of the desired single defect. To remove the effects of the absorbing layers on the band structure of the PC structure, a system with just the absorbing layers (i.e. without any PC layers) must also be simulated and the resulting wavevector solution subtracted from that of the PC-absorbing layer supercell. The expansion of the governing layer-KKR theory using the Green's function to include vector electromagnetic fields is described next.

From the Lippman-Schwinger equation, the right-going scattered wave function for a single wave incident from the left $\vec{E}_{0R}(\vec{r})$ can be written as

$$\vec{E}_R(\vec{r}) = \vec{E}_{0R}(\vec{r}) + \int_J d^3\vec{r}\,'\vec{\vec{G}}(\vec{r} \mid \vec{r}\,')k^2[\varepsilon(\vec{r}\,') - 1]\vec{E}_R(\vec{r}\,'), \tag{3.1}$$

where the integration is over the single layer *J*, k is the wavenumber, and the tensor $\vec{\vec{G}}(\vec{r} \mid \vec{r}\,')$ is the dyadic Green's function. Here, the Green's dyadic satisfies

$$\nabla \times [\nabla \times \vec{\vec{G}}(\vec{r} \mid \vec{r}\,')] - k^2\vec{\vec{G}}(\vec{r} \mid \vec{r}\,') = \delta(\vec{r} - \vec{r}\,')\vec{\vec{I}}\,. \tag{3.2}$$

For $\vec{r}$ outside of layer *J*, the Green's dyadic [67] can be expanded as

$$\vec{\vec{G}}(\vec{r} \mid \vec{r}\,') = \begin{cases} 4\pi \dfrac{\sum_n \overline{\vec{F}}_n(\vec{r}\,') \otimes \vec{F}_n(\vec{r})}{\Lambda_n(k_n^2 - k^2)}, x < x_J \\ 4\pi \dfrac{\sum_n \overline{\vec{F}}_n(\vec{r}) \otimes \vec{F}_n(\vec{r}\,')}{\Lambda_n(k_n^2 - k^2)}, x > x_J + a \end{cases}. \tag{3.3}$$

where Λ_n is a normalization coefficient and $\vec{F}_n(\vec{r})$ is the expansion basis function. By substitution, this leads to

$$\vec{E}_R(\vec{r}) = \begin{cases} \vec{E}_{0R}(\vec{r}) + \sum_n r_n \vec{F}_n(\vec{r}), x < x_J \\ \sum_{n'} \overline{\vec{F}}_{n'}(\vec{r}) t_{n'}, x > x_J + a \end{cases}, \tag{3.4}$$

for the right-going electric field, where $r_n = \int d^3\vec{r}' f_n \overline{\vec{F}}_n(\vec{r}') \vec{E}_R(\vec{r}') k^2 [\varepsilon(\vec{r}') - 1]$, $t_{n'} = \delta_{n'}(\vec{r}') + \int d^3\vec{r}' f_{n'} \vec{F}_{n'}(\vec{r}') \vec{E}_R(\vec{r}') k^2 [\varepsilon(\vec{r}') - 1]$, and $f_n = \frac{4\pi}{\Lambda_n (k_n^2 - k^2)}$. A similar formulation can be found for the left-going field $\vec{E}_L(\vec{r})$, which is the scattered field from an incident wave from the right $\vec{E}_{0L}(\vec{r})$.

These scattering solutions can be combined to find the transmission and reflection coefficients of the transfer matrix for the structure. The transmission and reflection probabilities are calculated from the transfer matrix in the form of the Schrödinger equation and from this the loss in terms of the complex wave vectors. Thus, any mode analysis methods can be used to calculate the complex band structure of the PC (e.g., plane-wave expansion or finite element). Once this information is gathered, the propagation loss of the PC is given from the simple formula

$$\begin{aligned} T &= e^{-2\lambda} \\ \lambda &= \left| \Im(k_n a) - \Im(k_0 a_0) \right|, \end{aligned} \tag{3.5}$$

where a_0 is the periodicity of the supercell used to calculate the band structure.

3.2 Complex-band simulations

To confirm the validity of the complex-band theory, the transmission behavior of a simple PC waveguide (PCWG) was studied. A triangular-lattice PC was chosen because of its large bandgap with a hole radius of 30% of the periodicity and a waveguide

was formed by removing one row of the air holes in the high-permittivity material. A reference calculation was made using the 2D version of the FDTD code described in Chapter 2; a Gaussian pulse source was used to provide a band of frequencies wide enough to cover the bandgap of this structure. The computational domain is shown in Figure 3.2, where the mode profile of the normal PCWG has been calculated (Figure 3.2a) as well as the profile for the same waveguide but with a small defect added to on of the holes, circled in white (Figure 3.2b). It is clear that the mode profiles are significantly different despite the small size of the defect, qualitatively highlighting the

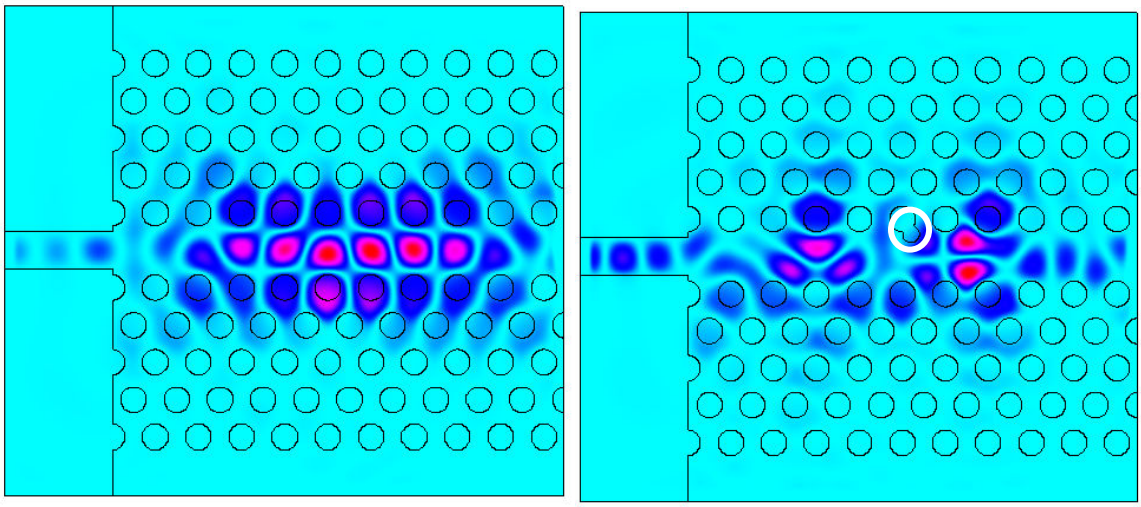

Figure 3.2. Mode profiles from FDTD of a triangular-lattice W1 PCWG **a.** without and **b.** with a defect (circled in white), highlighting the effect of the relatively small defect on the propagation of the guided modes.

problem of fabrication defects deteriorating the propagation behavior of PCWGs. The effects of the defect can be seen quantitatively in the transmission plots for the two waveguides, shown in Figure 3.3. Here, the transmission band for the waveguide without a defect starts above the mode gap around $a/\lambda = 0.27$ in normalized frequency and extends to the upper edge of the bandgap, at around $a/\lambda = 0.35$. When the defect is

introduced, the transmission outside of the transmission band remains largely unchanged; however, a strong dip is observed in the transmission band with a peak at approximately $a/\lambda = 0.32$.

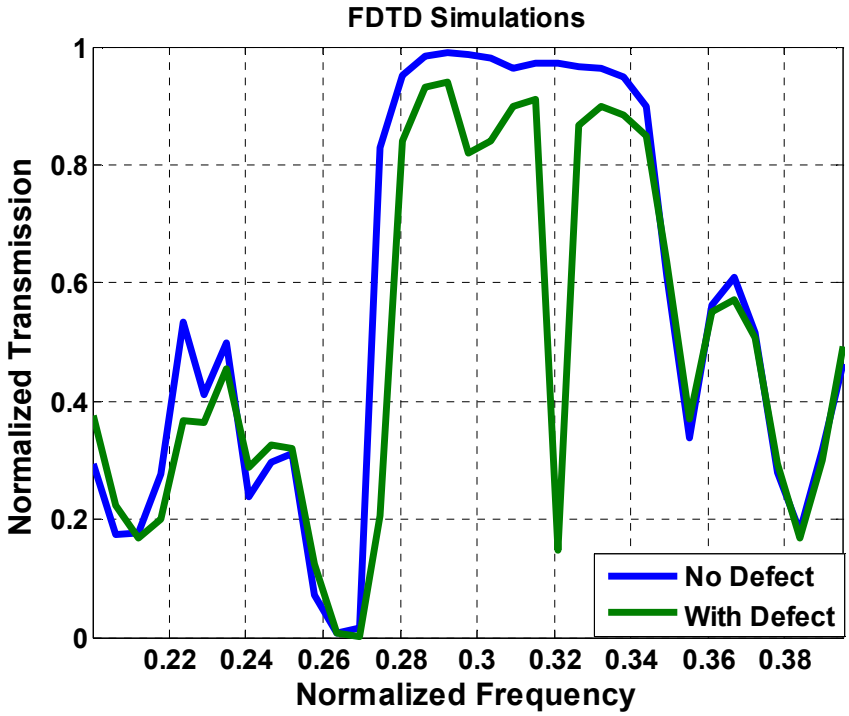

Figure 3.3. Transmission plot of the PCWG shown in Figure 3.2 with and without the defect, calculating using FDTD.

The technique that has been chosen to calculate the complex band structure of the PCWGs is the plane-wave expansion (PWE) method [68], which is a common technique for calculating the band diagrams for PC structures. PWE solves Maxwell's equations for infinitely periodic structures by expanding the electromagnetic field with plane waves and turning the equations into an eigenvalue problem. Thus, the complex band behavior for the triangular-lattice PCWG with a single defect was calculated using this technique. The computation domains used for the PWE simulations is shown in Figure 3.4; the unit cells are indicated in white. The supercells are separated by using perfectly-matched

layer (PML) absorbing boundary conditions on the left and right boundaries of the domains.

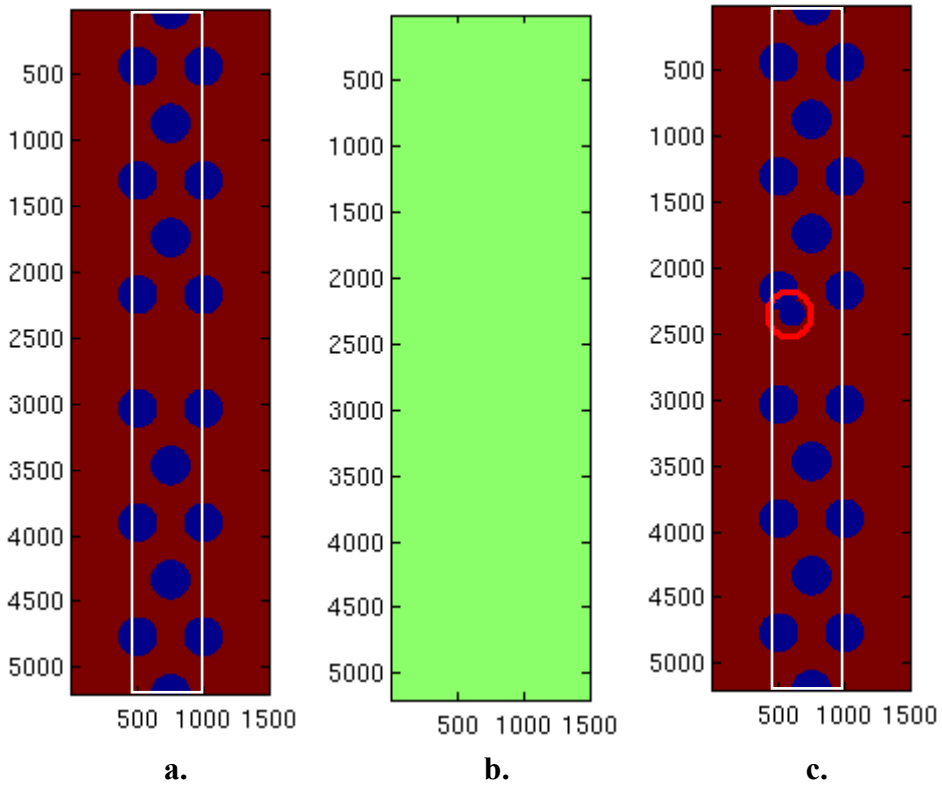

Figure 3.4. Computational domains used in PWE for the **a.** supercell structure without a defect, **b.** reference structure (PML only), and **c.** supercell structure with the defect (circled in red). The unit cells for the waveguide structures are highlighted in white.

There are a couple of difficulties in reproducing the transmission results obtained from the brute-force calculations. One issue is that while the Green's function-based complex band theory presented thus far is exact, the PWE is an approximate numerical technique. This means that the accuracy of the simulation results is dependent upon the number of plane waves used to expand the electromagnetic fields in the structure (which determines the computational demands to complete a given simulation). Another problem is the optimization of the formulation for the PML absorbing boundary conditions to maximize the isolation between the virtual adjacent cells produced by the

periodic assumption made by the PWE method. The PML is implemented by adding an imaginary component to the refractive index, which has the effect of introducing material loss. While the profile of the imaginary component can be arbitrary, different forms produce varying amount of absorption and reflection. The mathematical of the PML was optimized using a form that provided good results in earlier reported work [66]. This model uses a $1/x$ form, resulting in a cross-section profile for the imaginary part of the permittivity as shown in Figure 3.5. The reflectivity from the boundary layers has been greatly reduced using this PML, while maximizing the absorption.

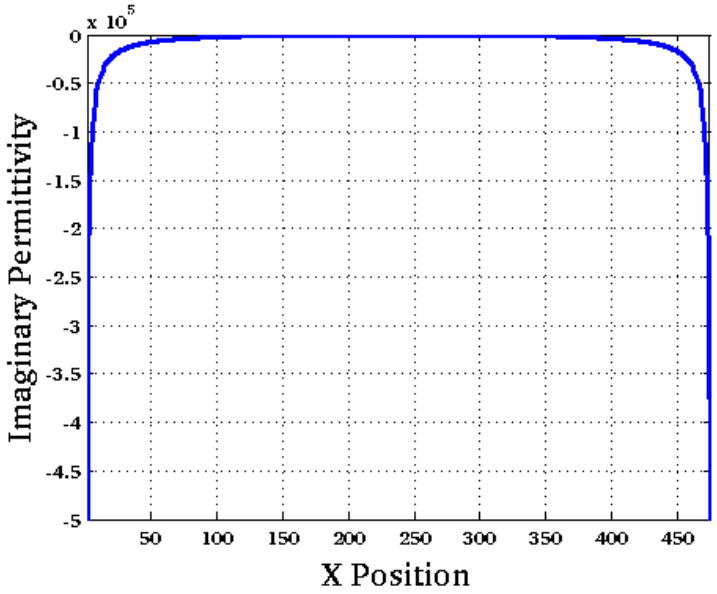

Figure 3.5. Cross-section profile of the PWE computation domain sliced in the guiding direction of the PCWG, showing the 1/x form of the complex permittivity for the PML.

Another important note is that the complex-mode technique calculates the transmission (or loss) for only one mode of the structure. This has two implications; the first is that the transmission for the complex band calculations may not exactly match the FDTD results, particularly for a multi-mode structure. This is especially noticeable when certain guided modes of a PCWG are highly lossy as compared to others. The second

issue is that the technique requires that the same mode be used in the Eq. (3.5) for the structure and the reference simulation results. Since the simulation output assigns an arbitrary order to the modes, it is often not immediately obvious which values to use. Thus, careful analysis of the output data is necessary to produce meaningful and accurate transmission results.

Bearing these caveats in mind, the transmission from the complex-band calculations using PWE for the lowest $Re\{k\}$ mode, designated Mode 1, is shown in Figure 3.6a. A transmission band can be observed centered at about $a/\lambda = 0.33$ similar to the FDTD results, although much narrower in bandwidth, and the mode gap and smaller transmission peak at the lower frequencies are present as well. A dip for the defect case is present in the mode gap here, too, at about $a/\lambda = 0.33$ (as compared with $a/\lambda = 0.32$ using FDTD). Nevertheless, the curves do not match exactly as a result of the mode-based nature of the complex-band technique. The facts that a slab waveguide that is required for the FDTD excitation and that the simulated PCWG has finite length of the (as compared to the infinite structure used in PWE) contribute to the discrepancies,

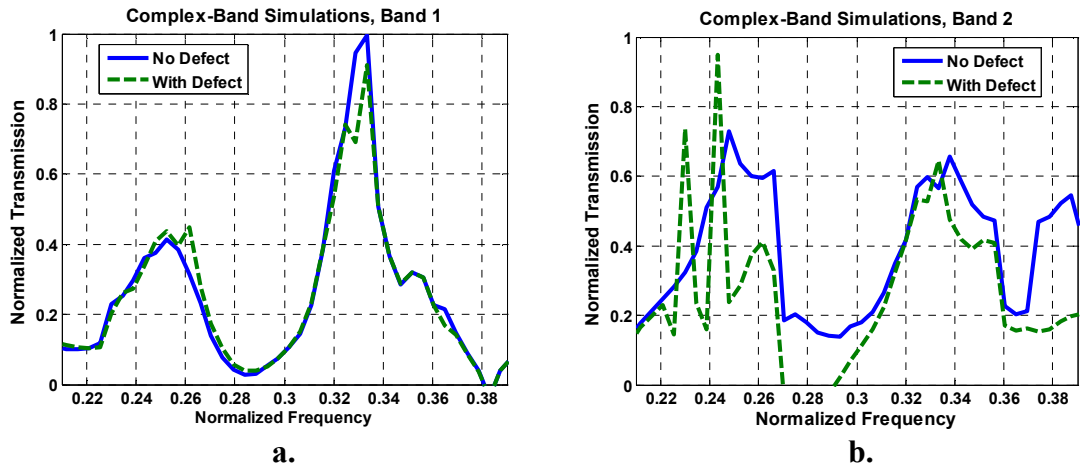

Figure 3.6. Transmission of the triangular-lattice PCWG calculated using complex-band analysis with PWE for **a.** the mode designated 1 and **b.** mode 2.

particularly by introducing a small frequency shift to the transmission curves. The primary reason for the observed differences, though, is that the FDTD calculations include all of the possible modes of the structure together, while the PWE calculations consider each mode individually. Thus, all of the modal spectra calculated using this technique would have to be superimposed to generate comparable results as those from FDTD. However, this actually highlights one of the advantages of this technique, since the transmission (or loss) contributions of each mode can be analyzed individually using the complex-mode approach. This can be seen in Figure 3.6b, where the calculated transmission for another mode, designated Mode 2, has been plotted. Again, the high transmission band around $a/\lambda = 0.33$ is seen, now with a width more comparable to the results from the FDTD calculations. The transmission peak at the lower frequencies is more pronounced now, although with a slight dip near the center similar to the FDTD curve. Also, the somewhat erratic peaks at the lowest frequencies for the waveguide with the defect indicate that there the mode is not well-defined in that structure, and are most likely spurious. However, this demonstrates the power of the ability to identify the contributing factors of individual modes to the transmission characteristics, which can be very useful for structures with inherently complex mode behavior, such as PCWGs.

Thus far, only one defect has been considered in these proof-of-principle simulations. However, in general, the problem of fabrication defects is not manifested as a single defect but as a random distribution of perturbations to the geometrical properties of the PCWG. The layer-KKR technique used in the previous section to derive the complex-band method can be extended in a straightforward manner to handle this very situation. This extension is commonly referred to as the Korringa-Kohn-Rostoker

coherent potential approximation (KKR CPA), and has been widely used to calculate the electronic band structure of polycrystalline metal alloys [69],[70]. The technique handles random material properties by substituting an ordered lattice of effective materials for the varying properties of the random material. An ensemble-averaged Green's function is used in this case, which can be written in the form [71]

$$\left\langle \vec{\vec{G}}(\vec{r} \mid \vec{r}') \right\rangle = \frac{4\pi}{\Lambda_n (k_n^2 - k^2)} \left[\sum_n \vec{\vec{F}}_n(\vec{r}') \otimes \left\langle \tau_n \right\rangle \vec{F}_n(\vec{r}) - \sum_n \vec{F}_n(\vec{r}') \otimes \vec{K}_n(\vec{r}) \right], \qquad (3.6)$$

where $\left\langle \tau_n \right\rangle$ denotes the scattering matrix for the defect at the *n*th site, and $\vec{K}_n(\vec{r})$, like $\vec{F}_n(\vec{r})$, is a solution to Eq. (3.2) and is continuous at the boundary of layer *J*. The probability distribution is determined by the experimental statistics describing the defects typical for a given fabrication process, and is introduced into a structure defined by distinct two materials having a low and high permittivity, denoted ε_L and ε_H, respectively, via structure composed of materials that have an effective permittivity with a value $\varepsilon_L <= \varepsilon_{eff} <= \varepsilon_H$. By averaging over all possible values at each site *n*, the Green's function can be written as

$$\left\langle \vec{\vec{G}}(\vec{r} \mid \vec{r}') \right\rangle = \frac{4\pi}{(k_n^2 - k^2)} \left(\begin{array}{l} \sum_n \left[C_H \vec{\vec{F}}_n^H(\vec{r}') \otimes \left\langle \tau_n \right\rangle \vec{F}_n^H(\vec{r}) + C_L \vec{\vec{F}}_n^L(\vec{r}') \otimes \left\langle \tau_n \right\rangle \vec{F}_n^L(\vec{r}) \right] \\ - \sum_n \left[C_B \vec{F}_n^B(\vec{r}') \otimes \vec{K}_n^B(\vec{r}) + C_L \vec{F}_n^L(\vec{r}') \otimes \vec{K}_n^L(\vec{r}) \right] \end{array} \right), \qquad (3.7)$$

where C_H and C_L denote the concentrations of the defects of permittivity ε_L and ε_H, respectively. This implies that a random distribution of defects can be analyzed by simulating a structure with fixed defects that are assigned values based on a probability distribution. Thus, the statistics of the defect distribution can be handled by a single simulation, as opposed to the multiple simulations with different orientations of randomly placed defects as would be necessary with the popular Monte Carlo method. This is

likely where the greatest advantages in computation demand will be realized over other techniques such as FDTD.

CHAPTER 4

PHOTONIC CRYSTAL-BASED MULTI-FUNCTIONAL DEVICES

4.1 Introduction to photonic crystal devices

The term photonic crystal (PC) is a term used to describe a periodic arrangement of dielectric materials that can modify the propagation behavior of light within a certain range of frequencies [21]. They can be though of as the optical analogue of semiconductors, which can similarly be used to engineer the behavior of electrons, and thus have been extensively investigated in literature [72]-[77]. Using the anomalous dispersion inherent to propagating waves in a PC, effects such as negative refraction, superprism effect, and diffractionless propagation have been observed. Alternatively, PCs have inspired much interest with their unique ability to control light propagation and emission through the photonic band gap (PBG), a range of frequencies within which light cannot propagate in the material [78]-[80]. A number of devices can be engineered by adding defects to the PC, such as cavities [81] (using, e.g., point defects) and waveguides [82] (using line defects). Planar two-dimensional PCs are excellent candidates for integrating the functions such as waveguides, resonators, filters [83], and couplers onto a single chip to form small-footprint photonic circuits [84]. Due to their large band gaps, triangular-lattice PC waveguides (PCWGs), which are formed by removing one row of air holes (W1) from the otherwise perfect triangular-geometry PC lattice, are attractive for forming the backbone of such photonic circuits [85].

4.2 Tunable nonlinear PC drop filter

Since PC structures can support electromagnetic modes with highly-confined modal profiles and drastically differing dispersion properties, the introduction of nonlinear materials into PC structures has led to many interesting nonlinear optical phenomena [86]-[98]. The can be applied to a device such as the channel drop filter based on PC cavities and waveguides, shown in Figure 4.1. Two cavities, formed by modifying the radii of a few of the holes, couple the input waveguide (excited by a slab waveguide on the left) to the drop waveguide above it [99]. This structure has two degenerate modes at the resonant frequency if the cavities are identical, due to interactions between the two cavities. Thus, at the resonant frequency of the cavities, light in the lower waveguide will be unidirectionally coupled to the upper waveguide.

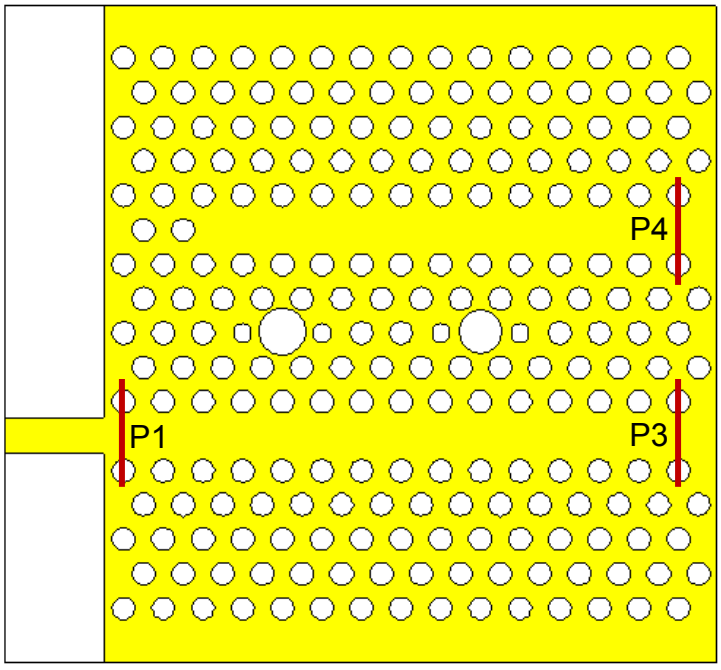

Figure 4.1. Schematic of a 3-port PC drop filter using two degenerate cavities; the material having $\varepsilon_{GaAs} = 12.96$ is shown in yellow and $\varepsilon_{polymer} = 2.25$ in white.

If the hole material is considered to have third-order nonlinear properties, the device behavior can be modified based on the intensity of the propagating beams. Since normalized parameters are used in the FDTD code used for the simulations, changing the light intensity can be modeled to a good approximation by instead changing the value of $\chi^{(3)}$ used in the simulations. The high-permittivity material, i.e. a semiconductor, was assigned $\varepsilon = 12.96$, and the low-permittivity material in the holes was assigned $\varepsilon = 2.25$ (typical for many nonlinear polymers); the material in all of the holes was assigned $\chi^{(3)}$ nonlinearity to model the practical case of a PC infiltrated with a nonlinear polymer. A hole radius of $r/a = 0.3$ is used for the bulk PC, and each cavity is created by enlarging a hole to $r/a = 0.6$ and decreasing the radii of the hole immediately to the left and right of the enlarged hole to $r/a = 0.25$. The nonlinear material has the effect of shifting the center frequency of the resonance as the $\chi^{(3)}$ strength is increased resulting in a small modulation of the drop power, as seen in Figure 4.2a. However, if the degeneracy of the two-cavity system is broken by slightly perturbing the radius of one of the larger cavity holes to $r/a = 0.55$,

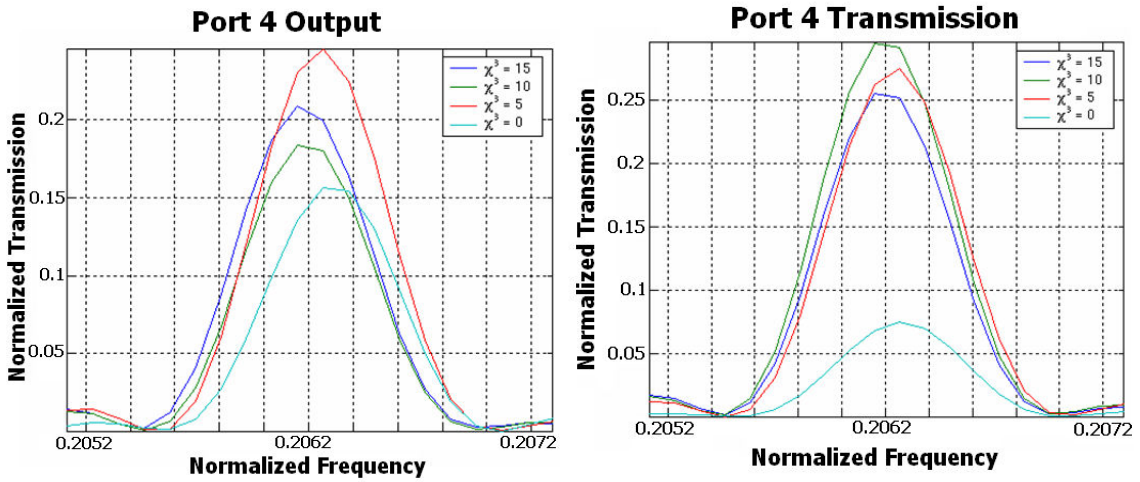

a. **b.**

Figure 4.2. Drop port transmission at frequencies near resonance for different $\chi^{(3)}$ strengths for **a.** two degenerate cavities and **b.** two cavities with broken degeneracy.

the cavity resonances are shifted by differing amounts by the nonlinear material and the modulation of the dropped power becomes larger. As seen in Figure 4.2b, there is a much more significant change of about 6.2 dB in the peak transmission between the linear and the case of $\chi^{(3)} = 10$, as compared with the structure with the degenerate cavities. This change in the transmission behavior versus the $\chi^{(3)}$ strength can also be observed from field profile, where the transmission for the non-degenerate cavities is shown in Figure 4.3a for the linear case and Figure 4.3b for the nonlinear case of $\chi^{(3)} = 10$. The transmitted power has clearly shifted in the latter case from straight-through transmission (port 3) to being dropped to port 4 by the filter. Note that the linear transmission for the non-degenerate cavities is greatly reduced from the degenerate structure due to the lack of a common resonance frequency for the two cavities.

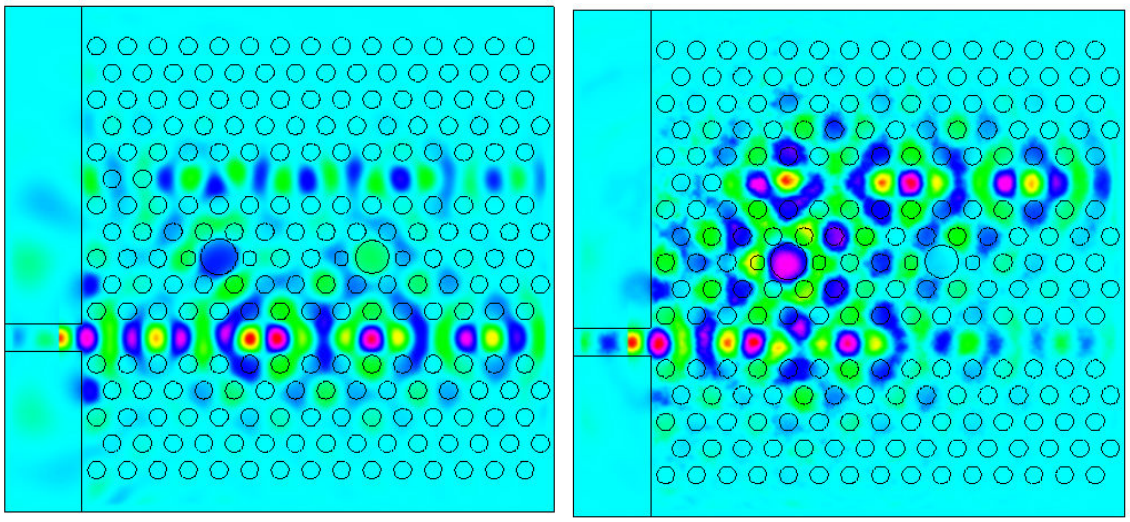

a. **b.**

Figure 4.3. Field profiles of the PC drop-filter with $\chi^{(3)}$ nonlinear material in the holes and with nondegenerate cavities for **a.** $\chi^{(3)} = 0$ and **b.** $\chi^{(3)} = 10$.

4.3 Photonic crystal-based design template

In an attempt to compose a general design that can be easily engineered for a variety of functionalities, a PC-based four-port device has been constructed that allows for a high degree of flexibility and resonant effects, shown in Figure 4.4. This device, composed of two doubly-crossed bent PC waveguides in a triangular lattice, can be configured to provide arbitrary power splitting among the four ports when one is used as an input. The eight holes located at the waveguide bends and crossings, referred to here as cavity holes, can be tuned (size, position, material, etc.) to modify the transmission properties of the device. The positions of these holes at the intersections of two PCWGs make them ideal foci for nonlinear interactions among multiple input beams, for example four-wave mixing effects. The possibility even exists for switching action, where two ports are used as inputs: one as a control beam and a second input as the signal beam. Perhaps one of the most interesting applications of this device involves placing nonlinear material in the cavity holes, particularly C3 and C6 (see Figure 4.4), to produce output at

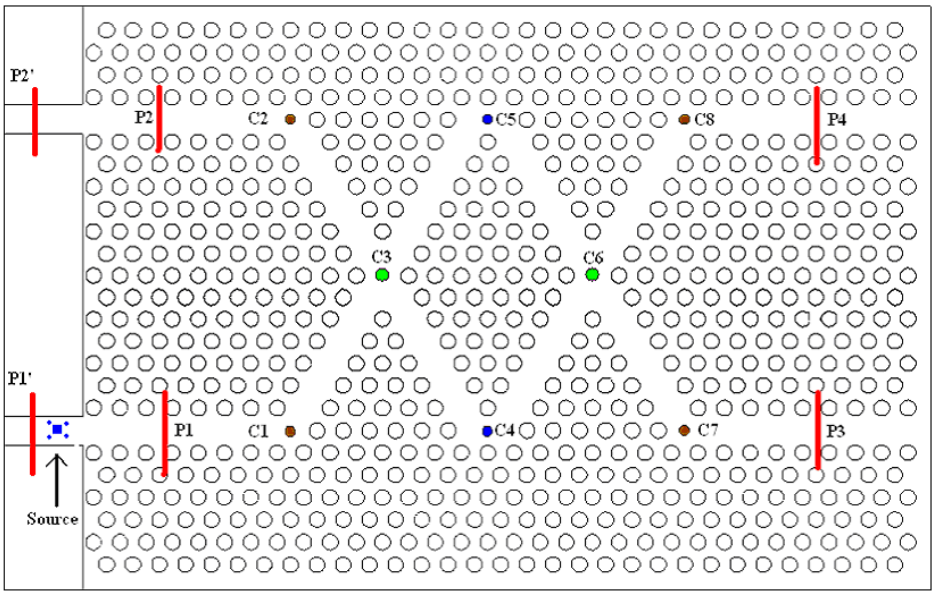

Figure 4.4. Schematic of the four-port PC crossed-waveguide structure, highlighting the eight tunable cavity holes C1-C8; the observation surfaces are shown in red.

the four ports that varies with the input power.

The transmission behavior of the linear device was calculated using the 2D FDTD code, as shown in Figure 4.5. The materials were assumed to be air holes (ε = 1.0) in a semiconductor (ε = 7.9), and the holes have a radius of r/a = 0.3 except for cavity holes C1, C2, C4, C5, C7, and C8, which have a radius of r/a = 0.2. While the transmission spectra are rather complex, they demonstrate the flexibility of the device to provide arbitrary functionalities based on the modification of only a few parameters. As an

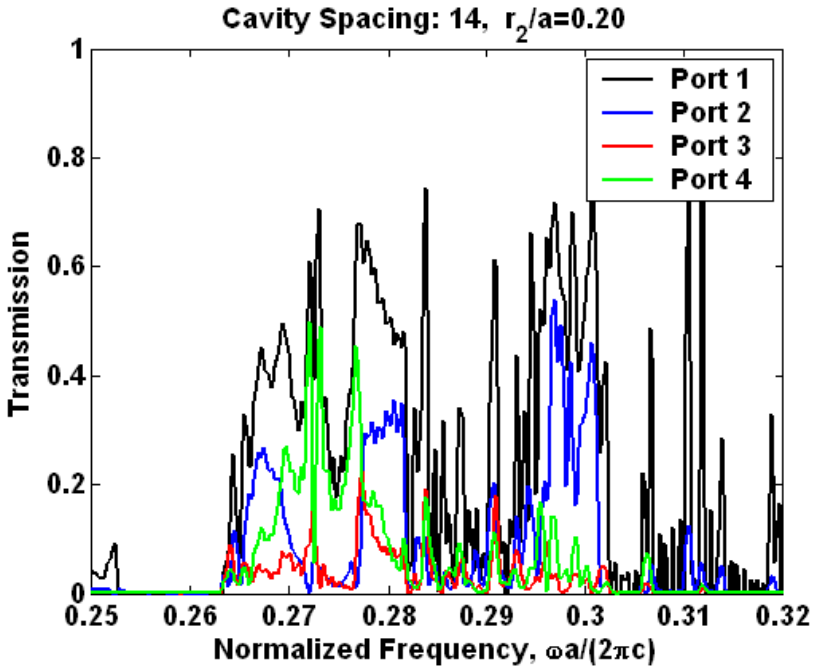

Figure 4.5. Transmission curves for the four ports of the multifunctional PC structure for r/a = 0.2 for holes C3 and C6 and r/a = 0.3 for all other holes.

example of how the transmission properties of this device can be tailored to different application, two devices with different hole radii for cavity holes C3 and C6 were simulated (Figure 4.6). Only linear materials were used for this simulation, and a hole

radius of r/a = 0.30 was again used for the bulk PC while r/a = 0.2 was used for cavity holes C1, C2, C4, C5, C7, and C8. However, the hole radius for holes C3 and C6 were r/a = 0.3 for the structure shown in Figure 4.6a and r/a = 0.2 for the one in Figure 4.6b. As seen in the mode profiles, the power (input through port 1) is predominately routed to port 4 at a frequency of a/λ = 0.2769 in the first design, while the power is distributed almost evenly among ports 2 through 4 at a frequency of a/λ = 0.2773 in the second.

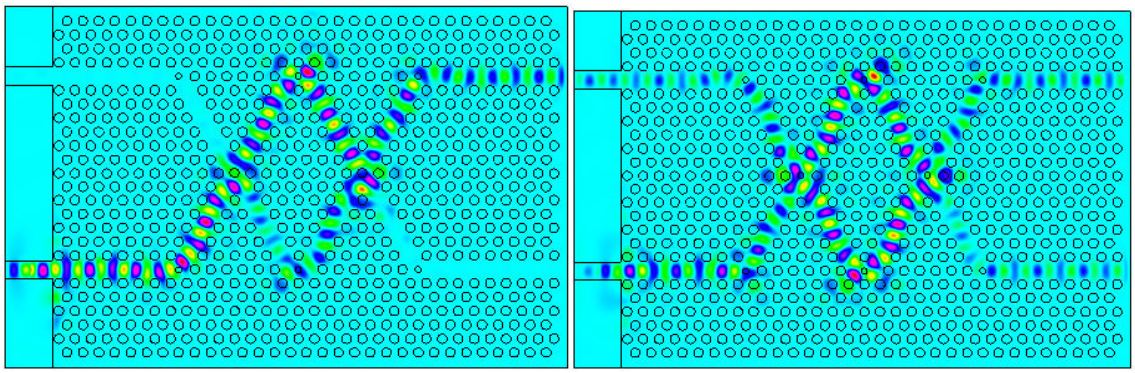

Figure 4.6. Field profiles of the four-port structure demonstrating **a.** power routing from port 1 to port 4 and **b.** power splitting from port 1 to ports 2, 3, and 4.

This type of behavior can be useful for applications where a single functionality is required from each device. However, is tunability is desired, the device must be modified in some way, for example by using nonlinear effects. One way to accomplish this is to assume that a $\chi^{(3)}$ nonlinear material can be infiltrated in to the holes of the PC. The behavior such a device is shown in Figure 4.7, where holes C3 and C6 have a modified radius of r/a = 0.2 and the excitation frequency is a/λ = 0.2773. The linear transmission (Figure 4.7a) is the same as Figure 4.6b, with approximately equal power splitting among ports 2 through 4. The nonlinear transmission with $\chi^{(3)}$ = 10 (Figure 4.7b) demonstrates that for sufficiently high field intensity and nonlinearity, the functionality can be changed to primarily routing power to port 4. This illustrates the

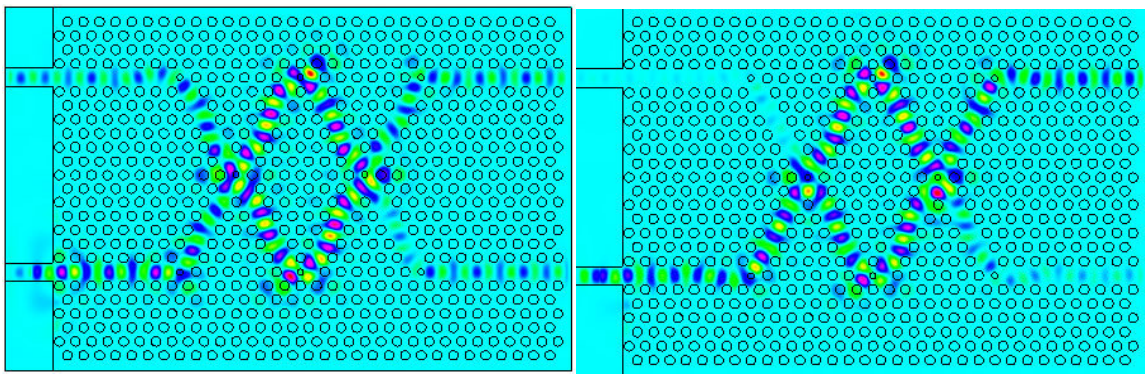

a. **b.**

Figure 4.7. Field profiles of the nonlinear four-port structure demonstrating **a.** splitting from port 1 to ports 2, 3, and 4 for the linear case and **b.** power routing primarily from port 1 to ports 4 for $\chi^{(3)} = 10$.

potential for switching or all-optical logic using this device design.

To confirm the practicality of this PC design, a sample was fabricated and measured using the characterization test bench described later in Chapter 6. A scanning electron micrograph of the sample, designed with a periodicity a = 400 nm, is shown in

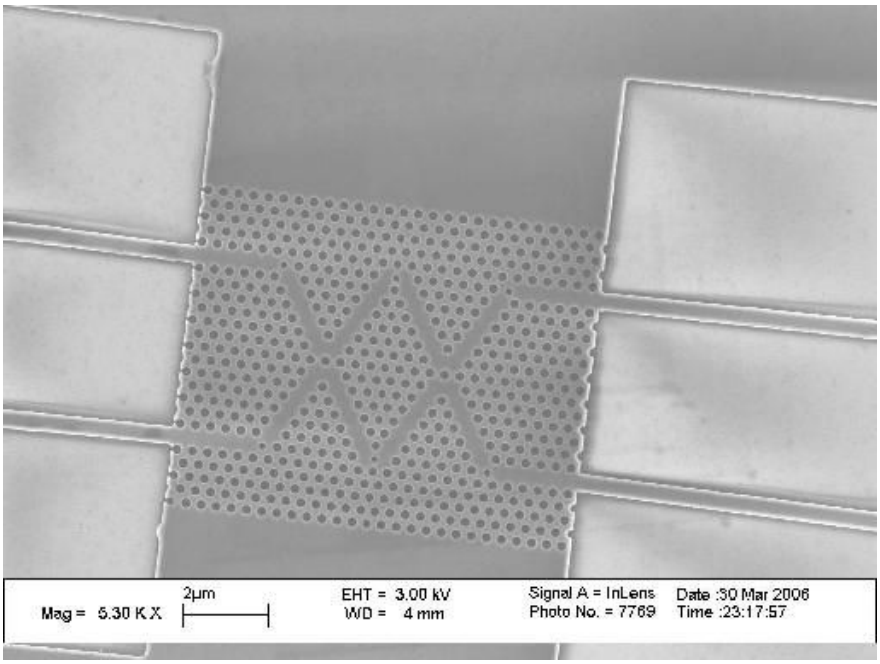

Figure 4.8. Scanning electron micrograph of the multi-functional PCWG sample; the period of the PC is 400 nm and the hole radius is 120 nm, except for cavity holes C1, C2, C4, C5, C7, and C8, which have a hole radius of 80 nm.

Figure 4.8. The hole radius was $r/a = 0.30$ for all of the holes except for cavity holes C1, C2, C4, C5, C7, and C8, which had a radius of $r/a = 0.20$. The slab waveguides used to excite the structure and rout the output light to the sample facet for measurement can also be seen in Figure 4.8; Port 2 is re-directed to output side (not shown) along with ports 3 and 4. The transmission spectra for the three output ports are shown in Figure 4.9. The blue, red, and green curves correspond to ports 2, 3, and 4, respectively; the reflection

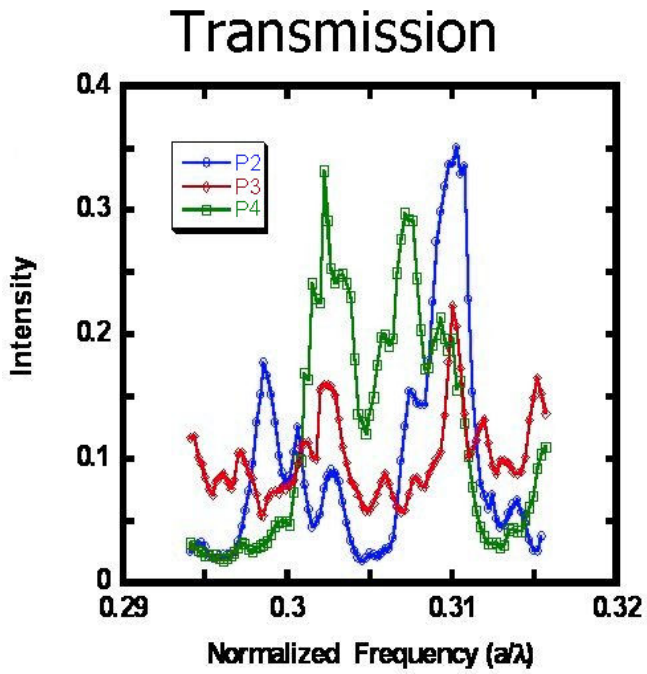

Figure 4.9. Measured transmission curves for the four ports of the multifunctional PC structure shown in Figure 4.8. The blue curve corresponds to port 2, the red curve to port 3, and the green curve to port 4.

(i.e. port 1) was not measured. Again, the complex behavior predicted by the theoretical simulations is clearly seen, although a direct correlation cannot be made due to differences caused by fabrication imperfections and the fact that a 2D simulation was used to approximate the behavior of a 3D structure. However, considering that one of the primary effects produced by these sources of error is a shift in the frequency of the measured transmission, the measured data in the range of $0.295 < a/\lambda < 0.310$ can be

compared with the calculated transmission (Figure 4.5) in the range of about $0.265 < a/\lambda < 0.280$. In this case, several similarities in the transmission features can be noted, such as the two strong peaks within this frequency range for port 4, and the strong transmission band seen for port 1 centered around $a/\lambda = 0.28$ in the plot for the simulation data. These measurements of an actual sample confirm the device behavior as predicted by 2D FDTD simulations.

CHAPTER 5

SECOND HARMONIC GENERATION USING CRITICAL COUPLING

5.1 Efficient Second Harmonic Generation

Planar integrated photonic components that exploit nonlinear optical phenomena are attracting attention from many researchers due to their potential for realizing chip-scale all-optical signal processing functionalities such as all-optical wavelength conversion, coupling, and switching [100]. Specifically, the second-harmonic generation (SHG) process [101] has drawn interest attention owing to its applications in ultrafast pulse measurement, microscopy, and switching [102]-[104]. Efficient second harmonic generation (SHG) is currently achieved in free-space optics using macroscopic nonlinear optical crystals, with over 30% single-pass conversion and 66% multi-pass conversion possible [105]. Clearly, however, such systems are unsuitable for photonic integrated circuit applications [106],[107], the photonic counterparts of microelectronic circuits, which require functionalities such as active switches and signal processing.

Numerous efforts have been made to realize efficient SHG in planar waveguide devices, using materials such as in lithium niobate [108]; however, fabrication constraints make nanoscale devices in such materials difficult and costly to produce. In addition, a major challenge to realize such planar structures has been the difficulty in satisfying the phase matching condition between the pump and the SHG waves. Phase matching is usually achieved in bulk systems using uniaxial crystals combined with angle tuning [109],[110]. In planar waveguides, phase matching has been achieved through techniques such as quasi-phase matching (QPM) with good conversion efficiencies [111].

However, since the second-harmonic process is quadratically proportional to the length of propagation in the nonlinear material, efficient SHG would require a long waveguide length that is incompatible with large scale integration. Thus, the need exists for a compact chip-scale device that can deliver highly efficient SHG. This chapter presents a highly efficient method of SHG in a traveling-wave resonator by critical coupling to a racetrack resonator.

5.2 Coupled-mode theory of optical resonators

The coupling between a waveguide and a resonator can be studied using coupled-mode theory. The guided wave behavior of this two-port device, as depicted in Figure 5.1, can be described by the coupling and transmission coefficients for the waveguide and the resonator [112] as

$$\begin{bmatrix} b_1 \\ b_2 \end{bmatrix} = \begin{bmatrix} t & \kappa \\ -\kappa^* & t^* \end{bmatrix} \begin{bmatrix} a_1 \\ a_2 \end{bmatrix}, \tag{5.1}$$

where t is the transmission coefficient and κ is the coupling coefficient from the

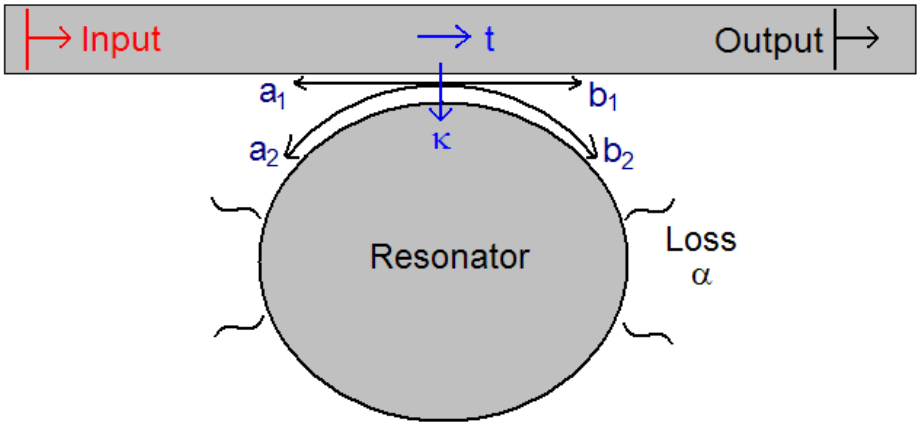

Figure 5.1. Diagram of a generic resonator side-coupled to a slab waveguide, showing the transmission, coupling, and loss coefficients.

waveguide to the resonator. The complex mode amplitudes a_1 and b_1 denote the backward and forward travelling waves in the waveguide, respectively, and likewise a_2 and b_2 represent the waves in the resonator. Note that the equations for this side-coupled configuration are independent of the actual type of resonator used (i.e., ring, microdisk, racetrack, etc.).

These complex amplitudes in Eq. (5.1) are normalized such that their squared amplitude corresponds to the modal power, and the coupling region is assumed lossless such that $|t|^2 + |\kappa|^2 = 1$. As a wave travels in the resonator, it experiences either loss or gain, depending on the sign of the loss coefficient α, which can be written as

$$a_2 = \alpha b_2 e^{i\vartheta}, \begin{cases} \alpha > 1, \text{loss} \\ 0 < \alpha < 1, \text{gain} \end{cases}, \tag{5.2}$$

where θ is the propagation phase accumulated in a single round trip. Eq. (5.1) can be combined with Eq. (5.2) to write

$$\begin{aligned} b_2 &= -\frac{\kappa^*}{1-\alpha t^* e^{i\vartheta}} a_1 \\ a_2 &= -\frac{\alpha\kappa^*}{e^{-i\vartheta} - \alpha t^*} a_1. \end{aligned} \tag{5.3}$$

The expression for a_2 from Eq (5.3) can then be substituted into Eq. (5.1) to find

$$b_1 = \frac{-\alpha + te^{-i\vartheta}}{e^{-i\vartheta} - \alpha t^*} a_1. \tag{5.4}$$

Critical coupling occurs when $\alpha = |t|$, meaning the loss in the resonator is equal to the magnitude of the coupling loss from the waveguide to the resonator at the resonant frequency (i.e. $t = e^{i\theta t}$ and $e^{-i\theta}\, e^{i\theta t} = 1$). Under these conditions, the transmission through the waveguide approaches zero and all of the power is dissipated inside the resonator. A plot of the transmission through the waveguide versus the coupling coefficient, given by

$T = \frac{(\alpha - \kappa)^2}{(\alpha + \kappa)^2}$ (at resonance) [114], is shown Figure 5.2; the loss coefficient has been fixed at a representative value of 0.5 for this plot. As expected, it can clearly be seen that the transmission is a maximum when there is no coupling to the resonator and zero at the critical coupling point where the coupling and loss strengths are equal.

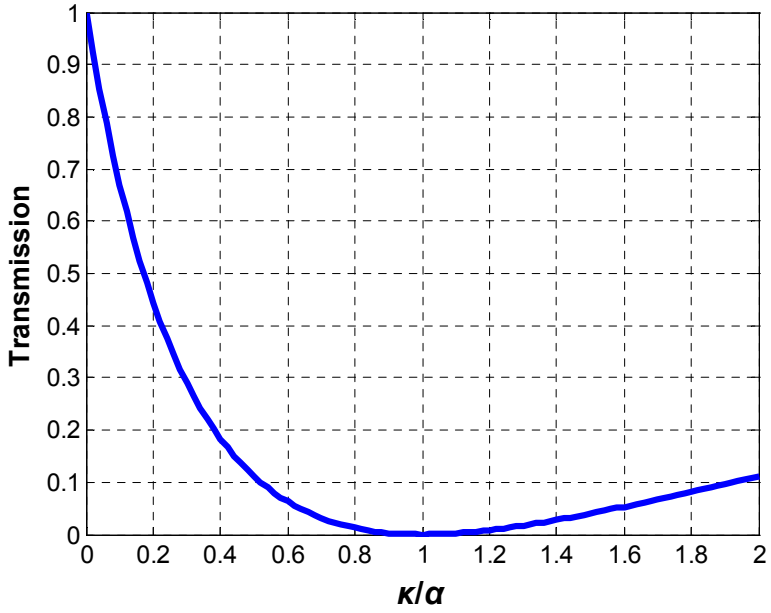

Figure 5.2. Plot of the transmission through a waveguide coupled to a resonator versus the ratio of the normalized coupling factor versus the normalized loss factor.

If all loss mechanisms other than SHG are ignored, and assuming that the fundamental (at frequency ω) and second harmonic (at frequency 2ω) waves are phase matched, the slowly-varying envelope approximation [113] can be written as

$$\begin{aligned} \frac{dE_\omega}{dz} &= -iDE_{2\omega}E_\omega^* e^{-i\Delta kz}, \\ \frac{dE_{2\omega}}{dz} &= -iDE_\omega^2 e^{i\Delta kz}, \end{aligned} \tag{5.5}$$

where E_ω and $E_{2\omega}$ are now used to represent the complex electric field amplitudes at frequencies ω and 2ω, and $D = \omega\sqrt{\frac{\mu}{\varepsilon_0}}\frac{1}{n}\varepsilon_0\chi^{(2)}$ and $\Delta k = k_{2\omega} - k_\omega$, where μ_0 is the free space permeability, ε_0 is the free space permittivity, n is material index of refraction, $\chi^{(2)}$ is the second-order nonlinear coefficient, and k_ω and $k_{2\omega}$ are the propagation constants in the resonator at frequencies ω and 2ω, respectively. This notation can be related to one used the previously by defining E^{in} and E^{out} as the electric field amplitudes at the input and output of the nonlinear region and equating $a_{2,\omega}$ to E_ω^{in} and $b_{2,\omega}$ to E_ω^{out} at the fundamental frequency, with corresponding variables for the second harmonic frequency. If the pump depletion is very small, i.e. $E_\omega^2 \sim (E_\omega^{in})^2$, then for a nonlinear region of length L:

$$\begin{aligned} &E_{2\omega}(z) = E_{2\omega}^{in} + \int_0^L dz\left[-iDE_\omega^2\right]e^{i\Delta kz} \Rightarrow \\ &E_{2\omega}^{out} - E_{2\omega}^{in} = DE_\omega^2\frac{1-e^{i\Delta kL}}{\Delta k}, \end{aligned} \tag{5.6}$$

and Eq. (5.6) can be substituted into Eq. (5.5) to find after again integrating:

$$E_\omega^{out} - E_\omega^{in} = DE_\omega^* E_{2\omega}^{in}\frac{1-e^{-i\Delta kL}}{\Delta k} + D^2\left|E_\omega\right|^2 E_\omega\frac{e^{-i\Delta kL}-1+i\Delta kL}{(\Delta k)^2}. \tag{5.7}$$

These equations describe the SHG process in the nonlinear region of the resonator.

Now, the coupled-mode theory for critical coupling can be combined with the standard coupled-mode theory for SHG. Two matrix expressions are used to describe the behavior at the fundamental and second harmonic frequencies:

$$\begin{aligned} \begin{bmatrix} b_{1,\omega} \\ b_{2,\omega} \end{bmatrix} &= \begin{bmatrix} t_\omega & \kappa_\omega \\ -\kappa_\omega^* & t_\omega^* \end{bmatrix}\begin{bmatrix} a_{1,\omega} \\ a_{2,\omega} \end{bmatrix}, \\ \begin{bmatrix} b_{1,2\omega} \\ b_{2,2\omega} \end{bmatrix} &= \begin{bmatrix} t_{2\omega} & \kappa_{2\omega} \\ -\kappa_{2\omega}^* & t_{2\omega}^* \end{bmatrix}\begin{bmatrix} a_{1,2\omega} \\ a_{2,2\omega} \end{bmatrix}. \end{aligned} \tag{5.8}$$

Here, the subscripts now also indicate whether the electric field at the fundamental or second harmonic frequency is under consideration. In terms of the loss coefficient α, now for frequencies ω and 2ω, we can write the electric field amplitudes entering and leaving the nonlinear region of the resonator as

$$\begin{aligned} a_{2,\omega} &= e^{i\vartheta_{\omega}}\alpha_{\omega}b_{2.\omega}, \\ a_{2,2\omega} &= e^{i\vartheta_{2\omega}}\alpha_{2\omega}b_{2.2\omega}. \end{aligned} \tag{5.9}$$

Using the definition $\delta_1 = D\dfrac{1-e^{i\Delta kL}}{\Delta k}$ and with the expansion of Eq. (5.8) and substitution, it can be determined for the input and output field amplitudes for the nonlinear region:

$$\begin{aligned} b_{2,2\omega}^{in} &= \frac{t_{2\omega}^{*}\alpha_{2\omega}e^{i\theta_{2\omega}}}{1-t_{2\omega}^{*}\alpha_{2\omega}e^{i\theta_{2\omega}}}\delta_1(b_{2,\omega})^2, \\ b_{2,2\omega}^{out} &= \frac{1}{1-t_{2\omega}^{*}\alpha_{2\omega}e^{i\theta_{2\omega}}}\delta_1(b_{2,\omega})^2, \\ a_{2,2\omega} &= \frac{\alpha_{2\omega}e^{i\theta_{2\omega}}}{1-t_{2\omega}^{*}\alpha_{2\omega}e^{i\theta_{2\omega}}}\delta_1(b_{2,\omega})^2, \\ b_{1,2\omega} &= \frac{\kappa_{2\omega}\alpha_{2\omega}e^{i\theta_{2\omega}}}{1-t_{2\omega}^{*}\alpha_{2\omega}e^{i\theta_{2\omega}}}\delta_1(b_{2,\omega})^2, \end{aligned} \tag{5.10}$$

where, $b_{2,2\omega}^{in}$ and $b_{2,\omega}^{out}$ are the field amplitudes at the second-harmonic frequency entering and leaving the nonlinear region of the resonator, respectively. By additionally defining $\delta_2 = -D^2\dfrac{e^{-i\Delta kL}-1+i\Delta kL}{(\Delta k)^2}$ and noting that $E_{2\omega}^{in} = b_{2,2\omega}^{in}, E_{\omega}^{in} = b_{2,\omega}^{in}$, and $E_{\omega}^{out} = b_{2,\omega}^{out}$, Eq. (5.7) can now be written as

$$b_{2,\omega}^{out} - b_{2,\omega}^{in} = -\left|b_{2,\omega}\right|^2 b_{2,\omega}\left[\left|\delta_1\right|^2 \frac{t_{2\omega}^* \alpha_{2\omega} e^{i\vartheta_{2\omega}}}{1 - t_{2\omega}^* \alpha_{2\omega} e^{i\vartheta_{2\omega}}} + \delta_2\right]. \tag{5.11}$$

By defining a nonlinear loss coefficient as $b_{2,\omega}^{out} = \alpha_{2,NL} b_{2,\omega}^{in}$, this can be written as

$$\begin{aligned} \alpha_{2,NL} &= 1 - \left|b_{2,\omega}\right|^2 \left[\left|\delta_1\right|^2 \frac{t_{2\omega}^* \alpha_{2\omega} e^{i\vartheta_{2\omega}}}{1 - t_{2\omega}^* \alpha_{2\omega} e^{i\vartheta_{2\omega}}} + \delta_2\right] \Rightarrow \\ \alpha_{2,NL} &= 1 - \left|b_{2,\omega}\right|^2 \frac{D^2 L^2}{2} \frac{1 + t_{2\omega}^* \alpha_{2\omega} e^{i\vartheta_{2\omega}}}{1 - t_{2\omega}^* \alpha_{2\omega} e^{i\vartheta_{2\omega}}}, \end{aligned} \tag{5.12}$$

where the top expression in Eq. (5.12) is the general case, and the bottom expression in Eq. (5.12) assumes that the fundamental and second harmonic waves are phase matched. Now, focusing on the fundamental frequency and noting that $\alpha_{2,\omega} = \alpha_{2,NL} \alpha_\omega e^{i\vartheta_\omega} b_{2,\omega}$, it can be found that

$$\begin{aligned} b_{2,\omega} &= \frac{-\kappa_\omega^*}{1 - t_\omega^* \alpha_{2,NL} \alpha_\omega e^{i\vartheta_\omega}} a_{1,\omega}, \\ b_{1,\omega} &= \frac{t_\omega - \alpha_{2NL} \alpha_\omega e^{i\vartheta_\omega}}{1 - t_\omega^* \alpha_{2,NL} \alpha_\omega e^{i\vartheta_\omega}} a_{1,\omega}. \end{aligned} \tag{5.13}$$

Given that $\alpha_{2NL} \alpha_\omega = \alpha_{0,\omega} - \alpha_{2,\omega} \left|b_\omega^2\right|^2$, where $\alpha_{0,\omega}$ is the intensity-independent loss and $\alpha_{2,\omega}$ is the intensity-dependent loss due to SHG (in general a complex number), critical coupling occurs when

$$\begin{aligned} t_\omega &= \left[\alpha_{0,\omega} - \alpha_{2,\omega} \left|b_{2,\omega}\right|^2\right] e^{i\vartheta_\omega} \Rightarrow \\ \left|b_{2,\omega}\right|^2 &= \frac{\alpha_{0,\omega} - t_\omega e^{-i\vartheta_\omega}}{\alpha_{2,\omega}}. \end{aligned} \tag{5.14}$$

If $\alpha_{2,\omega}$ is a real number (and thus frequency independent), θ_ω is determined by $t_\omega e^{-i\theta_\omega}$ being real, which is independent of $\left|b_{2,\omega}\right|^2$. Thus phase matching will be required with

$t_{2\omega} = 0$, and there will be no shift in the minimum transmission frequency. However, if $\alpha_{2,\omega}$ is complex, the value of θ_ω that minimizes $\left| t_\omega - \left[\alpha_{0,\omega} - \alpha_{2,\omega} \left| b_{2,\omega} \right|^2 \right] e^{i\theta_\omega} \right|$ will change with $\left| b_{2,\omega} \right|^2$ and in general result in a shift of the SHG frequency. Thus, it is expected that the peak of the SHG signal will occur at a frequency slightly shifted from the fundamental frequency multiplied by a factor of 2 (i.e., 2ω).

The structure chosen here to implement critical coupling with the SHG effect is a simple slab waveguide coupled to a racetrack resonator, as shown in Figure 5.3. For the purposes of this study, it is assumed that the nonlinear material is placed in the straight portion of the racetrack resonator farthest from the slab waveguide. The extended straight portions of the racetrack resonator provide an additional degree of freedom for tuning the coupling strength between the waveguide and resonator and allow for the round-trip length of the resonator (and thus the resonance frequency) to be changed independently of the bending radius (which effects the bending loss). This structure is also convenient because the coupling region between the waveguide and the resonator is spatially separated from the nonlinear region, thus simplifying the analysis of the device. To quantify the enhancement in SHG due to the racetrack resonator within the limit of phase-matching, consider the transmission through a straight slab of nonlinear material with no resonator, where Eq. (5.6) we can be simplified as

$$\left| b_{1,2\omega} \right| = \left| \delta_1 \right| \left| a_{1,\omega} \right|^2 . \tag{5.15}$$

This can be compared with the case when the resonator and critical coupling conditions are satisfied is present:

$$\left|b_{1,2\omega}\right| \approx \left|\delta_1\right| \frac{1}{\left|\kappa_\omega\right|^2} \left|a_{1,\omega}\right|^2, \tag{16}$$

and thus the enhancement due to the resonator is directly related to the coupling strength to the resonator can be calculated at as

$$\eta = \left[\frac{\left|b_{1,2\omega}\right|_{resonantor}}{\left|b_{1,2\omega}\right|_{no-resonantor}} \right]^2 = \frac{1}{\left|\kappa_\omega\right|^4}. \tag{5.16}$$

This indicates that the largest enhancement occurs when the coupling is small, which corresponds to a resonant mode that is strongly confined in the resonator and thus experiences more round-trips through the nonlinear material, multiplying its effects.

5.3 Simulation of second harmonic generation with critical coupling

The waveguide side-coupled to a racetrack resonator was simulated using a nonlinear two-dimensional finite-difference time-domain (2D FDTD) algorithm. Although another technique could have been used, such as finite-element method, FDTD was used because of its versatility, the ability to monitor the field profiles in time as they propagate, and the ease of modeling the nonlinear materials of interest. The details of the implementation of this FDTD nonlinear simulation tool can be found in Ref. [42]. The FDTD algorithm enables the analysis of SHG by assuming a nonlinear constitutive relationship of the second-order nonlinear material that takes the form of Eq. (2.10), which is appropriate for crystal classes $\bar{4}3m$, 23, and $m3m$ (e.g., GaAs or Si) [1], and the interaction is assumed to be instantaneous.

The device shown in Figure 5.3 was simulated using this code, where the excitation at the fundamental frequency enters the straight waveguide from the left near the left boundary. In these simulations, the high-permittivity material is assumed to have

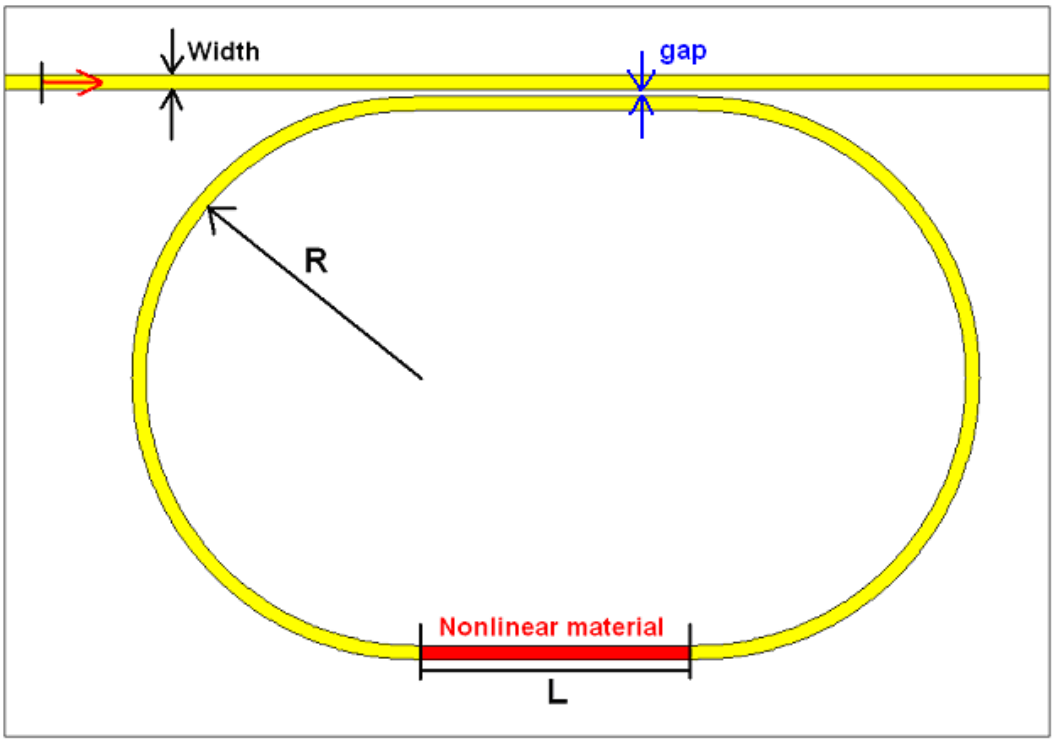

Figure 5.3. Schematic of the simulated device, composed of a slab waveguide side-coupled to a racetrack resonator that includes a $\chi^{(2)}$ nonlinear region. The input source is indicated by a red arrow.

a permittivity of 7.29, the low-permittivity material was assumed to be air (ε_r = 1.0), perfectly-matched layer (PML) absorbing conditions [115] were used on all boundaries to truncate the computational domain, and an input pulse with a Gaussian spectrum centered at the fundamental frequency was used for the excitation. The waveguide is assumed to be composed of a linear and nondispersive dielectric (although waveguide dispersion is still present, of course) with a width of 10 grid cells (about one-third of the fundamental wavelength), the radius R of the two curved ends of the racetrack resonator is 240 grid cells measured at the center of the waveguide, and the length L of the straight regions of the racetrack resonator is 240 grid cells. The waveguide and straight portion of the racetrack resonator are separated by 6 grid cells. The linear frequency response of this

coupled waveguide-resonator system was calculated using the FDTD technique with a Gaussian excitation pulse, as shown in Figure 5.4, where frequencies around the

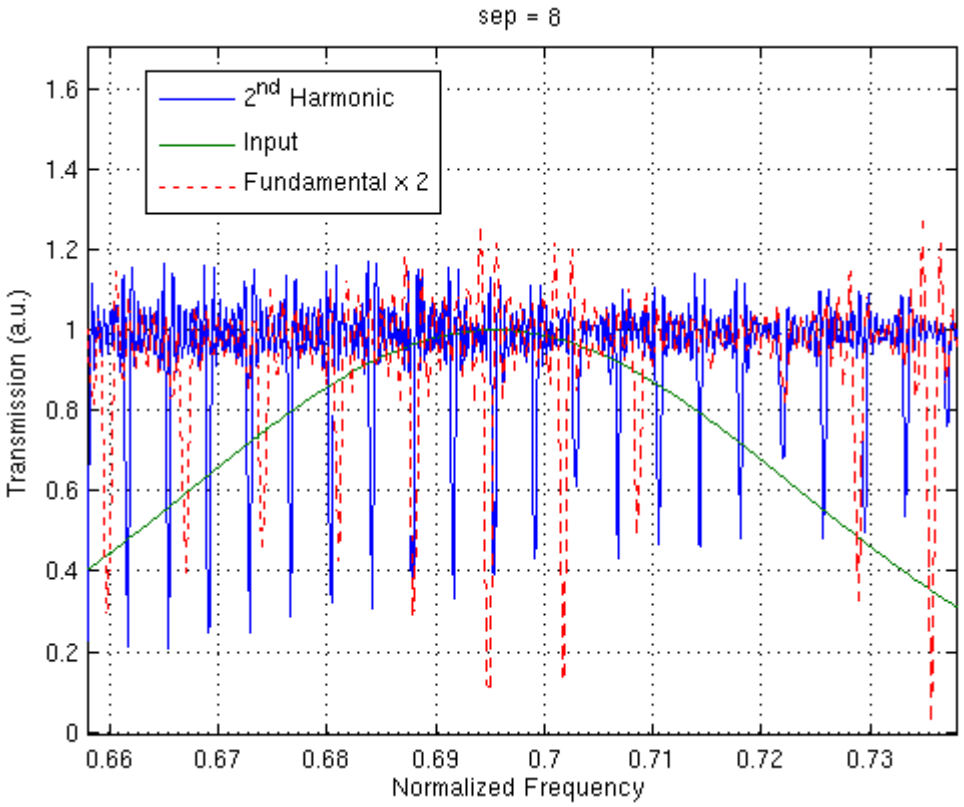

Figure 5.4. The frequency response of the waveguide coupled to a racetrack resonator. The frequencies at the fundamental have been doubled for direct comparison with the frequencies at the second harmonic.

fundamental have been multiplied by 2 for direct comparison with the frequencies around the second-harmonic. The racetrack resonator parameters have been chosen to provide a bend radius that does not suffer significantly from bending losses, a waveguide-resonator gap that offers strong coupling, and straight sections that provide an extended nonlinear region for good single-pass SHG and also resonant modes for the operating frequencies of interest. From this plot, it is clear that a resonant mode can be obtained for both the fundamental and second harmonic frequencies using the same resonator parameters, which is essential for optimal operation of the structure. However, it is not possible to

optimize the coupling for the fundamental and second harmonic simultaneously, since the maximum resonator quality factor (Q) for a given resonator size is directly related to the frequency of the resonant mode (the effects of fabrication imperfections on the Q are not considered). Thus, the resonator was optimized for critical coupling with maximum Q at the fundamental frequency; this represents a limiting factor for the overall extraction of the SHG signal out of the resonator and back to the output waveguide that prevents 100% conversion efficiency in an actual device.

It can be deduced from the constitutive relationship given in Eq. (2.10) that a transverse-electric (TE, i.e. E_z component only) excitation will result in no SHG, while a transverse magnetic (TM, i.e. E_x and E_y components present) input will result in a TE-polarized SHG signal. The field profiles of the fundamental and resulting second harmonic fields calculated using the nonlinear FDTD code are shown in Figure 5.5, where a nonlinear $\chi^{(2)}$ material using the above form has been placed in the lower straight portion of the resonator. In this case, a single-frequency (i.e. continuous wave or CW)

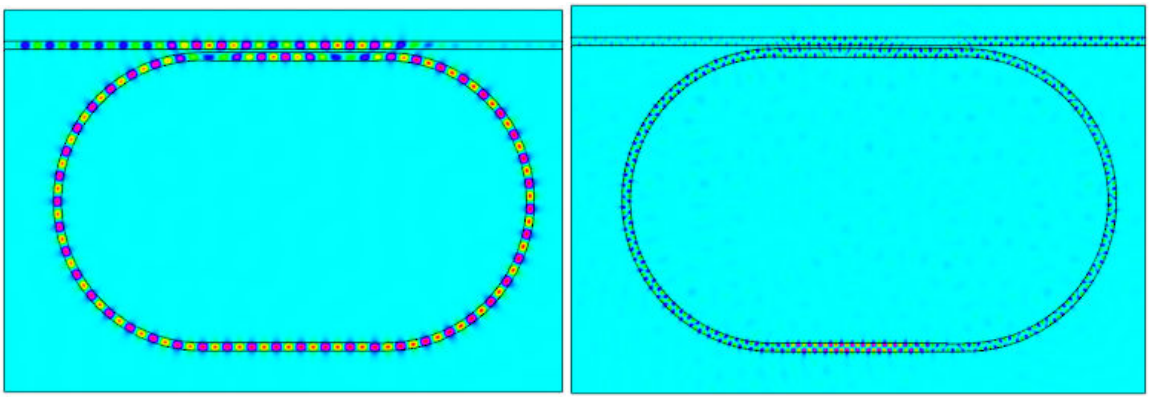

Figure 5.5. a. TM (B_z field component) mode profile of the waveguide coupled to a racetrack resonator showing the fundamental frequency field. **b.** TE (E_z field component) mode profile of the waveguide coupled to a racetrack resonator showing the second harmonic field. The waveguide width is 10 grid cells, the radius of the two curved ends of the racetrack resonator is 240 grid cells measured at the center of the waveguide, and the length of the straight regions of the racetrack resonator is 240 grid cells.

source was used, seen entering the waveguide from the left of the resonator, and the frequency was chosen such that critical coupling is satisfied for the fundamental beam, corresponding to a high-Q (but not critically-coupled) mode at the second harmonic frequency. The field values in Figure 5.5b have been normalized to the maximum, which occurs as expected in the nonlinear region of the resonator. Thus, the SHG power coupled back to the waveguide is significant, despite the fact that it appears smaller than the power in the resonator. Also, some radiation can be observed inside and around the racetrack resonator, due to narrow waveguide width that has a cutoff frequency near that of the second harmonic wave and a slight mode mismatch at the abrupt junction between the straight sections of the racetrack resonator and the curved sections.

Two notes should be made here. First, as seen in Figure 5.5b, the SHG mode has an odd profile, despite the fact that an even mode was used for excitation (Figure 5.5a). This can be explained by the constitutive relationship (Eq. (2.10)), which shows that the second harmonic field results from a multiplication of the E_x and E_y components of the

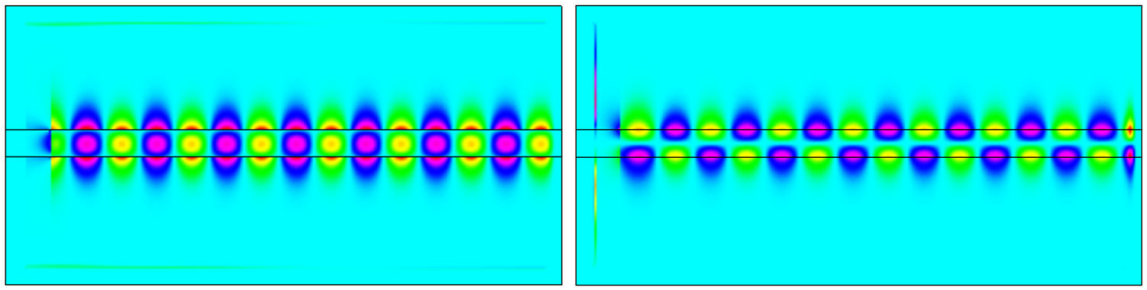

a. **b.**

Figure 5.6. Field profiles for the **a.** E_x and **b.** E_y components of the fundamental even TM mode for a slab waveguide. The field values in these plots have been normalized to the maximum; the E_y field is much smaller then the E_x field.

fundamental field (Figure 5.6a and b, respectively). As seen in Figure 5.6b, the E_y field component has a null on the center longitudinal axis of the waveguide, which gives rise

to an odd mode profile for the second harmonic field. Second, since the slab waveguide that defines the racetrack resonator has some (nonzero) dispersion, the fundamental and second harmonic beams will have differing propagation constants. This resulting phase mismatch will limit the maximum SHG possible in a given length on nonlinear material, since the second harmonic field will begin to convert back to the fundamental periodically once the two beams drift 180° out of phase. Thus, the SHG signal will oscillate sinusoidally between 0 and some maximum, as shown in Figure 5.7a. To counteract this effect, quasi-phase matching (QPM) [116] has been employed in the simulations presented in this work. QPM is implemented by changing the sign (i.e.

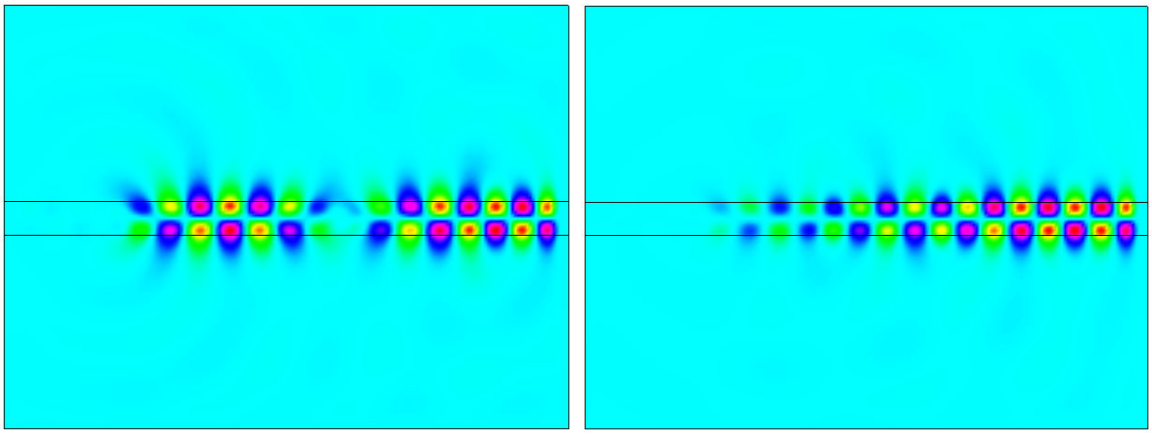

a. **b.**

Figure 5.7. a. SHG field for a slab waveguide without quasi-phase matching. **b.** SHG field for a slab waveguide with quasi-phase matching. The field values are normalized to the maximum, and the length of the waveguides is about twice the coherence length of the SHG is this structure as evidenced by the two periods of oscillation of the field in **a.**

reversing the orientation) of the $\chi^{(2)}$ material every half-period of the phase drift between the fundamental and second harmonic beams, given by

$$\Lambda = \frac{\pi}{\Delta k} \tag{5.17}$$

Using QPM, the SHG can be made to increase monotonically, as shown in Figure 5.7b.

The waveguide-resonator structure was simulated using a continuous-wave (single-frequency) input source as the excitation and a runtime of 2^{19} time steps to achieve steady-state conditions. This simulation time is several orders of magnitude larger than the coherence length for the second harmonic process, demonstrating the effectiveness of the QPM modulation. The spectrum at the second harmonic frequency is shown in Figure 5.8a, where the input spectrum multiplied by 2 is included for reference. As predicted by the Eq. (5.15), a small blue shift in the SHG frequency of about 0.04% has occurred due to $\alpha_{2,\omega}$ being complex. By combining the aforementioned optimization of the coupling between the waveguide and the resonator for the fundamental frequency, choosing a geometry that has a resonant mode at the second harmonic, and using QPM in the nonlinear region, the SHG beam can be efficiently coupled out of the device, as seen in Figure 5.8b. The power of the SHG signal at the output of the waveguide is calculated

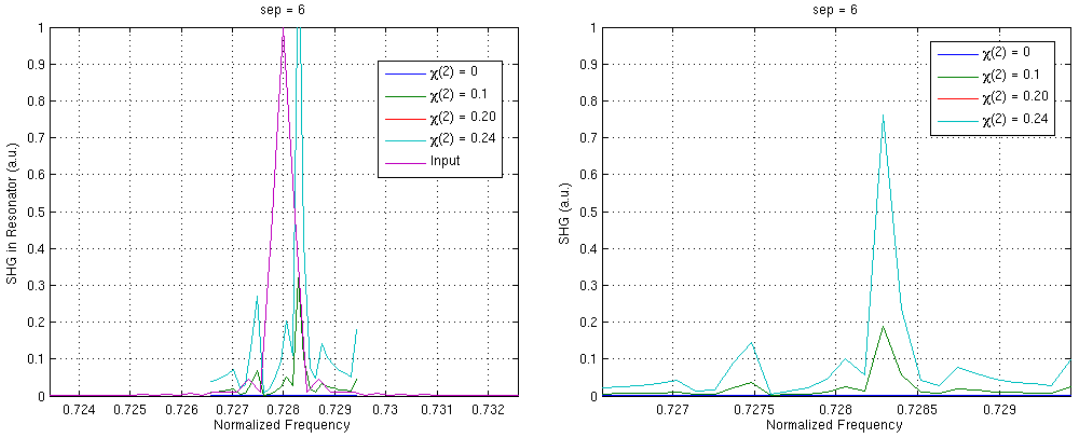

a. **b.**

Figure 5.8. SHG efficiency **a.** inside the racetrack resonator and **b.** coupled to the output waveguide.

to be about 75% of the input power at the fundament frequency entering the waveguide, at a normalized $\chi^{(2)}$ value of 0.24 (see Section 2.2). This corresponds to a value well

below the damage threshold of most semiconductors and nonlinear polymers, for strongly nonlinear materials such as GaAs ($d_{36} = 4 \cdot 10^{-7}$ cm/statvolt).

CHAPTER 6

MEASUREMENT OF PLANAR PHOTONIC DEVICES

6.1 Phase-Sensitive Lock-In Characterization Tool

The ability to accurately measure the operating behavior of nanophotonic devices is essential to photonics research. Although, there are some recently reported techniques for measuring the dispersion of PC waveguide (PCWG) samples [117], many existing techniques are very complicated, requiring expensive equipment such as an ultrafast laser or near-field scanning optical microscope. In this chapter, the experimental characterization of triangular-lattice PCWGs in using a phase-sensitive technique is described, including the observation of large parity-change-induced dispersion. Using a lock-in amplifier, the signal-to-noise ratio (SNR) of the power transmission measurements can be improved by at least one order of magnitude, while at the same time direct correlations can be made between features in the group delay spectra obtained from phase measurements and the complex transmission properties, i.e. amplitude and phase of the PCWGs. Also, with this technique it is possible to make measurements very close to the mode gap of a PCWG [118], at frequencies where broad-band techniques such as those that use ultra-fast lasers fail.

A schematic of the experimental setup is shown in Figure 6.1. The infrared (IR) lasers (a multiplexed series of four lasers from Agilent Technologies Inc., tunable from 1260 nm to 1640 nm a with 100 kHz linewidth) are triggered by a common square-wave modulation signal at frequency f_M = 20 kHz, while the average output power is kept constant at 0.5 mW. A lock-in amplifier (SR 830 from Stanford Research Systems,

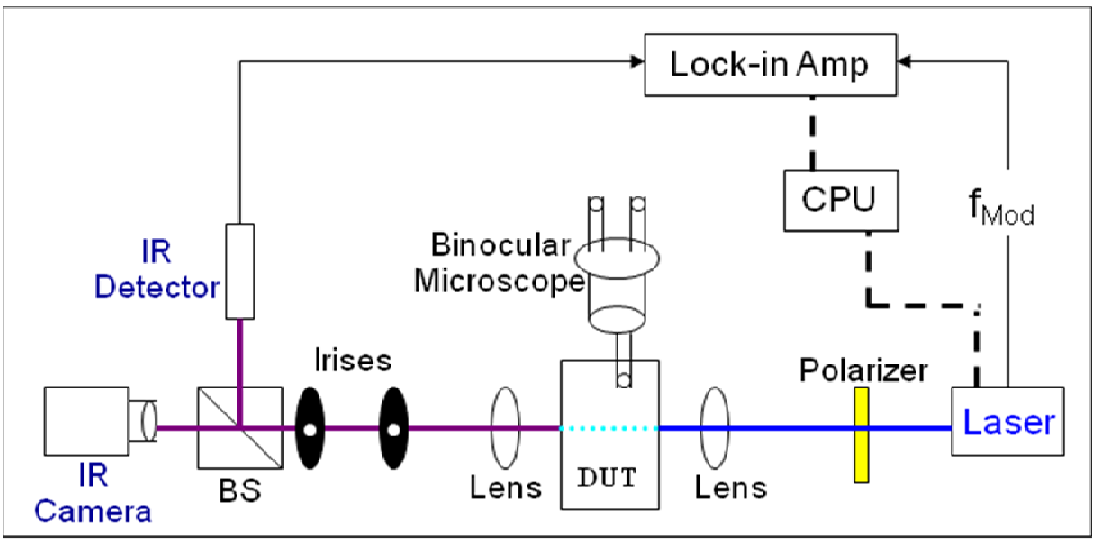

Figure 6.1. Schematic of experimental lock-in setup for making phase-sensitive measurements of planar PC devices.

1 to 102 kHz) is also synchronized to the same trigger signal to allow for phase measurements with a resolution of better than 1° (0.017 rad). The laser beam is TM polarized (i.e. magnetic field normal to the plane of the periodicity of the PCs) by the sheet polarizer and coupled into the input slab waveguide (WG) using a 40X microscope objective lens. The light from the output slab WG is imaged onto an IR camera by a 20X objective lens, and the unwanted scattered light is filtered by one or more adjustable irises. Using a thin-film 50/50 broadband (500 nm to 1.8 μm) beam splitter, one-half of the output beam power is steered to a camera to enable viewing of the far-field output mode profile, and the other half into an IR photodetector (New Focus Corp., Model No. 2033, bandwidth 0 to 30 kHz), which was connected to the input of the lock-in amplifier. The output field for a frequency that has good transmission is shown in Figure 6.2a, and Figure 6.2b shows the same structure but for a frequency with poor transmission. The lock-in amplifier was used to measure the power, *R*, of the output signal component

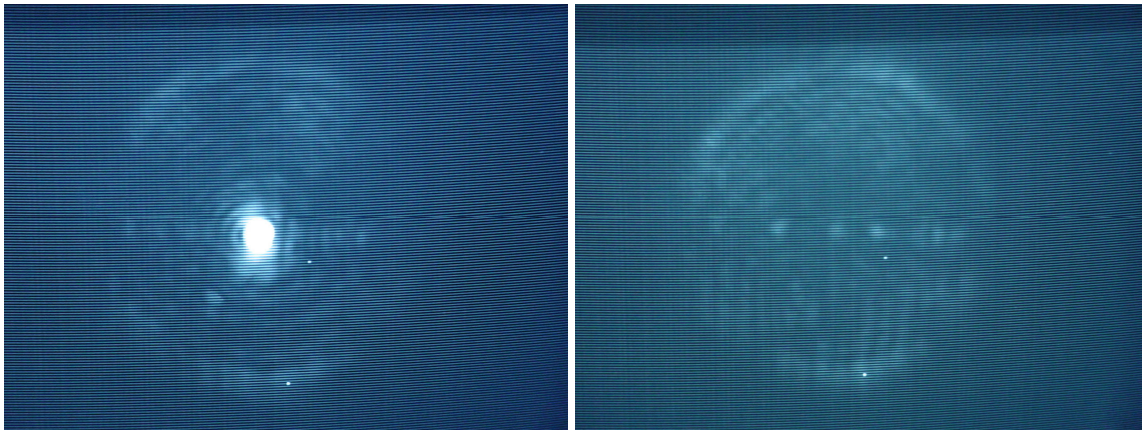

a. **b.**

Figure 6.2. Sample output mode imaged using an IR camera for **a.** a frequency in the high-transmission band, and **b.** a frequency in the transmission mode gap of the PCWG.

having the same frequency as the reference signal from the input channel, and also to compare the phase shift, Φ, between the output signal and the reference signal. This phase shift is a direct measure of the optical signal delay, τ, with $\Phi = 2\pi f_M \tau$. The input laser wavelength was controlled by computer, which iteratively recorded R and Φ for each selected wavelength.

To clarify what is actually measured when referring to the phase (or delay) signal, a diagram of the signals used in the setup are shown in Figure 6.3, where the red curve represents the reference signal and the blue curve represents the filtered output signal. The reference is a "on-off" modulation of the CW beam generated by the tunable laser, and thus is represented by a square-wave signal. The output signal coming from the detector will generally be distorted due to various scattering and reflections in the measurement setup, but is filtered by the lock-in amplifier to remove any frequency components that are not a harmonic of the reference frequency. Thus, the phase difference between reference signal and the filtered signal from the light propagating through the sample is what is actually measured by the lock-in amplifier. This phase

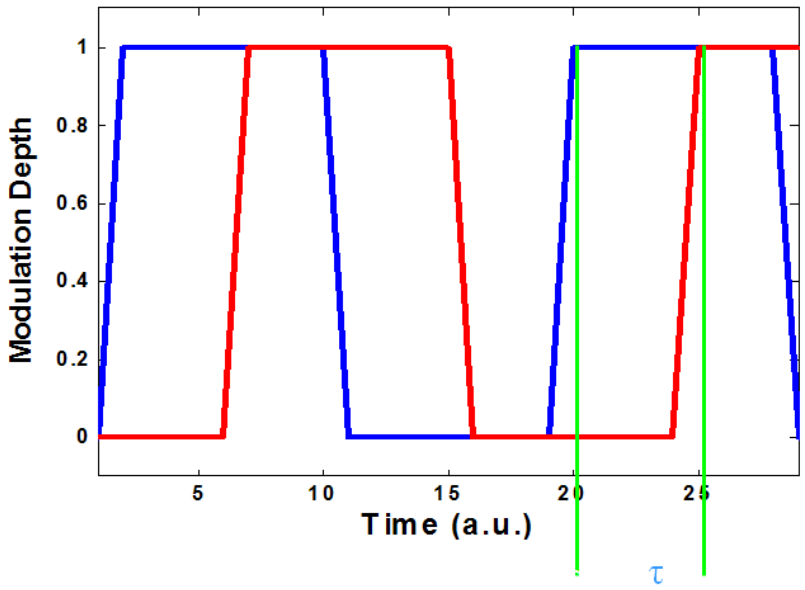

Figure 6.3. Schematic plot of the reference and measured signals used by the lock-in amplifier to determine the phase/delay signal measurements.

delay is "zeroed" at a reference wavelength, and then the shift in that signal is monitored as the wavelength is swept.

The PCWG samples were fabricated on a silicon-on-insulator wafer (Unibond wafer, from SOITEC Inc.). This wafer has a silicon slab of 260 nm thickness, which is separated from the silicon substrate by a 1 μm SiO_2 buried oxide layer. The thickness of the slab was chosen to ensure single-mode guiding along the normal direction of the wafer at wavelengths centered around 1.5 μm. The PCWGs were sandwiched between two slab waveguides to couple light in and out the PCWGs. The sample was fabricated using electron beam lithography (e-beam lithography or EBL) to define the regions of the silicon layer to be removed, and reactive-ion etching (RIE) to remove the material [11]. The scanning electron microscopy (SEM) image of a typical sample, which features a 400-period triangular lattice of air holes, is shown in Figure 6.4. The lattice constant a for this sample was 380 nm, and the hole radius r was determined to be $0.29a$. Samples

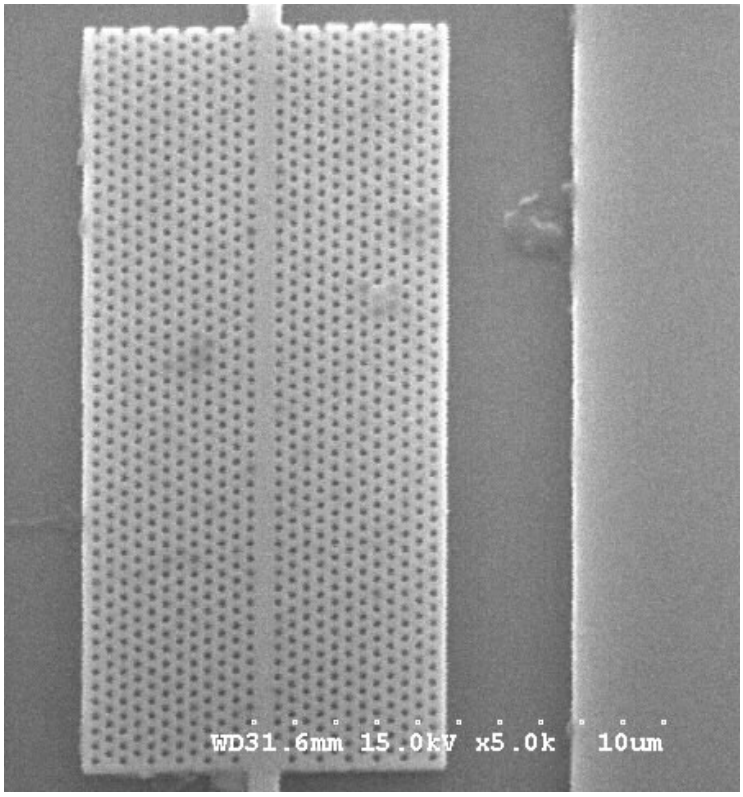

Figure 6.4. Scanning electron micrograph of the PCWG sample measured using the phase-sensitive measurement test bench; the planar sample was fabricated on a silicon-on-insulator wafer with a period of 380 nm and hole radius of 29% of the periodicity.

of the structure with same lattice constant but different lengths (L) of 50a, 100a, and 150a were used to provide more insight into the properties of the PCWGs.

6.2 Phase-sensitive measurements

As a point of reference, the dispersion diagram and field profiles of the guided TM modes of the PCWG created by removing a single row of air holes in the PC lattice (commonly referred to as a W1 waveguide) were calculated using the 2D FDTD technique. The simulations assumed an infinite thickness of the SiO_2 layer below the PCWG structures. The dispersion diagram is shown in Figure 6.5, where blue stars

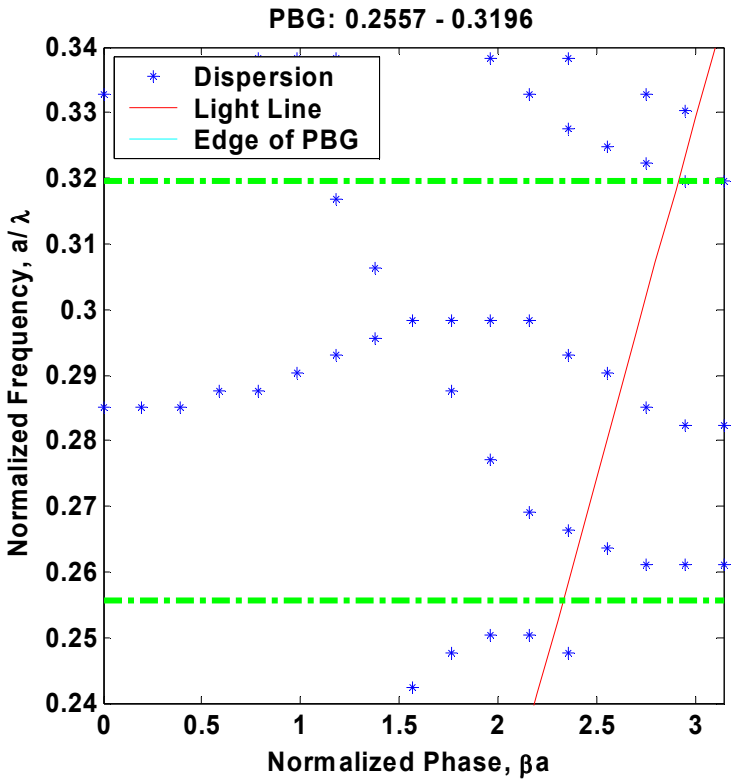

Figure 6.5. Dispersion diagram of a W1 triangular-lattice PCWG calculated using a 2D FDTD code. The bandgap is highlighted in green, the light line in red, and the guided modes by blue stars.

represent the odd, even, and weakly guided modes in this PCWG. In the same figure, the light line of this PCWG is plotted as the solid red line, and the edge of the PBG is shown by the horizontal green dotted lines. The simulation results indicate that there exists a frequency range inside the photonic band gap (PBG) with no guided modes within the normalized frequency range $0.25 < a/\lambda < 0.26$, with λ being the light wavelength in a vacuum. Such a frequency range is commonly referred to as a photonic mode gap (PMG). At the same time, the light line crosses the even modes at the normalized frequency $a/\lambda = 0.265$, above which the guided modes of this PCWG are no longer well-confined in the out-of-plane direction. The even and odd field profiles (i.e. intensity distribution) for the guided modes are shown in Figures 6.6a and 6.6b, respectively. It

can be seen from Figure 6.6 that the power of the even mode is centered in the middle of the PCWG, while the odd mode has essentially no intensity in that region.

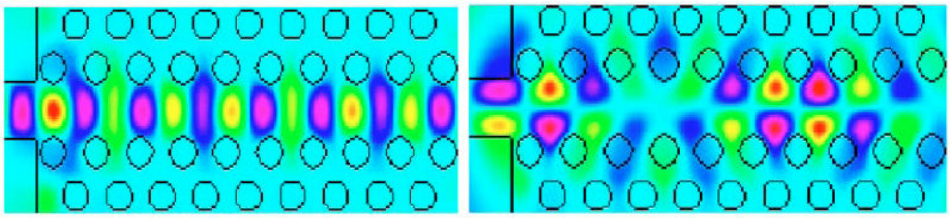

a. **b.**

Figure 6.6. Field profile of the **a.** even and **b.** odd guided modes of a W1 triangular lattice PCWG calculated using FDTD.

To study the transmission properties of the W1 PCWGs, all of the measurements were normalized to the transmission spectra of the reference waveguides, simple slab waveguides with the same width and total length as the PCWGs and fabricated on the same substrate. Figure 6.7a shows the transmission spectrum of a PCWG with $L = 50a$, from which a PMG can be clearly seen in the normalized frequency range of $0.24 < a/\lambda < 0.25$. The signal group delay spectrum, $\tau(\lambda)$, was directly deduced from the phase signal, which was measured simultaneously with the transmitted power using the lock-in amplifier. The results are plotted in Figure 6.7b, where a group delay dip is clearly seen in frequency range of $0.24 < a/\lambda < 0.25$ with a peak value of -0.86 μs, which corresponds to a phase shift of -0.11 rad (well above the system resolution of 0.017 rad). The frequency range of this group delay dip matches well with the PMG frequency range in the transmission spectrum in Figure 6.7a, which suggests the same physical origin, i.e. the PMG, for these two features. This feature is similar to those observed in one-dimensional PC studies, where the PBG generates a group delay difference for various wavelengths [119].

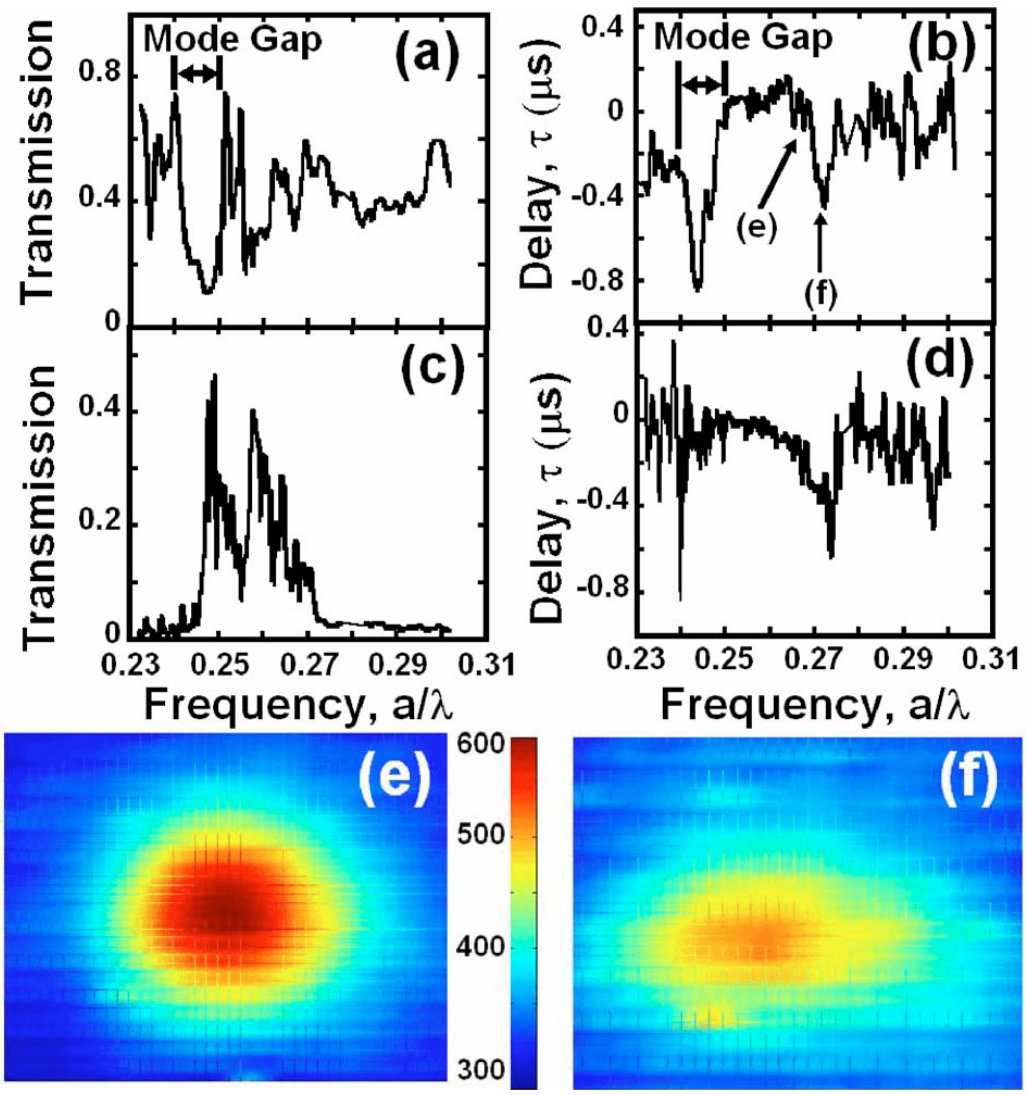

Figure. 6.7. a. Transmission and **b.** signal group delay spectra of a 50-period triangular lattice PCWG. **c.** Transmission and **d.** group delay spectra of a 150-period triangular lattice PCWG. Imaged output field profiles at frequencies **e.** $a/\lambda = 0.265$ and **f.** $a/\lambda = 0.27$, as highlighted in **b.**

Aside from the above observations, another group delay dip can be seen in frequency range of $0.265 < a/\lambda < 0.274$ with a peak value of −0.48 μs (Figure 6.7b). There are no obvious features in the transmission spectrum (Figure 6.7a), such as a low transmission region, corresponding to this dip. In order to confirm the generality of these observations, the transmission and signal delay spectra of another PCW was measured having the same lattice constant, but with $L = 150a$. The results are shown in Figures

6.7c and 6.7d. It is worth noting that compared with Figures 6.7a and 6.7b, the onset of the PMG in Figures 6.7c and 6.7d is redshifted to $a/\lambda = 0.245$ (for $L = 150a$), as opposed to $a/\lambda = 0.25$ (for $L = 50a$) for both the transmission and phase spectra. This small shift (about 2%) is likely the result of fabrication imperfections. However, the PCWG that is three times longer also has a very different transmission spectrum from the shorter waveguide. A dramatic transmission dip for frequencies below $a/\lambda = 0.245$ and above $a/\lambda = 0.265$ is observed for the longer structure. Interestingly, however, the group delay spectrum in Figure 6.7d is very similar to that in Figure 6.7b, in that there is one dip peaking around $a/\lambda = 0.24$ corresponding to the PMG, and another one peaked at $a/\lambda = 0.272$. Thus, the group delay spectra obtained by the lock-in technique are not affected by tunneling effects in the short waveguide and are less sensitive to length-induced loss. These experimental results demonstrated the power of the lock-in technique for the characterization of PC structures.

Another significant observation is that the onset of high transmission (corresponding to the onset of the even mode) is at $a/\lambda = 0.25$ in the experimental observations (Figures 6.7a and 6.7b) as opposed to that at $a/\lambda = 0.26$ for the simulation results (Figure 6.5). This small difference (about 4%) between the numerical and experimental results likely comes from the assumption of an infinite thickness of the SiO_2 layer below the PC structures and other physical defects in the fabricated structure that were not accounted for in the simulations. Nevertheless, the numerical results still provide qualitative insight if the simulated dispersion curves are shifted (Figure 6.5) down by $a/\lambda = 0.01$. In the simulation results, the light line crosses the even mode at $a/\lambda = 0.265$, which corresponds to the small transmission dips in the experimental

measurements at about $a/\lambda = 0.255$ (Figures 6.7a and 6.7c). There are no guided modes (even or odd) below the light line between $a/\lambda = 0.265$ and $a/\lambda = 0.28$. Above $a/\lambda = 0.28$, some of the odd mode extends below the light line. In this sense, there is a parity change in the guided modes of the PCWG. This mode parity change is attributed to the observed anomalous phase dip, which peaks around $a/\lambda = 0.27$ as shown in Figures 6.7b and 6.7d.

In order to confirm this observation, the far-field patterns (Figures 6.7e and 6.7f) corresponding to $a/\lambda = 0.265$ and $a/\lambda = 0.27$ (marked as (e) and (f) in Figure 6.7b, respectively) were measured. It is clear in these images that the far-field profile changes from a centered, round mode to a more spread-out, elliptical mode. The measured signal power level at $a/\lambda = 0.27$ is roughly the same as that at $a/\lambda = 0.265$ (Figure 6.7a), but the signal is delayed by about 400 ns compared to that at $a/\lambda = 0.265$ (Figure 6.7b). A recent work using scanning near-field optical microscopy confirms the claim of Bloch mode parity changes in these types of PCWGs [122]. Another interesting observation is that the odd modes in these PCWGs exhibit much higher propagation losses as compared to the even modes. As shown in Figures 6.7a and 6.7c, the transmission peak around normalized frequency $a/\lambda = 0.25$ (attributed to the even mode) is reduced by less than 3 dB as the PCWG length increases from $50a$ to $150a$. For the same length increase, the transmission around $a/\lambda = 0.27$ (attributed to the odd mode) is reduced by almost 10 dB, supporting the claim of mode parity changes in this frequency range. The high loss of the odd modes might be due to the fact that the odd modes have more of their power concentrated on the edges of the guiding region of the PCWGs than odd modes, as shown in Figure 6.6, and thus are more sensitive to fabrication defects in the holes that define

the PCWG. It is well understood that relatively slow group velocities, such as that measured around $a/\lambda = 0.27$, can enhance propagation loss as well [123].

Note that there is a key difference between this method and those using an autocorrelator [120] or a near-field scanning optical microscope (NSOM) [121]. The modulation frequency and the final bandwidth of the signal used in the measurements (approximately $0.8 \cdot 10^{-6}$ nm) are several orders of magnitude smaller than the bandwidth of a femtosecond pulse (on the order of 20 nm) used in those experiments, which allows for measurements much closer to the edge of the PMGs, where smaller group velocities tend to distort wideband pulses. Significantly distorted pulse shapes were also observed at the low group velocity frequencies using this system. However, the ratio of delay over pulse duration was only 0.034, even at the peak of the delay signal. This has an important impact on the use of PC devices for high-bandwidth applications, since the data rate will be limited by distortion of the pulses propagating in such devices. One way to quantify this effect is by the dispersion of the waveguide, which can be calculated from the derivative of the delay signal, as shown in Figure 6.8. It can be observed that the dispersion (green curve) increases in amplitude (black curve fit) at frequencies approaching the PMG of the PCWG. This indicates that a high-data rate signal, which inherently has a relatively wide bandwidth, will experience significant distortion in this PCWG except for frequencies far from the PMG. This factor, combined with the high-loss region at higher frequencies, greatly limits the usable bandwidth of a standard PCWG; design modifications that can extend the low-loss, linear-dispersion bandwidth of such waveguides may prove invaluable for high-speed data channels [11].

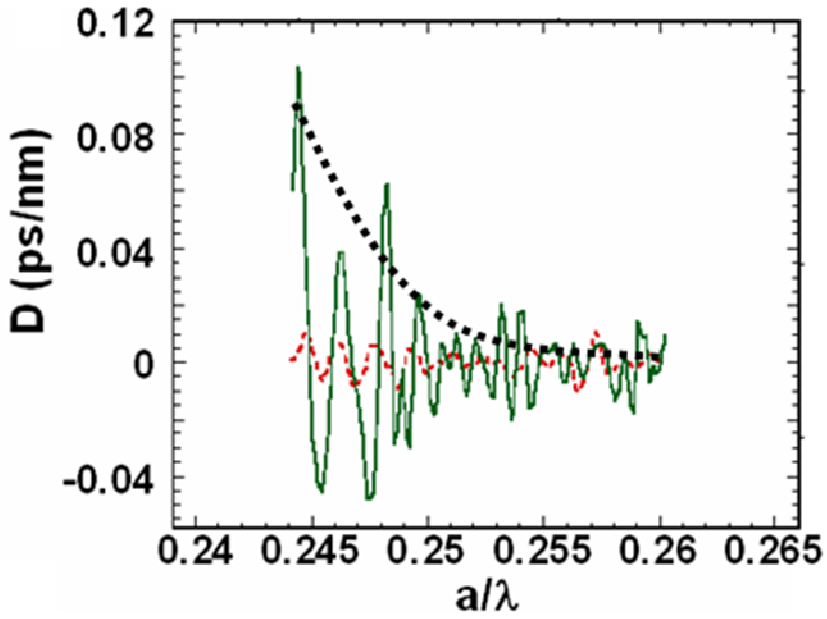

Figure 6.8. Calculated dispersion from the phase measurements for the W1 triangular-lattice PCWG for frequencies near the edge of the bandgap; the phase measurement is shown in red for reference, as well as an exponential fit to the envelope of the signal shown in black.

An interesting calculation that can be made from the experimental delay data and by taking into account the total length (19 μm) of the 50-period PCWG indicates that the optical signal travels at a speed of ~22 m/s. Since this rivals the lowest slow-light values measured in a Bose-Einstein condensate [124], it is clearly not accurate for a solid-state system such as this. The inaccuracy arises from the relatively low modulation frequency used for the lock-in amplifier, which is too slow to track the actual phase change and thus produces false delay value. This does not affect the observations already made, since they were based on the qualitative phase behavior versus frequency and the accuracy of the frequency data is based on the very precise tuning of the lasers. However, is does indicate that calculations based on the actual phase shift values should be considered cautiously. Thus, the dependence of the measured phase signal on the modulation frequency was investigated. A high-frequency lock-in amplifier (SR 844 from Stanford

Research Systems, 25kHz - 200MHz) was used for this characterization, and a lithium niobate Mach-Zehnder interferometer modulator had to be added to the test bench to provide the higher-frequency modulation of the continuous-wave output of the tunable lasers. The result of this characterization is show in Figure 6.9, where the measured delay spectra for frequencies near the mode gap of the PCWG are plotted for lock-in modulation frequencies ranging from 5 to 100 MHz. There is significant variation among the curves, due in part to phase shifts cause by a change in the reference phase values used to make the measurements; however, the primary effect of increasing the modulation frequency is that the amplitude of the measured delay values decreases significantly. This verifies that if the amplitude of the delay signal is to be used

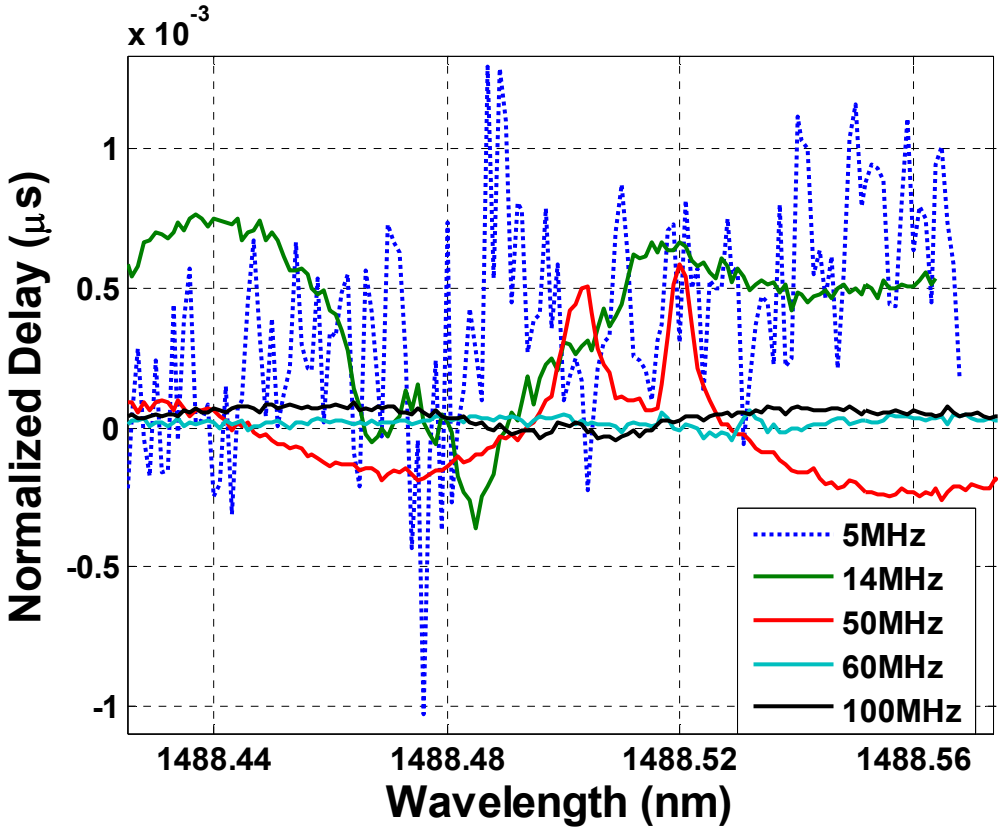

Figure 6.9. Plot of the measured delay signal for frequencies near the mode gap of the PCWG for lock-in modulation frequencies ranging from 5 to 100 MHz.

quantitatively, the modulation frequency used for the lock-in amplifier become critical, and must be chosen to ensure that sufficient bandwidth is available to accurately resolve the delay behavior of the device being tested.

A more complicated structure was also measured to demonstrate the utility of the phase sensitive test bench, namely the multi-functional 4-port device discussed in Section 4.3; an SEM of the device was shown in Figure 4.8. The transmission behavior of ports 2 through 4 has already been discussed in Chapter 4. Here, the focus is on the propagation characteristics for port 2 only. The transmission and delay (phase) measurements are shown in Figure 6.10, where the complex behavior predicted by 2D FDTD simulations (see Figure 4.5) is seen. The two peaks in the transmission measurement at about a/λ = 0.30 and 0.31 appear to correspond with the peaks in the simulated transmission at about

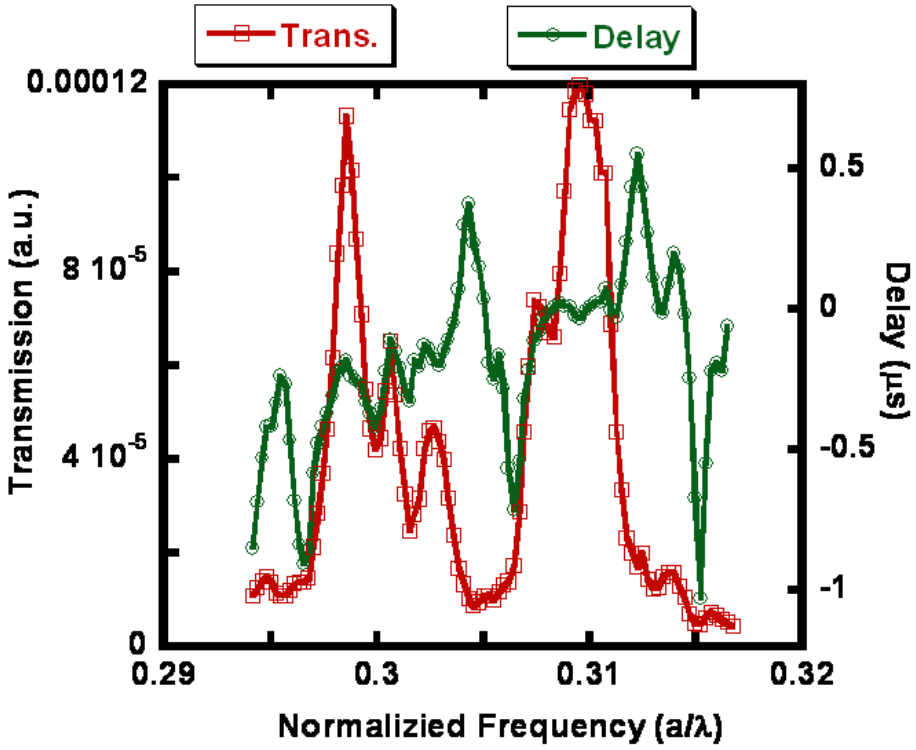

Figure 6.10. Measured transmission and delay curves for port 2 of the multifunctional PC structure shown in Figure 4.8.

a/λ = 0.27 and 0.28. The shift in frequency is likely due to errors in the permittivity values used in the simulations that do not accurately model the actual permittivity of the silicon layer and effective permittivity due to the finite thickness of the physical sample. Nevertheless, it is interesting to note that the measured delay signal is relatively flat in the transmission bands corresponding to the measured amplitude peaks, and oscillates strongly at both edges of these transmission bands. Thus, the delay curve could be used to identify the onset of the transmission bands independent of the amplitude (transmission) data, even for a structure that has very complex propagation characteristics. This confirms the utility of the additional information provided by this phase-sensitive test bench.

CHAPTER 7

CONCLUSIONS AND FUTURE DIRECTIONS

7.1. Conclusions

A finite-difference time-domain (FDTD) simulation tool has been developed that is capable of simulating linear, anisotropic, $\chi^{(2)}$, and $\chi^{(3)}$ nonlinear materials. This includes the vast majority of the optical properties used for practical applications in integrated photonics. A full set of sources, including active waveguide mode sources, have been developed for both 2D and 3D domains. Field values can be recorded for points or integrated over a line (2D) or surface (3D), and a running Fast-Fourier Transform (FFT) is included for frequency-domain calculations. The algorithm has been shown to be stable based on Courant's stability condition, and has been verified using the well-understood phenomena of second-harmonic generation in a waveguide and self-phase modulation in a bulk nonlinear medium. The code has also been parallelized, demonstrating near-ideal performance for smaller computational domains and monotonically increasing speed-up factors even for the largest domains. The floating-point operations per second (FLOPS) performance of the 3D FDTD code has been characterized, indicating that the code is well optimized. *To the best of my knowledge, this is the most comprehensive and efficient numerical finite-difference time-domain simulation tool for nanophotonic systems developed to date. The performance of the code is similar to or better than that of the available commercial codes, while offering the ability to simulate a competitive range of material properties and optical effects.*

The theory for a Green's function-based loss analysis tool for photonic crystal waveguides (PCWGs) was presented, including the application of the layer-KKR technique using a supercell structure. The technique was demonstrated using the plane-wave expansion method to calculate the complex band behavior of a simple 2D PCWG having a single defect. It was observed that the main features of the transmission spectrum of the PCWG agreed with the brute force calculations, with significant differences arising from the mode-based nature of the technique, as opposed to the FDTD simulations that include all possible modes in the structure. The power of the technique was demonstrated by calculating the transmission spectra for two distinct modes of the structure, a feat that cannot be easily accomplished using a time-domain technique such as FDTD. The ability of the technique to be extended to analyze a random distribution of defects using the coherent potential approximation was also presented. *I believe that this technique combined with statistical analysis will be the most comprehensive tool for analyzing important issues like loss and scattering in a wide range of optical structures, especially those exhibiting anomalous dispersion characteristics.*

All-optical modification of the transmission characteristics of a two-cavity PC drop filter using nonlinear material in the holes of the PC was demonstrated theoretically using the nonlinear FDTD code developed in Chapter 2. A multifunctional bent PCWG design was also presented that can provide various power-splitting ratios among the four ports of the device based on the geometrical properties of a few cavity holes. The theoretically all-optical modification of the behavior of the device using nonlinear materials was presented as well. The design was fabricated and characterized using the test bench described in Chapter 6 to verify that the linear power-splitting functionalities

can be achieved in an actual device. *I believe that this universal structure can be used for a variety of applications, and even as a simple reconfigurable photonic structure.*

A critically-coupled resonator structure for highly-efficient chip-scale second harmonic generation was described and optimized for maximum conversion efficiency. The coupled mode theory governing the device operation has been presented, which shows that 100% conversion efficiency would be possible if critical coupling could be achieved simultaneously at both the fundamental and second harmonic frequencies. However, this is not possible in a real device of this design, since the waveguide dispersion needs to be taken into account. In this case, the coupling Q is optimized for the fundamental frequency, and QPM is used to compensate for the phase mismatch between the fundamental and second harmonic beams. The device was simulated using a nonlinear 2D FDTD code, and it was demonstrated that up to 75% of the second harmonic power at a normalized $\chi^{(2)}$ value of 0.24 could be coupled out of the device for a properly designed structure. This is comparable to what is currently achieved in free-space optics with bulk nonlinear optical crystals, where 66% multi-pass conversion efficiency has been demonstrated [105]. *I believe that the technique proposed here can enable ultra-compact, highly efficient nonlinear optical devices on-chip, which will be very useful for greatly desirable photonic integrated circuits used in applications like signal processing and communications.*

Finally, a phase-sensitive lock-in test bench was described and used to measure the transmission properties of a simple PCWG. In addition to the improved signal-to-noise ratio for the measured transmission spectra, large group delay dips at two specific frequencies were observed in the phase data, which could be attributed to the photonic

mode gap and modal parity changes between the even and the odd modes in the PCWG. The experimental results demonstrate the power of the lock-in technique for the characterization of planar PC structures. The response of the phase signal provided by the system with increasing modulation frequency was investigated, highlighting the limitations of the amplitude of the phase data for devices the exhibit large optical delays. The test bench was also used to characterize the more complex multifunctional device described in Chapter 4, demonstrating that the phase signal could provide useful information even for a device that exhibits very complex transmission behavior. *This is the simplest characterization tool for the intensity and phase analysis of integrated photonics devices, as compared to all other alternatives reported to date, such as near-field scanning optical microscopy or spectral interferometry.*

7.2. Future directions

A few useful functionalities could be added to the FDTD code, depending on the electromagnetic system that is desired to be simulated. The capability to simulate general nonlinear materials, i.e. materials with constitutive relationships that include any combination of tensor elements, could be added without much additional complexity, although the iterative inversion method would have to be used since it is not possible to find an explicit expression like the one used for the $\chi^{(3)}$ code. Dispersive materials could also be added, which can have a resonant or time-varying response to optical waves, by modeling the behavior using the recursive convolution technique [46]. The 3D mode source could be extended as a Huygen's source (propagating in only one direction, rather than bi-directionally), by using appropriately specified electric and magnetic surface

currents and solving Maxwell's equations for the resulting source field components. This source would allow for accurate calculation of the reflected power in 3D waveguiding structures. Finally, the parallel implementation of the code could be further optimized to mitigate the saturation of the speed-up factor as the number of processors used increases. It is likely that the biggest factor limiting the performance of the current version of the parallel FDTD code is memory access issues when the simulation size becomes too large to fit into the processors' cache. This issue could be alleviated by implementing the update equations, the most-iterated portions of the code, using calls to the Linear Algebra PACKage (LAPACK) library. The LAPACK routines are written to automatically divide memory accesses for large arrays into cache-sized chunks and specifically optimized for most modern processor architectures.

The next step for Green's function-based complex mode technique, which is compatible with multiple scattering theory, would be to extend it to include the effects of multiple, randomly distributed defects using a configurational average with the coherent potential approximation, as mentioned near the end of Chapter 3. The dependence of scattering loss on the modes of various PC waveguiding structures could be investigated in greater detail, using the mode-based analysis properties of the technique. Also, the effects of coupling due to defect scattering between transverse electromagnetic modes, which are normally considered to be orthogonal, could be considered. This is something that has been observed in experimental data but is not commonly included in numerical electromagnetic simulations.

Experimental demonstration of nonlinear operation of the multifunctional PC device could be performed by introducing nonlinear material into the holes of the PC, as

was simulating using FDTD. Infiltration of nanoscale PC structures has been demonstrated for structures suitable for operation at communications wavelengths [125]. Additionally, the measurement test bench could be modified to allow for direct measurement of the reflection from the input port of the PC device, thus providing full characterization of its transfer properties. This would necessitate the addition of a circulator on the excitation side of the setup, preferably just before the device under testing.

A few schemes for fabricating the critically-coupled resonator for efficiency chip-scale SHG are possible. It theoretically possible to use the guiding high-index material as the nonlinear medium, if the material has a large enough intrinsic $\chi^{(2)}$ such as GaAs. In this case, an excitation at around 2 μm could be used to produce a SHG signal with a frequency within the transmission window for this semiconductor. For the active nonlinear region of the resonator, QPM could be achieved by using orientation-patterned GaAs [126], which used a novel growth method to periodically reverse its crystallographic orientation. However, one commonly-mentioned limitation of GaAs is that it is not compatible with modern CMOS fabrication techniques. For such applications, silicon is preferred for use as a guiding material because of the maturity of its fabrication technology and its compatibility with standard microelectronics fabrication processes, although cannot be used for SHG since its crystal is centrosymmetric. Nevertheless, advances in nonlinear polymer materials with relatively large $\chi^{(2)}$ values [127] make them very attractive candidates for an active material. Thus, the proposed device would use a waveguide and a racetrack resonator defined in silicon (for example, on a silicon-on-insulator or SOI wafer), with a layer of nonlinear polymer spun on top for

evanescent coupling to the guided light in the silicon region. This polymer layer could be patterned to remove the material everywhere except for the active region of the resonator, although it may not be necessary since the light intensity outside of the resonator will be too low to produce a significant second harmonic effect. Within the resonator, periodic poling of the polymer can be used to produce the desired modulation of the $\chi^{(2)}$ strength for QPM by patterning metal contacts above the polymer to provide the necessary electrical field profile [128]. Alternatively, a "1,0" type of QPM (rather than "1,-1") could be achieved by directly patterning the polymer to create a grating with a period corresponding to the QPM period using photolithography. Two issues arise when considering a top coating of polymer as the nonlinear material. First, the constitutive relationship of the material will likely be different from the one used in this work, with typically a single tensor element used (i.e., d_{33}) and all others assumed negligible. This will require that the simulations be reproduced with this form, which could be achieved in a straightforward manner since the inversion of the constitutive relationship in this case only involves taking a square-root. Second, since the guided optical beam must now be evanescently coupled to a nonlinear polymer cladding, this will reduce both the effective refractive index of the waveguide and the effective $\chi^{(2)}$ strength, both of which would need to be considered by calculating effective values for the 2D simulations. This reduction of the effective $\chi^{(2)}$ strength can be mitigated by considering that the waveguide-resonator separation distance can be adjusted to achieve critical coupling at the now smaller $\alpha_{2,NL}$, and also that polymers with larger nonlinear coefficients are continually being developed, with values almost three times that of GaAs reported already [129]. Note that if silicon is used as the guiding material, a excitation source near

2 μm or longer wavelengths would again be required to ensure that the SHG signal is not lost to material absorption; as an alternative, silicon nitride could be used instead, which would allow for an excitation at optical communications wavelengths (around 1550 nm) with a SHG output in the near-IR or visible wavelengths.

Despite the SNR benefits provided by the lock-in amplifier, the phase-sensitive measurement test bench still suffers from large insertion losses at the input and output of the test sample. This is largely due to the fact that the tunable laser output is fiber coupled and is collimated into a free-space beam. In addition, the microscope lenses used to couple the light into and out of the sample are not well-matched to the numerical aperture of the on-chip waveguides. Thus, the insertion loss may be improved significantly by using tapered optical fibers, such as those provided commercially by Corning, Inc., to excite the input waveguides and collect the light at the output. Measurement of the high-efficiency SHG device described in Chapter 5 could be accomplished using the test bench with the addition of an optical spectrum analyzer (OSA) at the output in place of the detector and lock-in amplifier. An OSA would allow for the broad spectral bandwidth necessary to observe the fundamental and SHG beams simultaneously, and is compatible with a fiber-based system. Alternatively, a set of band-pass or high- and low-pass filters at the output of the device could be used to allow for discrimination of the fundamental and generated second-harmonic signals using the original free-space configuration.

REFERENCES

[1] R. W. Boyd, *Nonlinear Optics*, San Diego, CA: Academic Press, Inc., 1992.

[2] Y. S. Kivshar and G. Agrawal, *Optical Solitons: From Fibers to Photonic Crystals*, Boston, MA: Academic Press, Inc., 2003.

[3] C. Flytzanis and J. L. Oudar, *Nonlinear Optics: Materials and Devices*, Berlin: Springer Verlag, 1986.

[4] D. L. Mills, *Nonlinear Optics, 2nd Ed.*, Berlin: Springer Verlag, 1998.

[5] D. Mihalache, F. Lederer, D. M. Baboiu, "Two-parameter family of exact solutions of the nonlinear Schrodinger equation describing optical-soliton propagation," *Physical Review A*, vol. 47, no. 4, pp. 3285-3290, 1993.

[6] E. L. Dawes and J. H. Marburger, "Computer studies in self-focusing," *Physical Review*, vol. 179, no. 3, pp. 862-868, 1969.

[7] R.G. Beausoleil, W. J. Munro, T. P. Spiller, "Applications of coherent population transfer to quantum information processing," *Journal of Modern Optics*, vol. 51, no. 11, pp. 1559-1601, 2004.

[8] G. Fibich, B. Ilan, and S. Tsynkov, "Backscattering and nonparaxiality arrest collapse of damped nonlinear waves," *SIAM Journal on Applied Mathematics*, vol. 63, pp. 1718–1736, 2003.

[9] P. I. Borel, L. H. Frandsen, M. Thorhauge, A. Harpoth, Y. X. Zhuang, and M. Kristensen, "Efficient propagation of TM polarized light in photonic crystal components exhibiting band gaps for TE polarized light," *Optics Express*, vol. 11, no. 15, pp. 1757-1762, 2003.

[10] J. Arentoft, T. Sondergaard, M. Kristensen, A. Boltasseva, M. Thorhauge, and L. Frandsen, "Low-loss silicon-on-insulator photonic crystal waveguides," *Electronics Letters*, vol. 38, no. 6, pp. 274-275, 2002.

[11] A. Jafarpour, E. Chow, C. M. Reinke, J. Huang, A. Adibi, A. Grot, L. W. Mirkarimi, G. Girolami, R. K. Lee, and Y. Xu, "Large-bandwidth ultra-low-loss guiding in bi-periodic photonic crystal waveguides," *Applied Physics B.*, vol. B79, no. 4, pp. 409-414, 2004.

[12] Y. Sugimoto, Y. Tanaka, N. Ikeda, Y. Nakamura, K. Asakawa, and K. Inoue, "Low propagation loss of 0.76 dB/mm in GaAs-based single-line-defect two-dimensional photonic crystal slab waveguides up to 1 cm in length," *Optics Express*, vol. 12, no. 6, pp. 1090-1096, 2004.

[13] M. V. Kotlyar, T. Karle, M. D. Settle, L. O'Faolain, and T. F. Krauss, "Low-loss photonic crystal defect waveguides in InP," *Applied Physics Letters*, vol. 84, no. 18, pp. 3588-3590, 2004.

[14] M. Augustin, H.-J. Fuchs, D. Schelle, E.-B. Kley, S. Nolte, A. Tunnermann, R. Iliew, C. Etrich, U. Peschel, and F. Lederer, "High transmission and single-mode operation in low-index-contrast photonic crystal waveguide devices," *Appl. Phys. Lett.*, vol. 84, no. 5, pp. 663-665, 2004.

[15] T. Baba, A. Motegi, T. Iwai, N. Fukaya, Y. Watanabe, and A. Sakai, "Light propagation characteristics of straight single-line-defect waveguides in photonic crystal slabs fabricated into a silicon-on-insulator substrate," *IEEE J. Quantum Electron.*, vol. 38, no. 7, pp. 743-752, 2002.

[16] Y. Suematsu and K. Furuya, "Propagation mode and scattering loss of a two-dimensional dielectric waveguide with gradual distribution of refractive index," *IEEE Transactions on Microwave Theory and Techniques*, vol. MTT-20, pp. 524–531, 1972.

[17] D. Gerace and L. C. Andreani, "Low-loss guided modes in photonic crystal waveguides," *Optics Express*, vol. 13, no. 13, pp. 4939-4951, 2005.

[18] R. Ferrini, D. Leuenberger, R. Houdre, H. Benisty, M Kamp, and A. Forchel, "Disorder-induced losses in planar photonic crystals," *Optics Letters*, vol. 31, no. 10, pp. 1426-1428, 2006.

[19] E. Yablonovitch, "Inhibited spontaneous emission in solid-state physics and electronics," *Physical Review Letters*, vol. 58, no. 20, pp. 2059–2062, 1987.

[20] S. John, “Strong localization of photons in certain disordered dielectric superlattices,” *Physical Review Letters*, vol. 58, no. 23, pp. 2486–2489, 1987.

[21] J. D. Joannopoulos, R. D. Meade, and J. N. Winn, *Photonic Crystals: Molding the Flow of Light*, Princeton, NJ: Princeton Univ. Press, 1995.

[22] M. Soljačić, S. G. Johnson, S. Fan, M. Ibanescu, E. Ippen, and J. D. Joannopoulos, “Photonic-crystal slow-light enhancement of nonlinear phase sensitivity,” *Journal of the Optical Society of America B*, vol. 19, no. 9, pp. 2052-2059, 2002.

[23] J. E. Heebner, N. N. Lepeshkin, A. Schweinsberg, G. W. Wicks, R. W. Boyd, R. Grover, and P.-T. Ho, “Enhanced linear and nonlinear optical phase response of AlGaAs microring resonators,” vol. 29, no. 7, pp. 769-771, 2004.

[24] B. M. Isfahani, T. A. Tameh, N. Granpayeh, and A. R. M. Javan, “All-optical NOR gate based on nonlinear photonic crystal microring resonators,” *Journal of the Optical Society of America B*, vol. 26, no. 5, pp. 1097-1102, 2009.

[25] A. Yariv, “Critical coupling and its control in optical waveguide-ring resonator systems,” *IEEE Photonics Technology Letters*, vol. 14, no. 4, pp. 483-485, 2002.

[26] M. K. Chin and S. T. Ho, “Design and modeling of waveguide-coupled single-mode microring resonators,” *Journal of Lightwave Technology*, vol. 16, no. 8, pp. 1433–1446, 1998.

[27] V. Berger, "Second-harmonic generation in monolithic cavities," *Journal of the Optical Society of America B*, vol. 14, no. 6, pp. 1351-1360, 1997.

[28] S. Nakagawa, N. Yamada, N. Mikoshiba, and D. E. Mars, “Second-harmonic generation from GaAs/AlAs vertical cavity,” *Applied Physics Letters*, vol. 66, no. 17, pp. 2159-2161, 1995.

[29] C. Simonneau, J. P. Debray, J. C. Harmand, P. Vidaković, D. J. Lovering, and J. A. Levenson, "Second-harmonic generation in a doubly resonant semiconductor microcavity," *Optics Letters*, vol. 22, no. 23, pp. 1775-1777, 1997.

[30] Y. Dumeige, and P. Feron, “Whispering-gallery-mode analysis of phase-matched doubly resonant second-harmonic generation,” *Physical Review A*, vol. 74, no. 6, pp. 63804-1-7, 2006.

[31] A. Rodriguez, M. Soljacic, J. D. Joannopoulos, and S. G. Johnson, "$\chi^{(2)}$ and $\chi^{(3)}$ harmonic generation at a critical power in inhomogeneous doubly resonant cavities," *Optics Express*, vol. 15, no. 12, pp. 7303-7318, 2007.

[32] G. Klemens and Y. Fainman, "Optimization-based calculation of optical nonlinear processes in a micro-resonator," *Optics Express*, vol. 14, no. 21, pp. 9864-9872, 2006.

[33] S. J. McNab, N. Moll, and Y. A. Vlasov, "Ultra-low loss photonic integrated circuit with membrane-type photonic crystal waveguides," Optics Express, vol. 11, pp. 2927-39, 2003.

[34] T. Asano, K. Kiyota, D. Kumamoto, B. Song, and S. Noda, "Time-domain measurement of picosecond light-pulse propagation in a two-dimensional photonic crystal-slab waveguide," *Applied Physics Letters*, vol. 84, no. 23, pp. 4690-4692, 2004.

[35] G. Fibich, B. Ilan, and S. Tsynkov, "Backscattering and nonparaxiality arrest collapse of damped nonlinear waves," *SIAM Journal on Applied Mathematics*, vol. 63, pp. 1718–1736, 2003.

[36] K. S. Yee, "Numerical solution of initial boundary value problems involving Maxwell's equations in isotropic media," *IEEE Transactions on Antennas and Propagation*, vol. 14, no. 3, pp. 302-307, 1966.

[37] H. -H. Lee, K. -M. Chae, S. -Y. Yim, and S. -H. Park, "Finite-difference time-domain analysis of self-focusing in a nonlinear Kerr film," *Optics Express*, vol. 12, no. 12, pp. 2603-2609, 2004.

[38] M. Bahl, N. -C. Panoiu, and R. M. Osgood, Jr., "Nonlinear optical effects in a two-dimensional photonic crystal containing one-dimensional Kerr defects," *Physical Review B*, vol. 67, no. 5, pp. 56604-1-9, 2003.

[39] M. A. Alsunaidi, H. M. Masoudi, and J. M. Arnold, "A time-domain algorithm for the analysis of second-harmonic generation in nonlinear optical structures," *IEEE Photonics Technology Letters*, vol. 12, no. 4, pp. 396-397, 2000.

[40] P. Tran, "Optical switching with a nonlinear photonic crystal: a numerical study," *Optics Letters*, vol. 21, no. 15, pp. 1138-1140, 1996.

[41] P. Tran, “Optical limiting and switching of short pulses by use of a nonlinear photonic bandgap structure with a defect,” *Journal of the Optical Society of America B*, vol. 14, no. 10, pp. 2589-2595, 1997.

[42] C. M. Reinke, A. A. Jafarpour, B. Momeni, M. Soltani, S. Khorasani, A. Adibi, Y. Xu, and R. K. Lee, “Nonlinear finite-difference time-domain method for the simulation of anisotropic, $\chi^{(2)}$, and $\chi^{(3)}$ optical effects,” *Journal of Lightwave Technology*, vol. 24, no. 1, 2006.

[43] C. C. Shang and H. Hsu, “The spatial symmetric forms of third-order nonlinear susceptibility,” *IEEE Journal of Quantum Electronics*, vol. QE-23, no. 2, pp. 177-179, 1987.

[44] S. Visnovsky, R. Lopusnik, M. Bauer, J. Bok, J. Fassbender, and B. Hillebrands, "Magnetooptic ellipsometry in multilayers at arbitrary magnetization," *Optics Express*, vol. 9, no. 3, pp. 121-135, 2001.

[45] R. M. Joseph and A. Taflove, “FDTD Maxwell’s equations models for nonlinear electrodynamics and optics,” *IEEE Transactions on Antennas and Propagation*, vol. 45, no. 3, pp. 364-374, 1997.

[46] A. Taflove and S. C. Hagness, *Computation Electrodynamics: The Finite-Difference Time-Domain Method*, Norwood, MA: Artech House, Inc., 2000.

[47] A. C. Cangellaris, “Numerical stability and numerical dispersion of a compact 2-D/FDTD method used for the dispersion analysis of waveguides,” *IEEE Microwave and Guided Wave Letters*, vol. 3, no. 1, pp. 3-5, 1993.

[48] R. F. Remis, “On the stability of the finite-difference time-domain method,” *Journal of Computational Physics*, vol. 163, no. 1, pp. 249-261, 2000.

[49] Y. Amnon and P. Yeh, *Optical waves in crystals: propagation and control of laser radiation*, New York City, NY: Wiley, 1984.

[50] V. Van and S. K. Chaudhuri, “A hybrid implicit–explicit FDTD scheme for nonlinear optical waveguide modeling,” *IEEE Transactions on Microwave Theory and Techniques*, vol. 47, no. 5, pp. 540-545, 1999.

[51] D. E. Merewether, R. Fisher, and F.W. Smith, "On implementing a numeric Huygen's source scheme in a finite difference program to illuminate scattering bodies", *IEEE Transactions on Nuclear Science*, vol. 27, no. 6, pp. 1829-1833, 1980.

[52] T. Baba and T. Iwai, "Enhancement of third order nonlinearity calculated for two-dimensional photonic crystal," *Japanese Journal of Applied Physics*, vol. 42, no. 4A, pp. 1603-1608, 2003.

[53] D. Marcuse, *Theory of Dielectric Optical Waveguides*, Boston: Academic Press, 1991.

[54] A. L. Shimpi, "Intel's Pentium M on the desktop - a viable alternative?", www.anandtech.com/printarticle.aspx?i=2342 (Accessed March 11, 2009).

[55] S. Hughes, L. Ramunno, J. F. Young, and J. E. Sipe, "Extrinsic optical scattering loss in photonic crystal waveguides: role of fabrication disorder and photon group velocity," *Physical Review Letters*, vol. 93, no. 4, pp. 033903/1-4, 2005.

[56] J. Korringa, "On the calculation of the energy of a block wave in a metal," *Physica*, vol. 13, pp. 392-400, 1947.

[57] W. Kohn and N. Rostoker, "Solution of the Schrödinger equation in periodic lattices with an application to metallic lithium," *Physical Review*, vol. 94, no. 5, pp. 1111-1120, 1954.

[58] J. S. Faulkner, H. L. Davis, and H. W. Joy, "Calculation of constant-energy surfaces for copper by the Korringa-Kohn-Rostoker method," *Physical Review*, vol. 161, no. 3, pp. 656-664, 1967.

[59] D. W. Jepson and P. M. Marcus, *Computation Methods in Band Theory*, New York: Plenum Press, 1971.

[60] D. W. Jepson, P. M. Marcus, and F. Jona, "Low-energy-electron-diffraction spectra from [001] surface of face-centered cubic metals: Theory and experiment," *Physical Review B*, vol. 5, no. 10, pp. 3933-3952, 1972.

[61] S. Lounis, P. Mavropoulos, P. H. Dederichs, and S. Blügel, "Surface-state scattering by adatoms on noble metals: Ab initio calculations using the Korringa-Kohn-Rostoker Green function method," *Physical Review B*, vol. 73, no. 19, pp. 195421-1-6, 2006.

[62] A. Modinos, N. Stefanou, and V. Yannopapas, "Applications of the layer-KKR method to photonic crystals," *Optics Express*, vol. 8, no. 3, pp. 197-202, 2001.

[63] N. C. Debnath, M. R. Chowdhuri, S. Chatterjee, "Electronic energy bands and optical properties of Cr and Fe by the KKR method," *Journal of Physics F*, vol. 15, no. 8, pp. 1693-1701, 1985.

[64] Y.-J. Lee, S. A. Pruzinsky, P. V. Braun, "Diffraction response of colloidal crystals: effect of numerical aperture," *Optics Letters*, vol. 20, no. 2, pp. 153-155, 2005.

[65] J. M. MacLaren, "Layer Korringa-Kohn-Rostoker electronic structure code for bulk and interface geometries," *Computer Physics Communications*, vol. 60, no. 3, pp. 365-389, 1990.

[66] X. G. Zhang, K. Varga, and S. T. Pantelides, "Generalized bloch theorem for complex periodic potentials – a powerful application to quantum transport calculations," *Physical Review B*, vol. 76, no. 3, pp. 35108/1-9, 2007.

[67] P. M. Morse and H. Feshbach, *Methods of Theoretical Physics*, New York: McGraw-Hill, 1953.

[68] K. M. Ho, C. T. Chan, and C. M. Soukoulis, "Existence of a photonic gap in periodic dielectric structures," *Physical Review Letters*, vol. 65, no. 25, pp. 3152-3155, 1990.

[69] J. Klima, G. Schadler, P. Weinberger, and A. Neckel, "On the electrical structure of TiN_x," *Journal of Physics F*, vol. 15, no. 6, pp. 1307-1320, 1985.

[70] A. Meike, A. Gonis, P. E. Turchi, and K. Rajan, *Properties of complex inorganic solids 2*, New York: Kluwer Academic/Plenum, 2000.

[71] J. S. Faulkner and G. M. Stocks, "Calculating properties with the coherent-potential approximation," *Physical Review B*, vol. 21, no. 8, pp. 3222-3244, 1980.

[72] S. G. Johnson, S. Fan, P. R. Villeneuve, J. D. Joannopoulos, and L. A. Kolodziejski, "Guided modes in photonic crystal slabs," *Physical Review B*, vol. 60, no. 8, pp. 5751-5758, 1999.

[73] M. Qiu, K. Azizi, A. Karlsson, M. Swillo, and B. Jaskorzynska, " Numerical studies of mode gaps and coupling efficiency for line-defect waveguides in two-dimensional photonic crystals," *Physical Review B*, vol. 64, no. 15, pp. 155113-155117, 2001.

[74] S. Boscolo, C .Conti, M. Midrio, and C. G. Someda, "Numerical analysis of propagation and impedance matching in 2D photonic crystal waveguides with finite length," *Journal of Lightwave Technology*, vol. 20, no. 2, pp. 304-310, 2002.

[75] P. Lalanne, "Electromagnetic analysis of photonic crystal waveguides operating above the light cone," *IEEE Journal of Quantum Electronics*, vol. 38, no. 7, pp. 800-804, 2002.

[76] T. Sondergaard, J. Arentoft, and M. Kristensen, "Theoretical analysis of finite-height semiconductor-on-insulator-based planar photonic crystal waveguides," *Journal of Lightwave Technology*, vol. 20, no. 8, pp. 1619-1626, 2002.

[77] E. Lidorikis, M. L. Povinelli, S. G. Johnson, and J. D. Joannopoulos, "Polarization-independent linear waveguides in 3D photonic crystals," *Physical Review Letters*, vol. 91, no. 2, pp. 23902-23905, 2003.

[78] K. M. Ho, C. T. Chan, and C. M. Soukoulis, "Existence of a photonic gap in periodic dielectric structures," *Physical Review Letters*, vol. 65, no, 25, pp. 3152-3155, 1990.

[79] W. M. Robertson, G. Arjavalingam, R. D. Meade, K. D. Brommer, A. M. Rappe, and J. D. Joannopoulos, "Measurement of photonic band structure in a two-dimensional periodic dielectric array," *Physical Review Letters*, vol. 68, no. 13, pp. 2023-2026, 1992.

[80] K. W. K. Shung and Y. C. Tsai, "Surface effects and band measurements in photonic crystals," *Physical Review B*, vol. 48, no. 15, pp. 1265-11269, 1993.

[81] M. Loncar, M. Hochberg, A. Scherer, and Q. Yueming, "High quality factors and room-temperature lasing in a modified single-defect photonic crystal cavity," *Optics Letters*, vol. 29, no. 7, pp. 721-723, 2004.

[82] A. Mekis, J. C. Chen, I. Kurland, S. Fan, P. R. Villeneuve, and J. D. Joannopoulos, "High transmission through sharp bends in photonic crystal waveguides," *Physical Review Letters*, vol. 77, no. 18, pp. 3787-3790, 1996.

[83] H. Takano, Y. Akahane, T. Asano, and S. Noda, "In-plane-type channel drop filter in a two-dimensional photonic crystal slab," *Applied Physics Letters*, vol. 84, no. 13, pp. 2226-2228, 2004.

[84] A. Chutinan, S. John, and O. Toader, "Diffractionless flow of light in all-optical microchips," *Physical Review Letters*, vol. 90, no. 12, pp. 123901/1-4, 2003.

[85] N. Wu, M. Soltani, B. Momeni, M. Javanmard, A. Adibi, Y. Xu, and R. K. Lee, "General methods for designing single-mode planar photonic crystal waveguides in hexagonal lattice structures," *Optics Express*, vol. 11, no. 12, pp. 1371-1377, 2003.

[86] S. F. Mingaleev and Y. S. Kivshar, "Nonlinear transmission and light localization in photonic crystal waveguides," *Journal of the Optical Society of America B*, vol. 19, no. 9, pp. 2241-2249, 2002.

[87] E. Yablonovitch, "Photonic crystals," *Journal of Modern Optics*, vol. 41, no. 2, pp. 173-194, 1994.

[88] S. John and M. Florescu, "Photonic bandgap materials: towards an all-optical micro-transistor," *Journal of Optics A*, vol. 3, no. 6, pp. S103-S120, 2001.

[89] S. Fan and J. D. Joannopoulos, "Photonic crystals: towards large-scale integration of optical and optoelectronic circuits," *Optics and Photonics News*, vol. 11, no. 10, pp. 28-33, 2000.

[90] J. Martorell, "Parametric nonlinear interaction in centrosymmetric three-dimensional photonic crystals," *Journal of the Optical Society of America B*, vol. 19, no. 9, pp. 2075-2082, 2002.

[91] Y. Xu, R. K. Lee, and A. Yariv, "Propagation and second-harmonic generation of electromagnetic waves in a coupled-resonator optical waveguide," *Journal of the Optical Society of America B*, vol. 17, no. 3, pp. 387-400, 2000.

[92] Y. Dumeige, I. Sagnes, P. Monnier, P. Vidakovic, C. Mériadec, and A. Levenson, "$\chi^{(2)}$ semiconductor photonic crystals," *Journal of the Optical Society of America B*, vol. 19, no. 9, pp. 2094-2101, 2002.

[93] M. D. Rahn, A. M. Fox, M. S. Skolnick, and T. F. Krauss, "Propagation of ultrashort nonlinear pulses through two-dimensional AlGaAs high-contrast photonic crystal waveguides," *Journal of the Optical Society of America B*, vol. 19, no. 4, pp. 716-721, 2002.

[94] M. Soljačić, M. Ibanescu, S. G. Johnson, J. D. Joannopoulos, and Y. Fink, "Optical bistability in axially modulated OmniGuide fibers," *Optics Letters*, vol. 28, no. 7, pp. 516-518, 2003.

[95] M. Soljačić, C. Luo, J. D. Joannopoulos, and S. Fan, "Nonlinear photonic crystal microdevices for optical integration," *Optics Letters*, vol. 28, no. 8, pp. 637-639, 2003.

[96] A. Babin, A. Figotin, "Nonlinear photonic crystals: I. Quadratic nonlinearity," *Waves in Random Media*, vol. 11, no. 2, pp. R31-102, 2001.

[97] A. Babin, A. Figotin, "Nonlinear photonic crystals. II. Interaction classification for quadratic nonlinearities," *Waves in Random Media*, vol. 12, no. 4, pp. R25-52, 2002.

[98] A. Babin, A. Figotin, "Nonlinear photonic crystals. III. Cubic nonlinearity," *Waves in Random Media*, vol. 13, no. 4, pp. R41-69, 2003.

[99] M. Qiu and B. Jaskorzynska, " Design of a channel drop filter in a two-dimensional triangular photonic crystal," *Applied Physics Letters*, vol. 83, no. 6, pp. 1074-1076, 2003.

[100] T.F. Krauss, "Planar photonic crystal waveguide devices for integrated optics," *Physica Status Solidi A*, vol. 197, no. 3, pp. 688-702, 2003.

[101] D. A. Kleinman, "Theory of second harmonic generation of light," *Physical Review*, vol.128, no. 4, pp. 1761-1775, 1962.

[102] L. A. Glasser, "CW modelocking of a GaInAsP diode laser," *Electronics Letters*, vol. 14, no. 23, pp. 725-726, 1978.

[103] S.-W. Chu, S.-P. Tai, T.-M. Liu, C.-K. Sun, and C.-H. Lin, "Selective imaging in second-harmonic-generation microscopy with anisotropic radiation," *Journal of Biomedical Optics*, vol. 14, no. 1, pp. 010504, 2009.

[104] Y. L. Chen, G. Liu, B. B. Zhou, Z. Y. Wei, and Y. Q. Zheng, "Wavelength conversion in a Ti:PPSMgLN channel waveguide," *Optics Communications*, vol. 282, no. 13, pp. 2524-2526, 2009.

[105] T. Mizushima, H. Furuya, S. Shikii, K. Kusukame, K. Mizuuchi, and K. Yamamoto, "Second harmonic generation with high conversion efficiency and wide temperature tolerance by multi-pass scheme," *Applied Physics Express*, vol. 1, no. 3, pp. 032003-1-3, 2008.

[106] I. D. Henning, "Materials for optoelectronic and photonic integrated circuits," *Progress in Crystal Growth and Characterization*, vol. 19, no. 1/2, pp. 1-20, 1989.

[107] W. Bogaerts, D. Taillaert, B. Luyssaert, P. Dumon, J. Van Campenhout, P. Bienstman, D. Van Thourhout, R. Baets, V. Wiaux, and S. Beckx, "Basic structures for photonic integrated circuits in silicon-on-insulator," *Optics Express*, vol. 12, no. 8, pp. 1583-1591, 2004.

[108] K. Sakai, Y. Koyata, S. Itakura, and Y. Hirano, "High-power, highly efficient second-harmonic generation in a periodically poled MgO:$LiNbO_3$ planar waveguide," *Journal of Lightwave Technology*, vol. 27, no. 5, pp. 590–596, 2009.

[109] J. A. Giordmaine, "Mixing of light beams in crystals," *Physical Review Letters*, vol. 8, no. 1, pp. 19-20, 1962.

[110] P. D. Maker, R. W. Terhune, M. Nisenoff, C. M. Savage, "Effects of dispersion and focusing on the production of optical harmonics," *Physical Review Letters*, vol. 8, no. 1, pp. 21-22, 1962.

[111] J. Yamawaku, E. Yamazaki, A. Takada, and T. Morioka, "Field trial of virtual-grouped-wavelength-path switching with QPM-LN waveband converter and PLC matrix switch in JGN II test bed," *Electronics Letters*, vol. 41, no.2, pp. 88-89, 2005.

[112] A. Yariv, "Universal relations for coupling of optical power between microresonators and dielectric waveguides," *Electronics Letters*, vol. 36, no. 4, pp. 321-322, 2000.

[113] P. N, Butcher and D. Cotter, *The elements of nonlinear optics*, Cambridge, MA: Cambridge University Press, 1990.

[114] Y. Xu , Y. Li, R. K. Lee, and A. Yariv, "Scattering-theory analysis of waveguide-resonator coupling," *Physical Review E*, vol. 62, no. 5, pp. 7389-7404, 2000.

[115] J. P. Berenger, "A perfectly matched layer for the absorption of electromagnetic waves," *Journal of Computational Physics*, vol. 114, no. 2, pp. 185-200, 1994.

[116] A. Szilagyi, A. Horduik, H. Schlossberg, "A quasi-phase-matching technique for efficient optical mixing and frequency doubling," *Journal of Applied Physics*, vol. 47, no. 5, pp. 2025-2032, 1976.

[117] T. Asano, K. Kiyota, D. Kumamoto, B. Song, and S. Noda, "Time-domain measurement of picosecond light-pulse propagation in a two-dimensional photonic crystal-slab waveguide," *Applied Physics Letters*, vol. 84, pp. 4690-4692, 2004.

[118] J. Huang, C. M. Reinke, A. Jafarpour, B. Momeni, M. Soltani and A. Adibi, "Observation of large parity-change-induced dispersion in triangular-lattice photonic crystal waveguides using phase sensitive techniques," *Applied Physics Letters*, vol. 88, pp. 071111-1-3, 2006.

[119] S. Wang, H. Erlig, H. R. Fetterman, E. Yablonovitch, V. Grubsky, D. S. Starodubov, and J. Feinberg, "Group velocity dispersion cancellation and additive group delays by cascaded fiber Bragg gratings in transmission," *IEEE Microwave and Guided Wave Letters*, vol. 8, no. 20, pp. 327-329, 1998.

[120] T. Asano, K. Kiyota, D. Kumamoto, B. Song, and S. Noda, "Time-domain measurement of picosecond light-pulse propagation in a two-dimensional photonic crystal-slab waveguide," *Applied Physics Letters*, vol. 84, no. 23, pp. 4690-4692, 2004.

[121] H. Gersen, T. J. Karle, R. J. P. Engelen, W. Bogaerts, J. P. Korterik, N. F. van Hulst, T. F. Krauss, and L. Kuipers, "Real-space observation of ultraslow light in photonic crystal waveguides," *Physical Review Letters*, vol. 94, no. 7, pp. 073903/1-4, 2005.

[122] B. Cluzel, D. Gérard, E. Picard, T. Charvolin, V. Calvo, E. Hadji, and F. de Fornel, "Experimental demonstration of Bloch mode parity change in photonic crystal waveguide," *Applied Physics Letters*, vol. 85, no. 14, pp. 2682-2684, 2004.

[123] S. Hughes, L. Ramunno, J. F. Young, and J. E. Sipe, "Extrinsic optical scattering loss in photonic Crystal waveguides: role of fabrication disorder and photon Group velocity," *Physical Review Letters*, vol. 94, no. 3, pp. 033903/1-4, 2005.

[124] J. Marangos, "Slow light in cool atoms," *Nature*, vol. 397, no. 6720, pp. 559, 1999.

[125] S. Tay, J. Thomas, B. Momeni, M. Askari, A. Adibi, P. J. Hotchkiss, S. C. Jones, S. R. Marder, R. A. Norwood, and N. Peyghambarian, "Planar photonic crystals infiltrated with nanoparticle/polymer composites," *Applied Physics Letters*, vol. 91, no, 22, pp. 221109-1-3, 2007.

[126] T. Skauli, K. L. Vodopyanov, T. J. Pinguet, A. Schober, O. Levi, L. A. Eyres, M. M. Fejer, J. S. Harris, B. Gerard, L. Becouarn, and E. Lallier, "Measurement of the nonlinear coefficient of orientation-patterned GaAs and demonstration of highly efficient second-harmonic generation," *Optics Letters*, vol. 27, no. 8, pp. 628-630, 2002.

[127] Z. Li, P. Hu, G. Yu, W. Zhang, Z. Jiang, Y. Liu, C. Ye, J. Qin, and Z. Li, "'H'-shape second order NLO polymers: synthesis and characterization," *Physical Chemistry Chemical Physics*, vol. 11, no. 8, pp. 1220-1226, 2009.

[128] R. A. Norwood, G. Khanarian, "Quasi-phase-matched frequency doubling over 5 mm in periodically poled polymer waveguide," *Electronics Letters*, vol. 26, no. 25, pp. 2105-2107, 1990.

[129] M. Hochberg, T. Baehr-Jones, G. Wang, J. Huang, P. Sullivan, L. Dalton, and A. Scherer, "Towards a millivolt optical modulator with nano-slot waveguides," *Optics Express*, vol. 15, no. 13, pp. 8401-8410, 2007.

VITA

CHARLES M. REINKE

Charles M. Reinke was born in Detroit, MI. He received his B.S. in Physics from Jackson State University in 2000 and his B.S. in Electrical Engineering from the Georgia Institute of Technology in 2001. He continued his graduate studies in the School of Electrical and Computer Engineering at Georgia Tech, earning a M.S.E.E. in 2007 and a Ph.D. in 2009, also in Electrical Engineering. He was a finalist for both the Bell Labs Graduate Research Fellowship and National Science Foundation Graduate Research Fellowship, a participant in the Lucent Cooperative Research Fellowship Program, and a recipient of the Georgia Tech President's Fellowship. In 2003, he was awarded the Best Paper Award from the International Association for Mathematics and Computers in Simulation (IMACS), Athens, GA. He has been a member of IEEE since 1999 and the Optical Society of America since 2001. After graduating, he accepted a postdoctoral appointee position at Sandia National Laboratories in their Photonic Microsystems Technologies group. Charles' technical interests include nanophotonics, nonlinear optics, and computational electrodynamics.